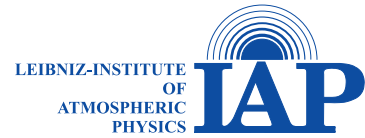


Universität  
Rostock



Traditio et Innovatio



# Development of a small-scale LITOS payload for turbulence measurements in the stratosphere

This thesis is submitted in  
partial fulfilment of the  
requirements for the degree of  
M. Sc. in physics

by

Jens Söder

7200878

Advisors: Prof. Dr. Franz-Josef Lübken (Rostock University)  
Dr. Michael Gerding (IAP Kühlungsborn)

Leibniz-Institute of Atmospheric Physics e.V.  
at Rostock University

5<sup>th</sup> September 2014



## **Abstract**

Since the first tests of CTA measurements at IAP nearly a decade ago, with LITOS a new balloon-borne instrument for in situ measurements of stratospheric energy dissipation rates has been established. This work is focused on the development of a small-scale LITOS payload weighing below 5 kg. The new device allows for measurements of energy dissipation rates by evaluation of velocity fluctuations from every radiosonde station. To achieve this, a new payload design is created which reduces pendulum motions of the gondola. Additionally, the LITOS measurement system is further developed by introducing the use of two independent constant temperature anemometers to the data acquisition scheme. Furthermore, the development of a new flightpath forecasting system is part of the project. Two successful measurements over Kühlungsborn (northern Germany) have been carried out using the new LITOS system: One of them revealing a constant energy dissipation rate in the troposphere and an increase in the stratosphere, the other one showing an increase from above the boundary layer to about 15 km and a sharp drop beyond. These findings are related to geophysical background conditions, to other measurements of energy dissipation rates and to the Richardson number.

## **Zusammenfassung**

Seit den ersten Tests von CTA-Messungen am IAP vor fast einem Jahrzehnt wurde mit LITOS ein neues ballongetragenes Instrument für in-situ-Messungen der Energiedissipationsrate in der Stratosphäre etabliert. Diese Arbeit legt den Schwerpunkt auf die Entwicklung einer kleinen LITOS-Nutzlast mit einem Gewicht von weniger als 5 kg. Sie erlaubt von jeder Radisondenstation aus die Messung der Energiedissipationsrate durch Auswertung von Geschwindigkeitsfluktuationen. Um dies zu erreichen, wird eine neue Nutzlastform gestaltet, die die Pendelbewegungen der Gondel reduziert. Zusätzlich ist das LITOS-Messsystem durch die Benutzung zweier unabhängiger Konstant-Temperatur-Anemometer weiterentwickelt und ein neues Flugbahn-Vorhersage-System programmiert worden. Zwei erfolgreiche Messungen unter Benutzung des neuen LITOS-Systems wurden über Kühlungsborn (Norddeutschland) durchgeführt: Eine von ihnen zeigt eine konstante Energiedissipationsrate in der Troposphäre und eine Zunahme in der Stratosphäre, die andere hingegen eine Zunahme von oberhalb der Grenzschicht bis etwa 15 km und einen starken Abfall darüber. Diese Befunde werden im Zusammenhang mit geophysikalischen Hintergrundbedingungen, anderen Messungen der Energiedissipationsrate und der Richardson-Zahl diskutiert.



# Contents

<b>1. Introduction</b>	<b>1</b>
1.1. Historical survey of stratospheric measurements	1
1.2. Why measuring turbulence in the stratosphere?	3
<b>2. Turbulence theory and measurement strategies</b>	<b>5</b>
2.1. The statistical approach to turbulence	5
2.1.1. Characterisation of turbulent flows	5
2.1.2. Important atmospheric parameters	6
2.1.3. The concept of the structure function	7
2.1.4. The energy spectrum of turbulence	8
2.1.5. How to determine the energy dissipation rate from the inner scale	10
2.2. How to measure turbulence in the stratosphere?	11
2.2.1. Balloon borne ionic anemometers	12
2.2.2. Thorpe analysis of radiosonde data	12
2.2.3. Satellite based scintillation measurements	13
2.3. The measurement principle of LITOS	14
2.3.1. CTA measurement principle	14
2.3.2. Data processing	16
<b>3. Payload development</b>	<b>23</b>
3.1. Pendulum calculation	23
3.2. Payload design	25
3.2.1. Payload shape	25
3.2.2. Payload mounting	28
3.2.3. Interior design	30
3.2.4. Quality of turbulence measurements	34
3.3. Flight path prediction	40
3.3.1. Balloon filling	41
3.3.2. Balloon ascent	42
3.3.3. Balloon descent	45
3.3.4. Wind divergence	46
3.3.5. Evaluation	47
<b>4. Geophysical results</b>	<b>51</b>
4.1. Energy dissipation rates	51
4.2. Influence of the data evaluation scheme	55
4.3. Comparison with other measurements	57
4.4. Meteorological background conditions	58

## *Contents*

- 4.5. Occurrence of turbulence compared to the Richardson number 62
- 4.6. The influence of Kelvin-Helmholtz instabilities and gravity wave breaking on turbulence 64
- 5. Conclusion and prospects 67**
- A. Appendix 69**
  - A.1. Noise level detection 69
  - A.2. Dereeler cords 70

# 1. Introduction

## 1.1. Historical survey of stratospheric measurements

Early investigations of the atmosphere's vertical structure were conducted in the 18<sup>th</sup> century by mountaineers equipped with barometers and thermometers. Soon, scientists became aware that the conditions around a mountain are influenced by the mountain itself. With the invention of the hot air balloon in 1783 measurements in the free atmosphere became possible. Still, there was hardly any knowledge of the atmosphere's general temperature structure, as it is depicted in Figure 1.1. In the 1860s and 1870s, several aeronauts reached altitudes of up to 10 km, but some of them paid for these attempts with their life [Hoinka et al., 1997]. This problem was not solved until the end of the century, when the unmanned sounding balloon was invented. On 14<sup>th</sup> of November 1892 Gustave Hermite launched a hydrogen filled paper balloon with a registering thermometer and a mercury barometer on-board. He recorded a minimum temperature of  $-10^{\circ}\text{C}$  and a maximum height of 7 600 m [Hermite, 1892]. A year later he reached altitudes of up to 14 700 m. As Hoinka et al. [1997] suggest, these measurements are likely to be influenced by effects of solar radiation on the thermometer. According to him, a few years later, the scientists Léon Teisserenc de Bort and Richard Aßman developed methods to avoid these radiation effects. They both discovered the existence of the tropopause after they had rejected the strong decrease in the temperature lapse rate as a measurement error in the first place. Aßmann [1902] concludes: "[Man wird] nicht umhin können, die Existenz eines erheblich höher temperierten Luftstromes oberhalb der Zone von 10 bis 12<sup>km</sup> als bewiesen

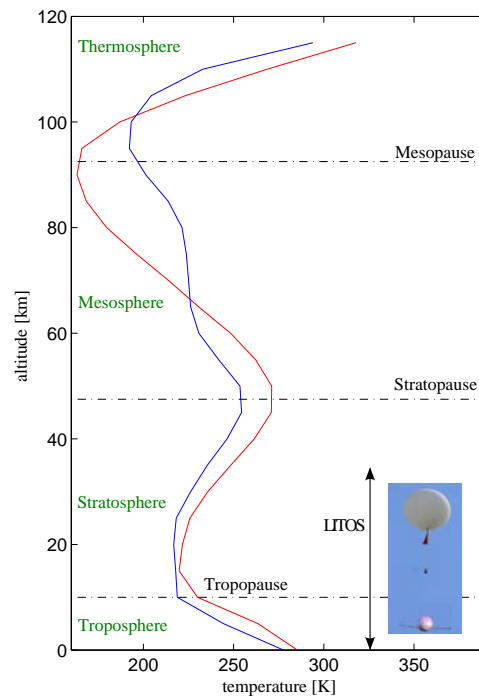


Figure 1.1.: Temperature structure of the Earth's atmosphere for midlatitudes on the northern hemisphere in winter (blue) and summer (red). Temperatures are taken from Fleming et al. [1988]. The black arrow on the right indicates the altitude range of LITOS.

## 1. Introduction

anzusehen.”<sup>1</sup> In cooperation with Continental, Åsman developed a new type of sounding balloon. It was made from rubber and expands during ascent [Hoinka et al., 1997]. Thereby, the ascent rate is kept constant until the stretch of the material reaches its maximum. Then the balloon bursts and the payload slides down with a parachute. This is pretty much the same concept which is still used with LITOS today. Whereas there are satellite based tracking systems available today, scientists at the beginning of the 20<sup>th</sup> century did not even have radio communication, so they were dependent on people finding their instruments and returning them. A contemporary plate offering finder’s reward is shown in Figure 1.2. In order to put the reward of 5 Shillings into perspective, it might be interesting to notice that the agricultural labourer who was likely to find the payload earned a weekly wage of 15 Shillings.

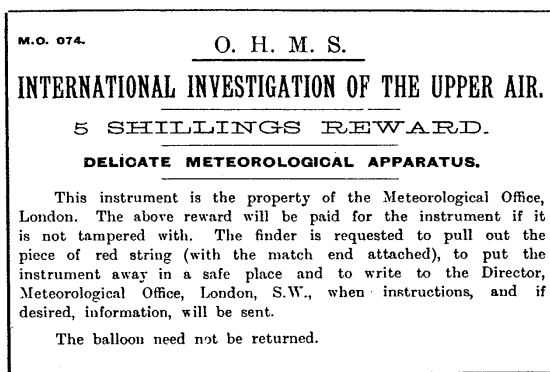


Figure 1.2.: Plate announcing finder’s reward as it was mounted on a balloon payload in 1913 [Hoinka et al., 1997].

Next question is about the reason behind this change in the temperature lapse rate. Åsman made a suggestion which actually foreshadows the so called Brewer-Dobson-Circulation accepted by the scientific community about 50 years later: “Wenn die über den tropischen Meeren unter steter Condensation ihres Wasserdampfes zu grossen Höhen aufgestiegenen und deshalb relativ warmen Luftmassen auf einer nach den Polen zu schräg abwärts geneigten Bahn fließen, so würden sie ihren durch Leitung und Strahlung erfolgten Wärmeverlust durch den dynamis-

chen Vorgang beim Niedersinken wohl ersetzen und noch in höhere Breiten als relativ hochtemperierte Strömung vordringen können.”<sup>2</sup>[Åsman, 1902] This residual circulation is driven by atmospheric waves and was thoroughly examined and explained for the first time by Alan Brewer [1949]. It is responsible for the temperature structure of the stratosphere, which results in its stable stratification. This in turn makes turbulent patches comparatively small in volume [Alisse et al., 2000]. Dobson’s conclusions were driven by aircraft-borne measurements of temperature and water vapour content near the tropopause. In the mid 1950s, Gordon Dobson extended these studies by measurements of tropospheric and stratospheric ozone concentrations [Dobson, 1956]. The circulation which is accountable for these distributions can be seen in Figure 1.3. This circulation is mainly driven by breaking Rossby waves in the stratosphere. The wave breaking deposits angular momentum near the tropopause, which is balanced by the Coriolis torque associated with the latitudinal mass flux of the Brewer-

- 1 There is no other way than taking the existence of a considerably higher tempered air flow above the altitude range of 10 to 12 km as demonstrated.
- 2 Set the case, the air masses are ascending above the tropical sea, losing their water vapour content by condensation and thus relatively warm air is floating along a descending path polewards. Then they would substitute their heat loss due to conduction and radiation and penetrate to even higher latitudes as a relatively high tempered flow.

## 1.2. Why measuring turbulence in the stratosphere?

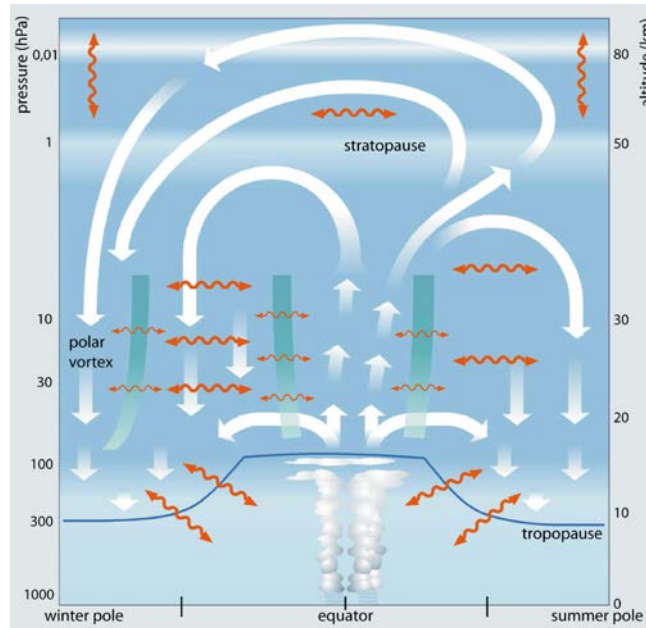


Figure 1.3.: Schematic drawing of the Brewer-Dobson-Circulation by Bönisch et al. [2011]. The circulation is indicated by white arrows, orange arrows depict horizontal mixing.

Dobson circulation [Shepherd, 2007]. To a smaller extent, this circulation is also driven by breaking gravity waves. Together with Kelvin-Helmholtz instabilities they are the main source of stratospheric turbulence. The strength of this turbulence is usually given by the turbulent energy dissipation rate  $\epsilon$ . It provides a measure for the amount of energy per unit time and unit mass that is dissipated into heat. Turbulence in the stratosphere can be measured by satellite soundings [Gavrilov, 2013]. With ground based techniques like RADAR [Lübken, 2014, Nastrom and Eaton, 2001] and LIDAR [Smalikho et al., 2005] one can access the lower stratosphere and the atmospheric boundary layer respectively. Nevertheless, these data sets have low vertical resolutions compared to in situ measurements. High resolution data between 60 and 110 km have been acquired using rockets as carriers [Lübken, 1997]. In the stratosphere, fairly few high resolution turbulence measurements have been done. Early aircraft borne measurements were carried out by Waco [1970]. He evaluated data from an accelerometer flown on an American spy plane in altitudes between 15 and 25 km. These observations were connected to meteorological background data drawn from radiosonde ascents at maximum 160 km or 6 hr away. Early balloon borne measurements of turbulence were carried out by Jean Barat and co-workers [e.g. Barat, 1982]. For a review on his work and other methods of measuring Clear Air Turbulence (CAT) in the stratosphere, please see Section 2.2. The measurement principle of LITOS is demonstrated in Section 2.3.

## 1.2. Why measuring turbulence in the stratosphere?

As visible in Figure 1.1, the stratosphere is characterised by a small negative or even positive temperature gradient. Generally, the stratosphere is stably stratified, hence its name. This is

## 1. Introduction

because the temperature gradient is larger than the adiabatic lapse rate, which in turn leads to positive values of the Brunt-Väisälä frequency  $N^2$ , please see Section 2.1.2 for further details. The positive temperature gradient in the stratosphere is caused by solar heating due to ozone absorption. 90% of the total ozone abundance in the Earth's atmosphere is located in the stratosphere. Absorption of solar radiation by ozone leads to a maximum heating rate of 12 K/day [Brasseur and Solomon, 1986] in an altitude of 50 km. This is compensated for by radiative cooling mainly due to carbon dioxide and water vapour and eventually leads to the stratospheric temperature profile seen in Figure 1.1. As mentioned in the previous section, two major transport processes in the stratosphere are the Brewer-Dobson circulation and horizontal mixing. These mechanisms are important to know, because they drive the atmospheric distribution of trace gases like ozone and carbon dioxide which in turn have large effects on climate and in case of ozone also on humankind due to absorption of genetically harmful ultraviolet radiation. Another important transport process is small scale turbulent mixing. Alisse et al. [2000] reports radar measurements, which find vertical eddy diffusivities so large that the "contribution of turbulence to large-scale dispersive transport in the lower stratosphere is [...] larger than that resulting from the combined effect of mean 'Brewer-Dobson' circulation and quasi-horizontal mixing by large scale eddies." Therefrom it may be concluded that turbulence does indeed play a vital role for the distribution of stratospheric trace gases. Air traffic is yet another field where turbulence must be considered. Flight levels of usual airliners are located in the lower stratosphere. Clear air turbulence leads to several serious incidents each year [Sharman et al., 2012].

Coming back to atmospheric layering, it can be said that the troposphere is well mixed due to its unstable stratification. This is not the case for the stratosphere. Fritts et al. [2003] remarks that "in all stably stratified environments, turbulence often occurs in layers of limited depth, with the turbulence extent determined initially by the scale of shear instability or wave breaking". From observations with LITOS we found that many turbulent patches in the stratosphere are less than 10 m in altitude. Therefore, especially satellite based measurements like those done by Gavrilov [2013] but also balloon borne turbulence measurements like those carried out by Barat [1982] can not resolve the fine structure of energy dissipation rates in the stratosphere. On the other hand, satellite based measurements provide data sets with global coverage, which can not be acquired by in situ measurements. Nevertheless, the problem of altitude resolution was overcome by LITOS as used on several BEXUS campaigns. With the availability of the new small-scale LITOS payload, these high resolution measurements may be carried out on a regular basis now.

## 2. Turbulence theory and measurement strategies

This chapter aims to give an overview of the principles underlying turbulence measurements with LITOS. It is divided into three sections. The first one deals with general remarks on turbulence, with its mathematical description and with the method of deriving turbulent energy dissipation rates as used by LITOS. The second one deals with an overview over methods of measuring energy dissipation rates aside from LITOS. The last one is concerned with the measurement principle of LITOS, including description of the instrument, of data retrieval strategies and presentation of exemplary measurements.

### 2.1. The statistical approach to turbulence

In this section a brief introduction to the statistical description of turbulent flows will be given first. Then the focus is turned on the spectral energy density of turbulent flows in general and the section will conclude with information on the theory underlying the acquisition of energy dissipation rates from velocity fluctuations. Generally, the scope of this section does not include a complete derivation of the formulae. Instead, the important relations will be presented and their elements explained.

#### 2.1.1. Characterisation of turbulent flows

According to an apocryphal story, once Werner Heisenberg was asked what he would like to know from God. He answered: “When I meet God, I am going to ask him two questions: Why relativity? And why turbulence? I really believe he will have an answer for the first.” [Davis and Marshak, 2005]

Alongside the funny overtone of Heisenberg’s remark he is making a point with his words. Not only that science does not really have an answer to the question *Why turbulence?*, also *What is turbulence?* can hardly be explained in a single sentence. Instead, a characterisation of main features of turbulent flows shall be given here. In doing so, the description of Tennekes and Lumley [1972] will be followed.

*Turbulent motions are:*

- *irregular*  
Motions are of random nature and cannot be described by deterministic methods.
- *diffusive*  
Turbulence induces rapid mixing by increased rates of heat, mass and momentum transfer.

## 2. Turbulence theory and measurement strategies

- *characterised by large Reynolds numbers*  
Turbulence occurs at high Reynolds numbers only. In other words: inertial forces need to dominate viscous forces.
- *dissipative*  
Turbulent flows always need an energy source to maintain their motion against the viscous losses.
- *continuous*  
Turbulence occurs on spatial scales where quantum mechanic effects do not play a role.
- *motions*  
The very properties of a turbulent flow are not features of the fluid, but of the fluid motions that occur.

This list may be neither exclusive nor exhaustive, but it provides necessary conditions for turbulence.

### 2.1.2. Important atmospheric parameters

Here, atmospheric parameters which are related to turbulence measurements will be introduced. Namely these are the Reynolds number  $Re$ , the kinematic viscosity  $\nu$ , the Brunt-Väisälä frequency  $N$  and the Richardson number  $Ri$ .

The third item of the list in the previous subsection deals with the so called *Reynolds number*  $Re$ . It is a dimensionless number that gives an estimate whether a flow is turbulent or not:

$$Re = \frac{v_0 l_0}{\nu} = \frac{\text{inertial forces}}{\text{viscous forces}} \quad (2.1.1)$$

where  $v_0$  is the typical velocity of the flow,  $l_0$  its typical length scale and  $\nu$  the kinematic viscosity. As stated in the list above, a flow changes its characteristics from laminar to turbulent if  $Re$  exceeds a certain critical value. This value is dependent on the shape of the body in the flow. According to Hucho [2011] it is usually in the range of  $Re = 10000$ .

The kinematic viscosity  $\nu$  in turn is given with the air density  $\rho$  and the dynamic viscosity  $\mu$  by

$$\nu = \frac{\mu}{\rho} \quad (2.1.2)$$

after NOAA [1976], the dynamic viscosity can be calculated from temperature  $T$  by

$$\mu = \frac{1.458e-6 \cdot T^{3/2}}{(T + 110)} \quad (2.1.3)$$

## 2.1. The statistical approach to turbulence

In case of LITOS,  $T$  is measured by a radiosonde.

A parameter connected to the stability of a fluid's stratification is the Brunt-Väisälä frequency  $N$ . For a general fluid, it is given by

$$N = \sqrt{\frac{g}{\rho_0} \frac{\partial \rho(z)}{\partial z}} \quad (2.1.4)$$

with  $g$  being the gravitational constant,  $\rho_0$  the density of the air parcel and  $\frac{\partial \rho(z)}{\partial z}$  the density gradient of the background fluid. For atmospheric conditions it can be written

$$N = \sqrt{\frac{g}{\rho_0} \left( \frac{\partial T}{\partial z} - \Gamma \right)} \quad (2.1.5)$$

where  $T$  denotes the background temperature and  $\Gamma = -g/c_p$  the adiabatic lapse rate with the heat capacity at constant pressure  $c_p$ .

Yet another parameter under consideration is the gradient Richardson number  $Ri$ . It is given by the ratio between the quadratic Brunt-Väisälä frequency  $N$  and the horizontal gradient of the background wind  $\partial \bar{u} / \partial z$ :

$$Ri = \frac{N^2}{(\partial \bar{u} / \partial z)^2} \quad (2.1.6)$$

Classically a flow is considered to be dynamically unstable if  $Ri$  is smaller than  $\sim 1/4$  [cf. Lübken, 1993]. However, as described in Section 4.5, this is not confirmed by LITOS measurements.

### 2.1.3. The concept of the structure function

For a flow at high Reynolds numbers, velocity and temperature of the fluid become very sensitive to boundary and initial conditions. If the exhaust plume of a power station is considered for example, one will find that its shape is not constant in time and space at all. Even if the station is kept at constant power output and the wind speed does not change, tiny variations in the flow within the cooling tower or in the wind field will lead to a substantially different shape of the patterns in the plume. Velocity and temperature of the flow undergo random variations, they behave chaotically in space and time. The exhaust plume is a popular example for a turbulent flow, the attributes given here are equally applicable to stratospheric clear air turbulence nevertheless.

In the following section which also draws on private communication with A. Schneider, concepts of describing turbulent flows will be introduced. To further investigate velocity fluctuations mentioned above, the flow is decomposed into a mean and a fluctuating part:

$$U_i = \bar{U}_i + u_i \quad (2.1.7)$$

In order to describe whether a flow is statistically dependent at two different points in space, the correlation function in space is introduced. For velocity fluctuations with  $\bar{U}_i = 0$  it is given by

$$B_{ij}(x, x', t) = \overline{u_i(x, t) \cdot u_j(x', t)} \quad (2.1.8)$$

## 2. Turbulence theory and measurement strategies

after Mathieu and Scott [2000]. If the turbulent flow is homogeneous, then an arbitrary displacement in space  $r = x - x'$  will not change the spatial correlation function:

$$B_{ij}(x - x', t) = \overline{u_i(x, t) \cdot u_j(x', t)} \quad (2.1.9)$$

Unfortunately, in the atmosphere turbulence is not homogeneous because on large scales non-isotropic and non homogeneous events like gravity waves take place. To deal with this problem, Andrey Kolmogorov introduced the concept of the structure function  $D_{ij}$ . It is given by Tatarski [1961]:

$$D_{ij}(\vec{r}) = \overline{[u(\vec{r}_1) - u(\vec{r}_2)]^2} \quad (2.1.10)$$

If the inhomogeneities in the velocity field do not exceed the scale of  $\vec{r}_1 - \vec{r}_2$  the field is called locally homogeneous. In this case the velocity structure function is related to the spatial correlation function by Tatarskii [1971]

$$D_{ij}(\vec{r}) = 2B_{ij}(0) - 2B_{ij}(\vec{r}) \quad (2.1.11)$$

Under the assumption of a locally isotropic velocity field, the structure function reads

$$D_{ij}(\vec{r}) = [D_l(r) - D_{tt}(r)] n_i n_j + D_{tt}(r) \delta_{ij} \quad (2.1.12)$$

with  $D_{ll}$  being the longitudinal and  $D_{tt}$  the transversal structure function.  $n = \frac{\vec{r}}{r}$  is the normal vector and  $\delta_{ij}$  the Kronecker delta. For  $i = j$  this relation becomes the so called total structure function as given by Tatarskii [1971]:

$$D_{\text{tot}}(\vec{r}) = D_{ij}(\vec{r}) = D_{ll}(r) + 2D_{tt}(r) \quad (2.1.13)$$

In the following section, we will turn away from the concept of the structure function in the first place and tend to the energy spectrum of atmospheric turbulence. Thereafter, the structure function will be given for the individual subranges of the spectrum.

### 2.1.4. The energy spectrum of turbulence

The general spectrum of turbulent motions in the atmosphere shows a typical shape which can be seen in Figure 2.1. As it is important for the concept of LITOS, a brief introduction to the spectral subranges of turbulence will be given. In doing so, the course of Lübken [1993] and Theuerkauf [2012] shall be followed mainly.

The turbulent kinetic energy per unit mass  $T$  is given by the integral over the spectral energy density  $E(k)$  with the wavenumber  $k$ :

$$T = \int_0^{\infty} E(k) dk \quad (2.1.14)$$

## 2.1. The statistical approach to turbulence

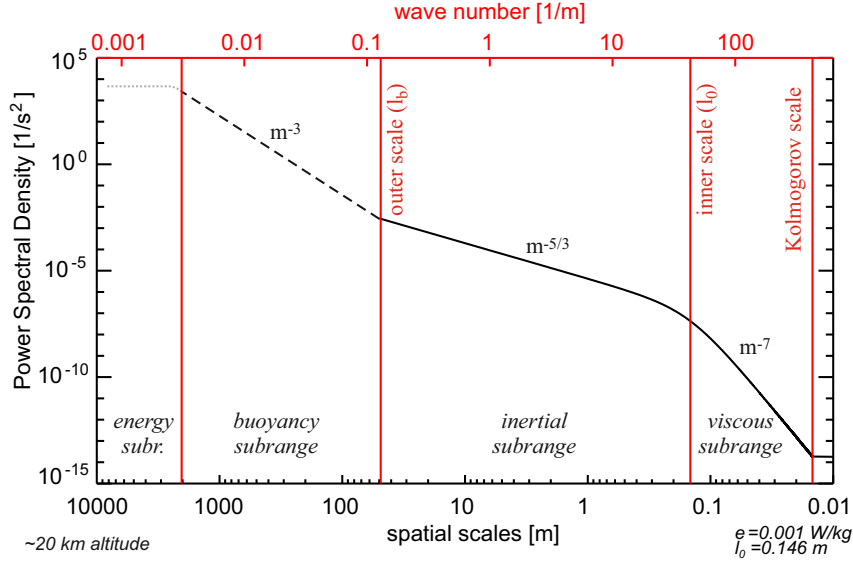


Figure 2.1.: Typical power spectrum of turbulent spectral energy density  $E(k)$  according to Lübken [1993]. Spatial scales are given for an altitude of approximately 20 km. Graphics kindly provided by M. Gerding and B. Strelnikov.

The amount of energy that is dissipated into heat per unit time is given by the so called energy dissipation rate  $\varepsilon$ . It is related to  $E(k)$  by:

$$\varepsilon = 2\nu \int_0^{\infty} k^2 E(k) dk \quad (2.1.15)$$

with the kinematic viscosity  $\nu$ . Both formulae are taken from Pope [2000]. The spectral energy density  $E(k)$  can be divided into several subranges shown in Figure 2.1. One of them is called the buoyancy subrange. It is formed by large scales. These are the scales where Rossby waves occur in the Earth's atmosphere. Here, the spectral energy density depends on the Brunt-Väisälä frequency  $N_B^2$  only. According to Lübken [1993], dimensional reasoning leads to:

$$E(k) \propto N_B^2 k^{-3} \quad (2.1.16)$$

For the inertial subrange of the energy spectrum Kolmogorov [1941] stated in his second hypothesis of similarity that the structure function may depend on  $\varepsilon$  and the scale itself ( $r$ ) only. Therefrom he derives the longitudinal structure function  $D_{ll}$  with the structure function constant for velocity fluctuations  $C_V$ :

$$D_{ll} \sim C_V \varepsilon^{2/3} r^{2/3} \quad (2.1.17)$$

Tatarskii [1971] also calculates the total structure function for the inertial subrange:

$$D_{\text{tot}} = \frac{11}{3} C_V^2 \varepsilon^{2/3} r^{2/3} \quad (2.1.18)$$

## 2. Turbulence theory and measurement strategies

As the spectral energy density is given by the Fourier-transformed of the structure function, it reads:

$$E(k) \propto \varepsilon^{2/3} k^{-5/3} \quad (2.1.19)$$

According to Heisenberg [1948], the spectrum will decay with the seventh power of the wavelength in the viscous subrange:

$$E(k) \propto k^{-7} \quad (2.1.20)$$

One way of obtaining the energy dissipation rate  $\varepsilon$  from measurements was introduced by Barat [1982]. Please see Section 2.2.1 for further details. He determined the horizontal structure function in the inertial subrange of the spectrum and deduced  $\varepsilon$  from it. The main drawback of his method is that he needs to measure absolute wind velocities and that his method depends on the use of very large balloons (10 000 m<sup>3</sup> in this case). Otherwise, the balloon gets smaller than the fluctuations that are to be measured. This means that it would float together with the velocity fluctuations, which then could not be detected by a relative wind measurement any more [Barat et al., 1984].

Another principle is used with LITOS. Instead of measuring the structure function in the inertial subrange, the inner scale of the spectrum (please see Figure 2.1) is determined by a fit over the energy spectrum. This method is introduced below.

### 2.1.5. How to determine the energy dissipation rate from the inner scale

In this section we will present the outline of a method originally developed by Lübken [1992] for density fluctuations and later applied to velocity and temperature fluctuations by Theuerkauf [2012]. The main idea of the method is to take advantage of the fact that the inner scale  $l_0$  can be related to the energy dissipation rate  $\varepsilon$  by a constant factor. The inner scale on the other hand can be obtained from a fit over the Power Spectral Density (PSD) of the velocity fluctuations measured by a constant temperature anemometer. For a technical description of the measurement process, please see Section 2.3.1. Details of the data processing routines are presented in Section 2.3.2.

According to Heisenberg [1948], the transition from the inertial to the viscous subrange can be described by:

$$V(k) = V_0 k^{-5/3} \left[ 1 + \left( \frac{k}{k_0} \right)^{8/3} \right]^{-2} \quad (2.1.21)$$

with  $V_0$  being a constant and  $k_0$  being the wavenumber that corresponds to the inner scale  $l_0$ . For the viscous subrange ( $k \gg k_0$ ),  $\left( \frac{k}{k_0} \right)^{8/3}$  is much larger than unity, therefore one gets

$$V(k \gg k_0) = \frac{V_0}{k_0^{16/3}} k^{-7} \quad (2.1.22)$$

## 2.2. How to measure turbulence in the stratosphere?

In the inertial subrange with  $k \ll k_0$ ,  $\left(\frac{k}{k_0}\right)^{8/3}$  is much smaller than unity, so the result yields Kolmogorov's formula:

$$V(k \ll k_0) = V_0 k^{-5/3} \quad (2.1.23)$$

By comparing this formula with the one dimensional spectral density as given by Tatarskii [1971] one can determine the constant  $V_0$  in favour of the structure function constant  $C_V^2$ . Furthermore, it is assumed that the turbulence does not change, while the balloon is passing it with the vertical velocity  $v_b$ . This assumption is called *frozen field hypothesis* and was first introduced by Taylor [1938]. Therefore

$$k = \frac{\omega}{v_b} \quad (2.1.24)$$

can be set. Doing so for the one-dimensional power spectrum as given in Equation 2.1.21 yields according to Theuerkauf [2012]

$$W(\omega) = \frac{\Gamma(5/3) \sin(\pi/3)}{2\pi v_b} C_V^2 \frac{(\omega/v_b)^{-5/3}}{\left[1 + \left(\frac{\omega/v_b}{k_0}\right)^{8/3}\right]^2} \quad (2.1.25)$$

This is the function which is used to fit the power spectral density of the velocity fluctuations. Hereafter this procedure shall be called *Heisenberg fit*. An exemplary result of such a fit can be seen in the right panel of Figure 2.7. By making use of a three dimensional form of this Heisenberg spectrum, comparing it to the structure function given by Tatarskii [1971] and using a certain value for the structure function constant  $C_V$ , Theuerkauf [2012] obtains the relation

$$l_0^V = 5.7 \left(\frac{v^3}{\varepsilon}\right)^{1/4} \quad (2.1.26)$$

$\nu$  is the kinematic viscosity as described in the previous section. It varies slowly with altitude and is therefore regarded as constant on the timescale of a Heisenberg fit. With the relation  $l_0 = 2\pi/k_0$  the energy dissipation rate yields:

$$\varepsilon = \left(\frac{5.7}{2\pi} k_0\right)^4 \nu^3 \quad (2.1.27)$$

$k_0$  is taken from the fit of the Heisenberg formula given in Equation 2.1.25. After this introduction to the underlying physics of the LITOS measurement method, some other ways of obtaining energy dissipation rates in the stratosphere will be presented in the following section.

## 2.2. How to measure turbulence in the stratosphere?

To give an overview on recent turbulence observations in the stratosphere we like to present three methods of obtaining energy dissipation rates in the stratosphere which are in use nowadays. The measurement principle of LITOS on the other hand is explained in Section 2.3.

## 2. Turbulence theory and measurement strategies

### 2.2.1. Balloon borne ionic anemometers

In the late 1970s, Jean Barat and co-workers developed a new method for measuring stratospheric turbulence. They used an ionic anemometer on a gondola below a zero pressure balloon. This enabled them to measure wind shear between the balloon and the gondola with an accuracy of better than 10% and a vertical resolution of about 1.6 cm [Barat, 1982]. With this anemometer, they measured the structure function  $D$  of the horizontal wind  $V_h$ :

$$D = [\Delta V_h(t + \tau) - \Delta V_h(t)]^2 \quad (2.2.1)$$

For *frozen turbulence*  $D$  corresponds to the longitudinal structure function as given in Equation 2.1.17:

$$D_{ll}(\tau) = B(\varepsilon \Delta V_h \tau)^{2/3} \quad (2.2.2)$$

With the empirical constant  $B$  and the lag distance  $\Delta V_h \tau$ , Barat [1982] calculates the energy dissipation rate  $\varepsilon$  by:

$$\varepsilon = \frac{1}{\Delta V_h \tau} \left( \frac{D(\tau)}{B} \right)^{3/2} \quad (2.2.3)$$

Initially they measured turbulent patches during the floating phase of the balloon. Later on, they increased the temporal resolution of their instrument and were thereby able to obtain profiles of energy dissipation rate during ascent [Barat et al., 1984]. Though they encountered some problems by detecting their own balloons' wake together with atmospheric turbulence, these measurements depend on less critical assumptions compared to Thorpe analysis (see below). Maybe the largest drawback is that only a few measurements have been carried out and the project was discontinued in the 1980s. Using a large 10 000 m<sup>3</sup> balloon, this method turns out to be quite demanding from a technical and financial point of view.

### 2.2.2. Thorpe analysis of radiosonde data

Another method of obtaining energy dissipation rates is by Thorpe analysis. Here one rearranges each data point of the measured potential temperature profile in a way that the new temperature profile is monotonically increasing. This is shown in Figure 2.2. The Thorpe length at a certain point in the profile is now given as the length by which the very point needs to be moved, so that the profile becomes monotonically increasing.

According to Ozmidov [1965] there is a maximum scale in a stably stratified fluid like the stratosphere, at which eddies are still isotropic. This length is nowadays called Ozmidov scale:

$$L_O \propto \sqrt{\frac{\varepsilon}{N^3}} \quad (2.2.4)$$

Here,  $N$  denotes the Brunt-Väisälä frequency. Assuming proportionality of Ozmidov and Thorpe scale with  $L_O = cL_T$ , one can obtain the energy dissipation  $\varepsilon$  by [Thorpe, 2005]:

$$\varepsilon = c^2 L_T^2 N^3 \quad (2.2.5)$$

## 2.2. How to measure turbulence in the stratosphere?

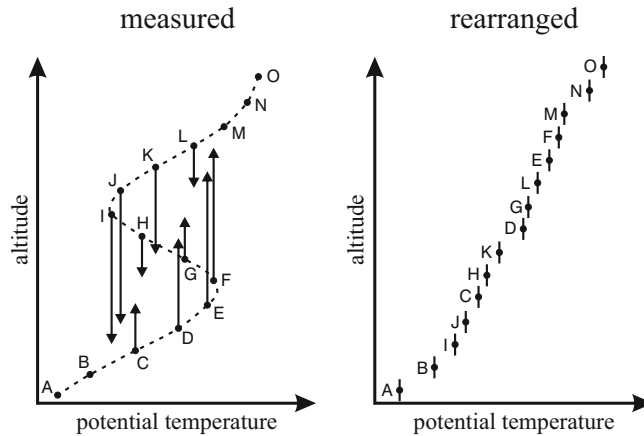


Figure 2.2.: Schematic drawing of the concept of Thorpe analysis. Graphics kindly provided by A. Schneider.

An example of turbulent parameter estimation by Thorpe analysis is the MUTSI-2000 Campaign, evaluated by Gavrilov et al. [2005]. They used high-resolution radiosondes with an altitude resolution of 0.1 m and a temperature accuracy of 2 mK. Generally, Thorpe analysis was created for observations in the ocean. Applying it to the atmosphere, it becomes evident that the *constant*  $c^2$  does not really deserve its name. According to Schneider et al. [2014] it has a distribution with a width of two orders of magnitude. Therefore one needs to take great caution when applying this concept. Though even if the mean values of  $\varepsilon$  estimations on larger scales are correct using Thorpe analysis, its value within small turbulent layers probably is not [cf. Schneider et al., 2014]. Nevertheless, the great advantage of this concept is that it can be performed using radiosonde data which have already been obtained. Therefore, a broad data set is available.

### 2.2.3. Satellite based scintillation measurements

Gavrilov [2013] provides a method of obtaining turbulent energy dissipation rates from GOMOS (Global Ozone Monitoring by Occultation of Stars). This satellite based instrument measures the intensity of a star, while its line of sight is crossing Earth's atmosphere. Air density irregularities (i.e., temperature irregularities) cause changes in the measured stellar intensity of up to several hundred per cent [Sofieva et al., 2010]. This energy dissipation measurement consists of two elements: first, air density along the line of sight is measured. Second, in a so called forward model turbulence and gravity waves are parametrised using global models. Then these parameters are fitted to the measurements. These parametrisations comprise the anisotropic structure function constant  $C_W$  as well as the inner scale  $\kappa_W$  and the outer scale  $\kappa_O$  of the buoyancy subrange. Therefore, what Sofieva et al. [2007] call the inner scale, namely the transition from the buoyancy to the inertial subrange, is called the outer scale in the terminology of LITOS. To obtain energy dissipation rates, Gavrilov [2013] needs to make use of the Thorpe analysis. These satellite based measurements provide a substantial advantage over balloon soundings: long term, global data sets are available. The author obtains turbulent energy dissipation rates in the same order of magnitude as he did with ra-

## 2. Turbulence theory and measurement strategies

diosonde measurements. Nevertheless, this does not overcome the aforementioned concerns connected to the Thorpe principle, as both measurements rely on this analysis. Furthermore, GOMOS data processing is very complex and may be a source of error itself. The author states: “Correlations between parameters of anisotropic and isotropic perturbation spectra [...] can be partly due to procedures of GOMOS data processing. For example, parameters  $C_W$ ,  $\kappa_O$ ,  $\kappa_W$  are calculated simultaneously and could have relations through mathematical expressions.” [Gavrilov, 2013]

### 2.3. The measurement principle of LITOS

In this section the basic concepts of energy dissipation rate measurements with LITOS will be presented. This comprises a description of the anemometer and the data processing routines as well as the presentation of typical measurements in dependence on parameters like the window width used for the Heisenberg fit.

#### 2.3.1. CTA measurement principle

The flight train of LITOS can be seen in Figure 2.3. The balloon is moving alongside the background wind. The sensor of the Constant Temperature Anemometer (CTA) undergoes a heat loss  $Q$  which is proportional to the horizontal relative wind  $u_r$  between the balloon and LITOS payload. In other words, the CTA measures the vertical alteration of the horizontal wind. Additionally to the CTA, the main payload is equipped with a radiosonde that measures important atmospheric background parameters like temperature, wind and humidity. For further information on technical aspects of the payload design, please see Section 3.2.

The underlying principle of a CTA is to heat a thin wire (in our case the diameter is  $5\ \mu\text{m}$ ) above the temperature of the ambient flow and measure the current that is needed to keep its temperature constant. The fluid flow leads to convective cooling of the wire, which is made from platinum-plated tungsten. The material’s resistance features a linear dependence on temperature. Hence, the flow evokes a change in the resistance of the wire, which is related to the velocity of the flow. This relation was examined by King [1914] who derived a formula for the heat loss of a thin wire due to convection depending on air speed, which later on became known as *King’s law*. It shows a logarithmic behaviour for low speeds and an asymptotic behaviour for high speeds.

In case of LITOS, this wire is heated by a bridge circuit. As it is shown in Figure 2.4, the hot wire forms one leg of a Wheatstone bridge. If the wire resistance changes, the bridge gets out of balance. This will result in a difference voltage between A and B which is amplified and fed back into the bridge in a way that makes the bridge adjust itself to a new metastable state. Further information on CTA measurements can be obtained from Durst [2008]. In our case, the output signal of the servo amplifier depends on the wind velocity and is digitised using custom made data acquisition electronics.

Furthermore, this curve depends on the ambient air pressure as well. Therefore, measuring absolute values of wind speed with LITOS would require a calibration depending on wind speeds between 0 and 15 m/s, pressures between 10 and 1000 hPa and temperatures between

### 2.3. The measurement principle of LITOS

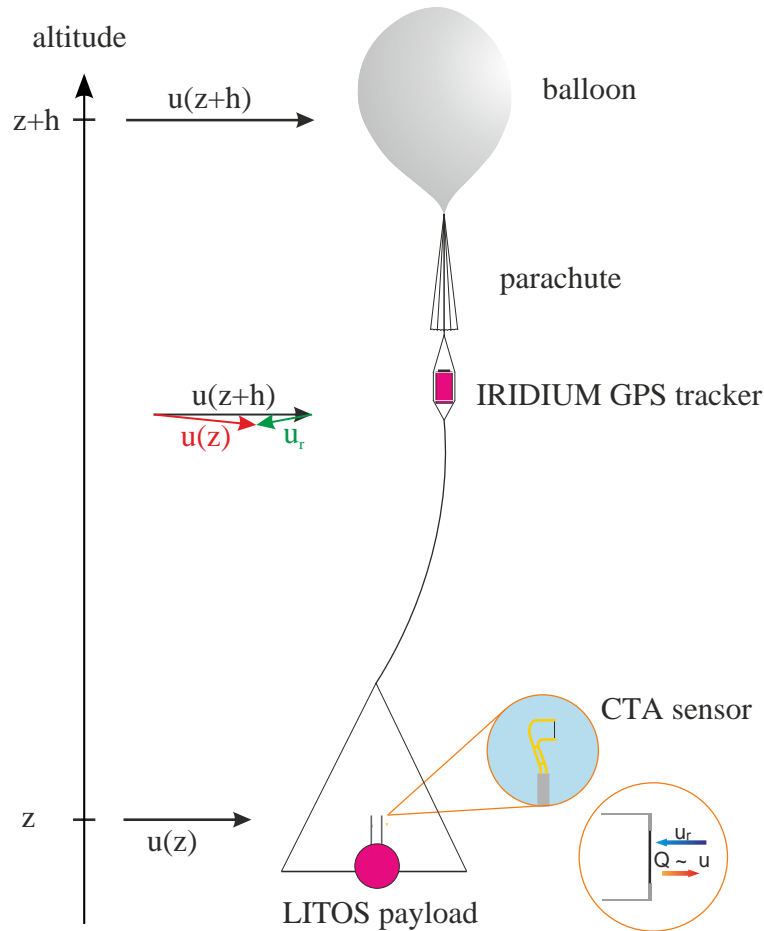


Figure 2.3.: General measurement principle of LITOS shown for the small payload.  $Q$  represents the heat loss of the wire and  $u_r$  the relative wind between the balloon and LITOS. The distance  $h$  between the balloon and the payload is typically 150 m.

210 and 300 K. This is not available so far. Fortunately, LITOS resolves the inner scale of turbulence. Therefore, the method described in Section 2.1.5 which does not require absolute measurements of air speed can be applied. The only requirement is that measurement conditions do not change substantially within the course of one Heisenberg fit (i.e., in an altitude range of 5 to 10 m). According to Theuerkauf et al. [2011] this is fulfilled in the entire altitude range of LITOS. As shown in Figure 2.3, the CTA sensor is not rotationally symmetric. Sumińska [2008] has pointed out that this lack of rotational symmetry results in a yaw effect of 15-20 %. Hence, measurements require a rather low speed of gondola-rotation. Please regard Section 3.1 for details. For further information on temperature and pressure dependence of CTA measurements, please see Theuerkauf et al. [2011].

## 2. Turbulence theory and measurement strategies

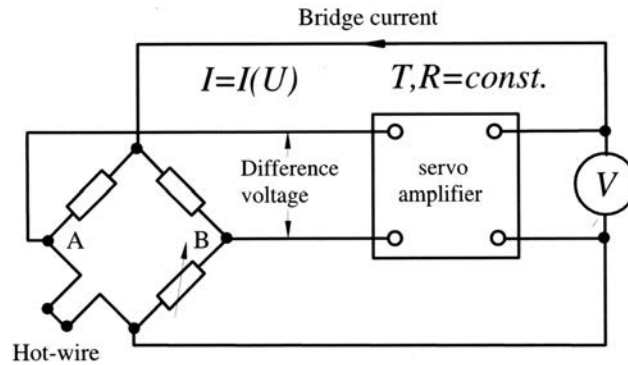


Figure 2.4.: General electrical circuit of a constant-temperature anemometer (CTA) taken from Durst [2008]

### 2.3.2. Data processing

Once information is read from the SD-Card after payload recovery, data processing routines need to be applied to finally retrieve a profile of the energy dissipation rate  $\varepsilon$ . This process shall not be reviewed in full detail here. Nevertheless, a brief description to introduce the reader to the basic concepts will be given here.

The data set can be divided into three branches: CTA voltages and housekeeping data are stored on the SD-card, whereas radiosonde measurements are constantly transferred to the ground station via radio communication during the whole flight. These three subsets need a different treatment each, which is visualised by the flowchart in Figure 2.5. These general data retrieval tools were already set up and implemented in MATLAB by A. Haack and A. Schneider when I joined the team at IAP.

The task was to adapt these tools to the special requirements of the small scale LITOS payload. As mentioned in Section 3.2.4, instead of using a Constant Current Anemometer (CCA) and a CTA, two CTAs were taken on-board. The procedure of the Heisenberg fit itself is depicted in further detail in Figure 2.6.

Before discussing the different steps of the data acquisition routine, an outcome of a typical example of such a fit will be presented. In Figure 2.7 the CTA-voltage signal and the corresponding power spectral density are given together with the Heisenberg fit. The programming flowchart in Figure 2.6 shows that the raw data of a certain altitude window need to undergo a spline-fit or mean value subtraction. If the spline subtraction is chosen, one has to set the supporting width of the spline fit. Many turbulent layers are only about two meters thick. The spline fit requires at least three supporting points. Therefore, they would be only 0.7 m apart. As visible in the right panel of Figure 2.7, the fit range starts at spatial scales of 2 m. This means that the Heisenberg fit would be biased by the spline subtraction. Accordingly, all data presented in this thesis have been generated by subtracting a running mean instead of a spline fit. The spline fit method is useful nevertheless, when applied with a larger altitude window.

Before running the Heisenberg fit procedure, the PSD data set needs to be smoothed, because otherwise the data set is too noisy. Here it was chosen to smooth on a logarithmic x-axis, because the Heisenberg fit is also done on logarithmic data. Smoothing on a linear x-axis would

### 2.3. The measurement principle of LITOS

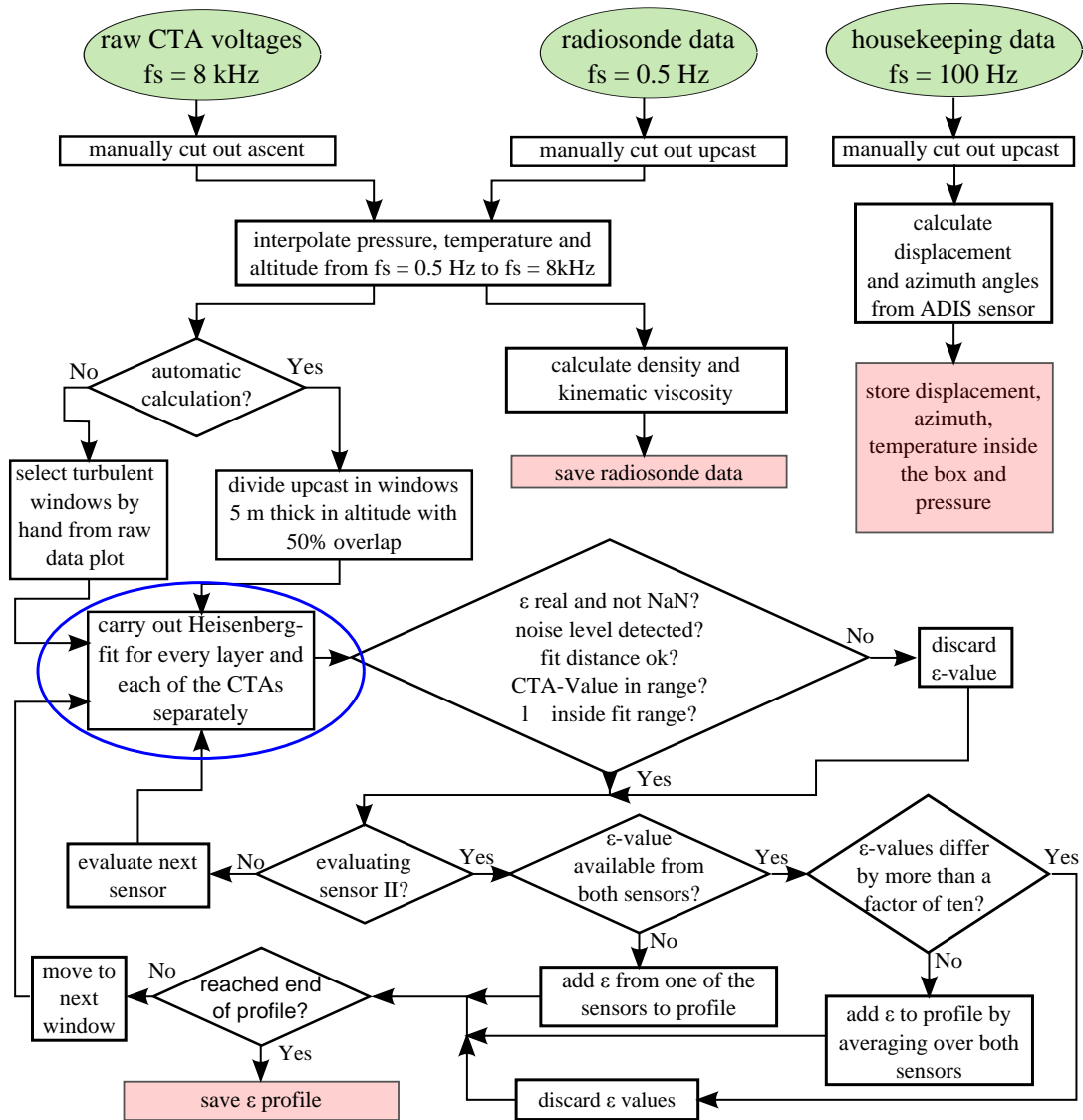


Figure 2.5.: Programming flowchart of LITOS data processing. The subroutine marked in blue is shown in further detail in Figure 2.6.  $f_s$  denotes the sampling frequency of the respective data set.

2. Turbulence theory and measurement strategies

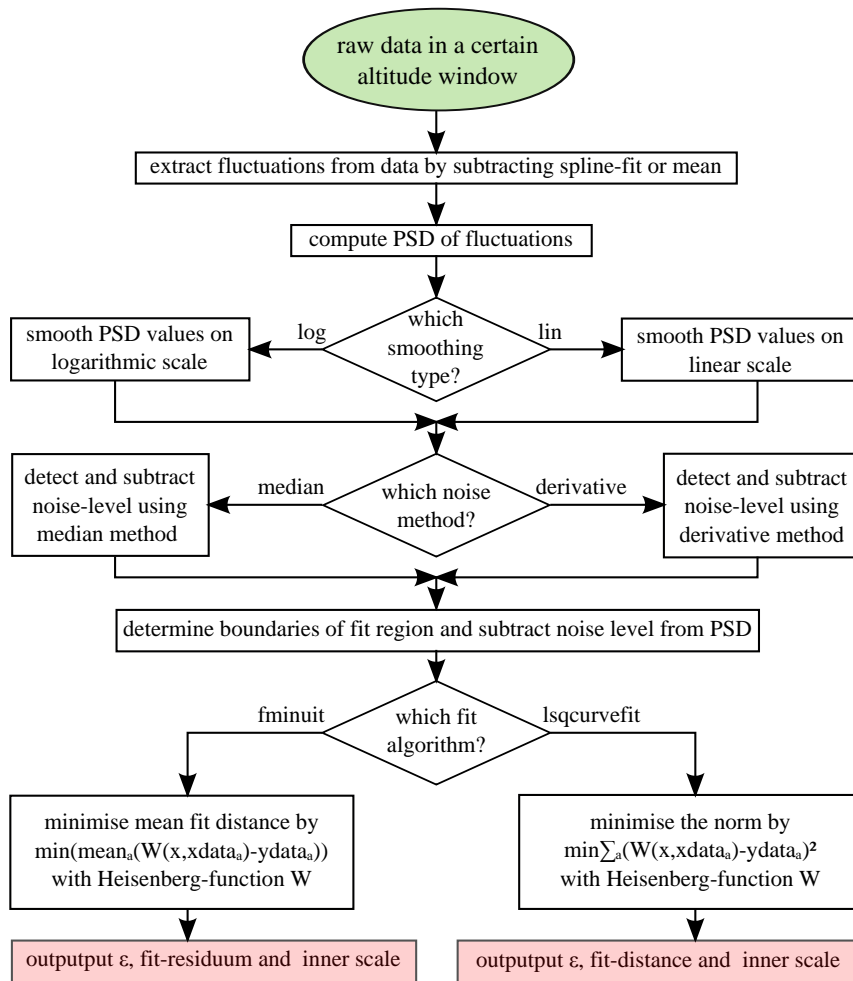


Figure 2.6.: Programming flowchart of Heisenberg fit procedure. This is a detailed representation of the blue circled subroutine from Figure 2.5. The Heisenberg-function  $W$  is described in Section 2.1.5.

### 2.3. The measurement principle of LITOS

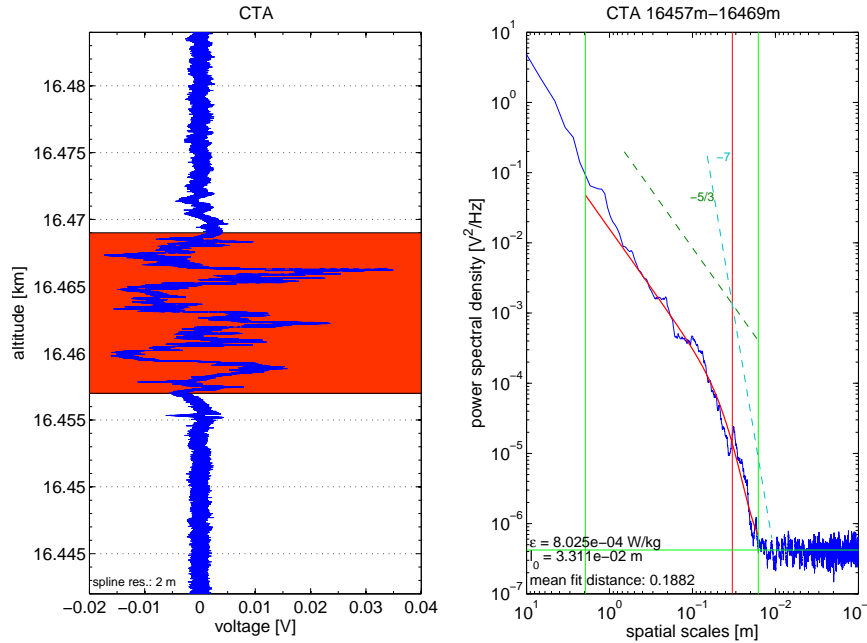


Figure 2.7.: Typical example of a turbulent layer in the lower stratosphere. The left panel shows fluctuations of the CTA voltage. The turbulent area is marked in red. For better depiction, a spline with a supporting width of 2 m is subtracted. The right panel visualises the power spectral density of CTA voltages in the turbulent patch. The vertical green lines show the fit range, whereas the horizontal ones marks the noise level. The slopes of the inertial and the viscous subrange are shown by the dashed lines. In the lower left corner, values are given for the energy dissipation rate  $\epsilon$ , the position of the inner scale  $l_0$  and the mean distance between the fit and the data curve.

therefore mean that the Heisenberg fit is not done on a linearly spaced grid. Large scales would contain much less data points than small scales. To avoid this, data smoothing on a logarithmic x-axis was chosen.

After smoothing the power spectral density, the noise level needs to be subtracted. This is one of the most critical points in data retrieval. If the noise level is improperly detected, this has a huge impact on the fit procedure itself. In other words: a failure of the fit often is down to a bad noise estimate.

Up to now, the noise level was detected by taking the median of all data with a frequency between two thirds of the maximum frequency and the maximum frequency. This method is fairly stable, but becomes problematic, if either the frequency range where the spectrum reaches noise level is very small, or perturbations exist on the data at high frequencies. In the course of the instrumental development described here another more precise method was developed which so far is not in use for the automatic calculation of  $\epsilon$ -profiles. This is because the higher stability of the median method results in a higher steadiness against non-atmospheric oscillations described in Section 3.2.4. The new method is described in Appendix A.1.

After the fit region has been determined and the noise level is subtracted from the data set, the fit itself is carried out. To do so, the power spectral density is fitted to Heisenberg's in-

## 2. Turbulence theory and measurement strategies

terpolation formula given in Section 2.1.4. For every evaluation shown in this thesis, the FMINUIT fit algorithm has been used. It was originally developed at CERN and implemented in FORTRAN 77 and is based on the MINUIT minimisation engine [Allodi, 2010]. It has two advantages over MATLAB's `lsqcurvefit` algorithm: for one thing the user can choose the function that is to be minimised himself. In our case, the mean distance between the fit-curve and the logarithmic data points is minimised. Therefore, contrary to the `lsqcurvefit` procedure, the residuum of the fit becomes independent of the length of the data set that is used for the fit. For another thing, FMINUIT outputs an estimate for the fit error, which will be used to determine the error of the  $\varepsilon$ -calculation. This method is still under development (A. Schneider, private communication). Hence no further details will be provided here and no confidence limits for the energy dissipation rates or other fit parameters can be given. In conclusion, the Heisenberg fit as depicted in Figure 2.6 calculates the energy dissipation rate  $\varepsilon$ , the mean fit distance and the inner scale  $l_0$  for a certain altitude window from raw CTA voltages.

When speaking about the automatic calculation of an  $\varepsilon$ -profile, one is mainly concentrating on the processes mentioned in the lower half of the flowchart shown in Figure 2.5. Generally, for an automatic calculation the entire data set is divided into sublayers, which are all treated as potentially turbulent. For every layer and each input channel the Heisenberg fit is carried out separately. For all fits the fitted parameters are checked for certain criteria, which allow to determine whether the results are sensible or not. These criteria are:

Table 2.1.: Evaluation criteria for the Heisenberg fit as used on the turbulence data discussed in Chapter 4. If one of these criteria is regarded as FALSE, the respective  $\varepsilon$ -value is set to NaN.

Name	Required values
Is $\varepsilon$ a real number?	YES
Noise-level detection successful?	YES
Fit distance small enough?	$\text{fit} - \text{dist} < 0.4$
$\varepsilon$ -value in range?	$0 < \varepsilon < 100$
$l_0$ inside fit range	YES
Both $\varepsilon$ available and in similar range?	$ 10^{\varepsilon_1} - 10^{\varepsilon_2}  < 10$

Sometimes, the FMINUIT engine returns a complex value for epsilon. This cannot be the proper result of a physical measurement. Therefore, these values are discarded as computational artefacts. Obviously, the  $\varepsilon$ -calculation can be carried out only, if the noise level and therefore the borders of the fit range were determined successfully. For spectra with a turbulence level as low as the one given in Figure 2.8 there is no visible transition from the inertial to the viscous subrange and they usually reveal a large fit distance. This is because even if the data contains only atmospheric noise and hardly follows the expected  $-5/3$  and  $-7$  power law, the fit routine will find a local minimum and converge. Nevertheless, this fit cannot be trusted because there is no physical meaning at all. The value of 0.4 for the maximum fit-distance was chosen from experience. The expected range for  $\varepsilon$  is given by physical reasoning: a negative energy dissipation rate does not have any physical meaning at all. From examining various spectra, it is known that  $\varepsilon$ -values larger than 100 are usually

### 2.3. The measurement principle of LITOS

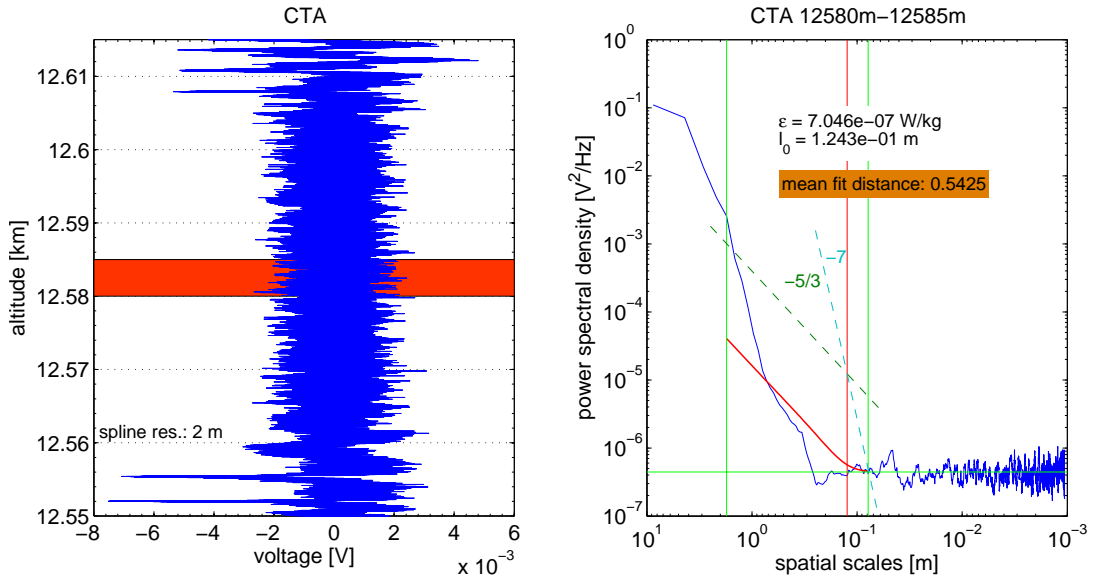


Figure 2.8.: Fit result for one of the CTA sensors in a non-turbulent area. The fit routine determines a position of the inner scale though there is no transition from the  $-5/3$  to the  $-7$  power range visible. Of all criteria from Table 2.1, *fit distance* is the only one to fail.

down to errors in the fit-procedure. Even if they would exist in the atmosphere, they could not be measured by LITOS. In the case of very large  $\epsilon$ -values, the noise level moves to such high frequencies that it overshoots the maximum frequency of 4 kHz and cannot be detected anymore. Therefore these fits need to be discarded. As the reader will be aware of, the inner scale cannot be outside the fit-range, because in this case the transition between both power regimes cannot be fitted. Therefore, these  $\epsilon$ -values are disposed as well.

With the onset of using the new LITOS payload, there is another evaluation parameter available: if all of the criteria mentioned above are positive for both sensors, their  $\epsilon$ -values are compared and expected to be no more than a factor of ten apart. If only one of the sensors delivers an  $\epsilon$ -value, this value is taken for real and not discarded. This is done because if one sensor shows turbulence and the fit of the other crashes this is usually down to oscillations on the signal as described in Section 3.2.4. Under these circumstances it is more realistic to use the single sensor measurement instead of marking the layer as non-turbulent.

When evaluating a data set not only the criteria given in Table 2.1 are important. Also the size of the evaluation window plays its part. Previously, the BEXUS flights were analysed using a 25 m window on the data set. By manually selecting all turbulent areas from the raw data fluctuations, it was found that many layers are only 10 m or even less in altitude. Therefore it was decided to reduce the window size to 5 m. From Figure 2.9 one can see that window size indeed matters. With a 25 m window, the whole coloured altitude range would have been marked as turbulent with  $\epsilon = 25 \text{ mW/kg}$ . Using a 5 m window instead results in the correct detection of two separate turbulent layers with  $\epsilon = 11 \text{ mW/kg}$  for the first and  $\epsilon = 50 \text{ mW/kg}$  for the second. Using even smaller windows results in increasingly large errors due to the lower number of data points.

## 2. Turbulence theory and measurement strategies

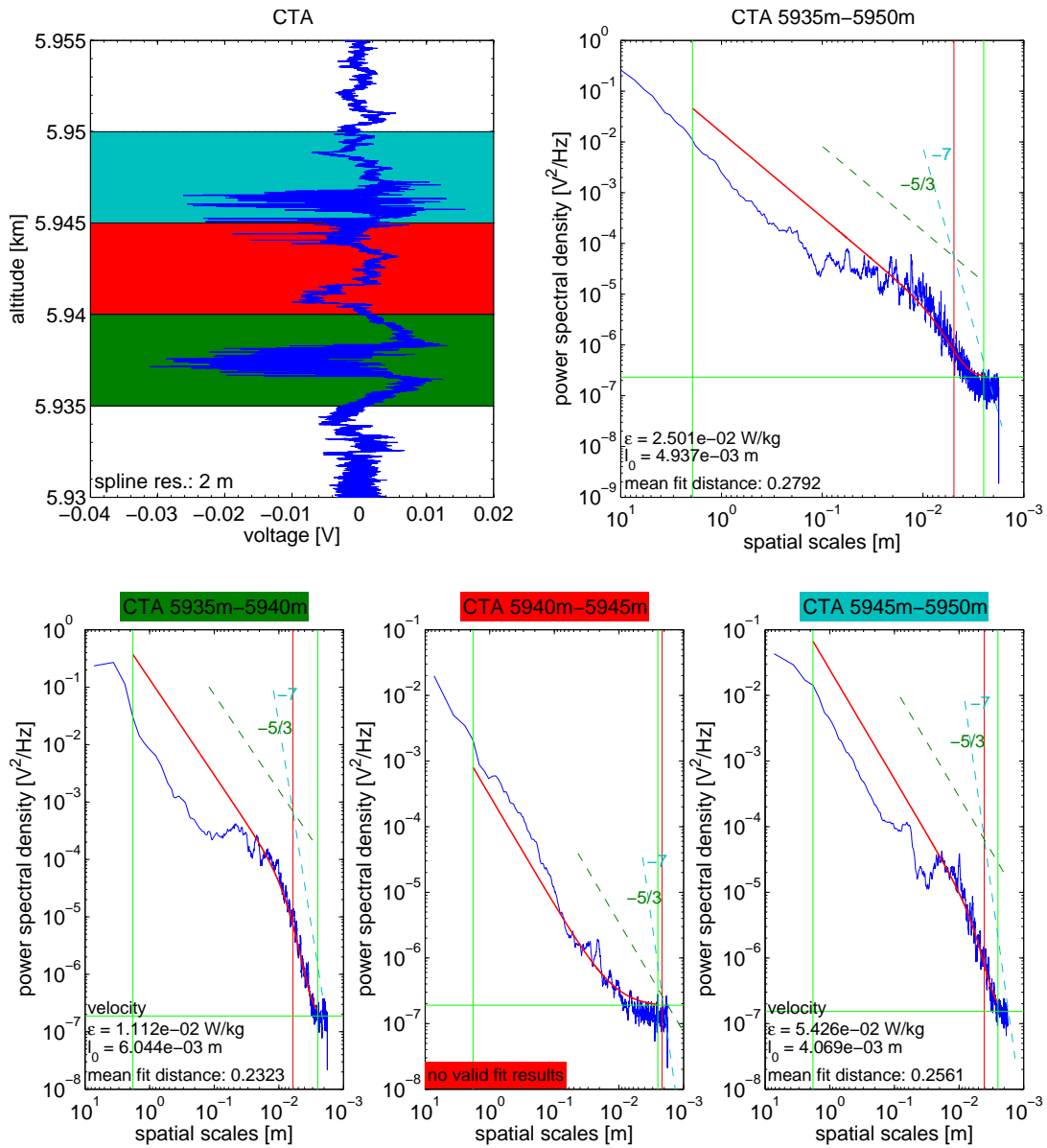


Figure 2.9.: Comparison of different window sizes: Top-left panel shows voltage fluctuation with three layers with a width of 5 m marked by colours. The top-right panel shows a fit with a 25 m window size, as it was used with LITOS previously. The lower panels show that although the whole area is seen as turbulent with a 25 m window, actually just the green and light blue areas are turbulent. The red area does not show a transition from the  $-5/3$  to the  $-7$  power range, therefore the fit fails ( $l_0$  is outside of the fit-range) and the area is not marked as turbulent.

## 3. Payload development

Up to now, successful measurements with LITOS have been performed on several BEXUS campaigns. Nevertheless, with this programme neither the time nor the site of launch can be chosen according to geophysical criteria. Therefore, IAP aims to perform regular soundings on a small-scale payload weighing below five kilogrammes. The weight limit is given by the German aviation authority. Accordingly, a new payload design was to be developed. It needs to house all the components, save them from environmental impact and ensure a sufficiently stable flight (Section 3.2). As the payload still needs to be recovered for data retrieval, an improved flight path prediction plays a crucial role when planning regular flights from launch sites near the sea (Section 3.3).

### 3.1. Pendulum calculation

In order to avoid the measurement being disturbed, it is important to keep the movement of the gondola as low as possible. As a first clue to the frequency range of these motions one can regard the gondola below the balloon as a mathematical pendulum. This leads to the following assumption for the period  $T_0$  of the gondola:

$$T_0 = 2\pi \sqrt{\frac{l}{g}} \quad (3.1.1)$$

with  $l = 150$  m being the usual balloon-gondola distance for the small-scale payload and  $g$  the gravitational constant. This yields

$$T_0 = 27 \text{ s} \quad (3.1.2)$$

Generally, the motions of the gondola consist of two constituents: pendulum motions below the balloon and rotational motions around its horizontal axis. The former create periodic changes of the wind speed. Assuming an ascent rate of 5 m/s the pendulum period  $T_0$  of the gondola results in additional signals on the PSD of the wind fluctuations at spatial scales of 135 m. During data evaluation, these scales are cut off by the background subtraction. Rotational motions alone also do not cause problems because they create low wind speeds around the sensors. However, the combination of rotational and pendulum motions in a wind field will cause trouble: sudden changes in the direction of flow around the CTA sensor will disturb relevant parts of the spectrum, because of the yaw dependence of the CTA sensor, which is evaluated by Sumińska [2008]. As both types of gondola movement cannot be completely avoided, it is important to reduce both of them as much as possible. Rotational motions can be best avoided by using a design with rotational symmetry. For the pendulum motions, two effects are important: on the one hand side a large drag coefficient will damp

### 3. Payload development

oscillations of the gondola. On the other hand side this will provide a large windage that drives the oscillations. The all important question is which effect prevails.

As the cord length between the balloon and the gondola is about 150m, crucial laboratory experiments on this question are impossible to perform. Hence, the system shall be modelled by a damped, forced pendulum. First attempt was to use a linear pendulum with the following differential equation:

$$0 = ml \frac{d^2 \phi}{dt^2} + mg \sin(\phi) + F_{\text{damp}} - F_{\text{drive}} \quad (3.1.3)$$

with  $m = 5 \text{ kg}$  being the mass of the payload,  $g$  the gravitational constant,  $\phi$  the angle of displacement,  $F_{\text{damp}}$  the force damping the pendulum by friction and  $F_{\text{drive}}$  the external force driving the pendulum. For a turbulent flow around the gondola this wind forcing is given by the wind drag on the gondola according to Wikipedia [2014a]:

$$F_{\text{drive}} = R \frac{1}{2} \rho v^2 C_d A \quad (3.1.4)$$

Here  $\rho$  is the air density,  $v$  the wind speed,  $C_d$  the drag coefficient and  $A$  the cross section area of the payload. This model only uses a pendulum with one degree of freedom, namely  $\phi$ . Therefore, the different angles between the wind forcing and the plane of motion are accounted for by a randomly distributed factor  $R$  with  $-1 < R < 1$ . The damping force  $F_{\text{damp}}$  for turbulent friction increasing quadratically with speed is analogously given by

$$F_{\text{damp}} = \frac{1}{2} \rho C_d \left( l \frac{d\phi}{dt} \right)^2 A \quad (3.1.5)$$

with  $l = 150 \text{ m}$  denoting the distance between balloon and gondola. In the following table, diameters of the different payload types are presented. The second line shows drag coefficients  $C_d$  of both types as given by Hucho [2011].

payload type	sphere	wind vanes
diameter [m]	0.15	0.25
drag coefficient	0.25	1.2

For the simulation, the differential equation 3.1.3 is solved using Runge-Kutta 4<sup>th</sup> order method. The wind field driving the motions was taken from an exemplary radiosonde ascent. In Figure 3.1 results are given for the two different payload shapes. It can be seen that the wind forcing increases until 2000 s after launch and decreases rapidly thereafter. The increase is caused by the speed of the specific wind field, whereas the decrease is down to the air density diminishing exponentially with altitude. The displacement angle  $\phi$  of both payloads pretty much follows the wind forcing until 2000 to 3000 s after take off. Later on, friction as well as forcing becomes so low that the payload with the wind vanes mainly preserves its maximum deflection angle. The spherical one on the other hand shows a decreasing maximum angle first, which at 4000 s after launch starts to increase slowly again. Most important result of this simple model is that a spherical payload with a low drag coefficient will

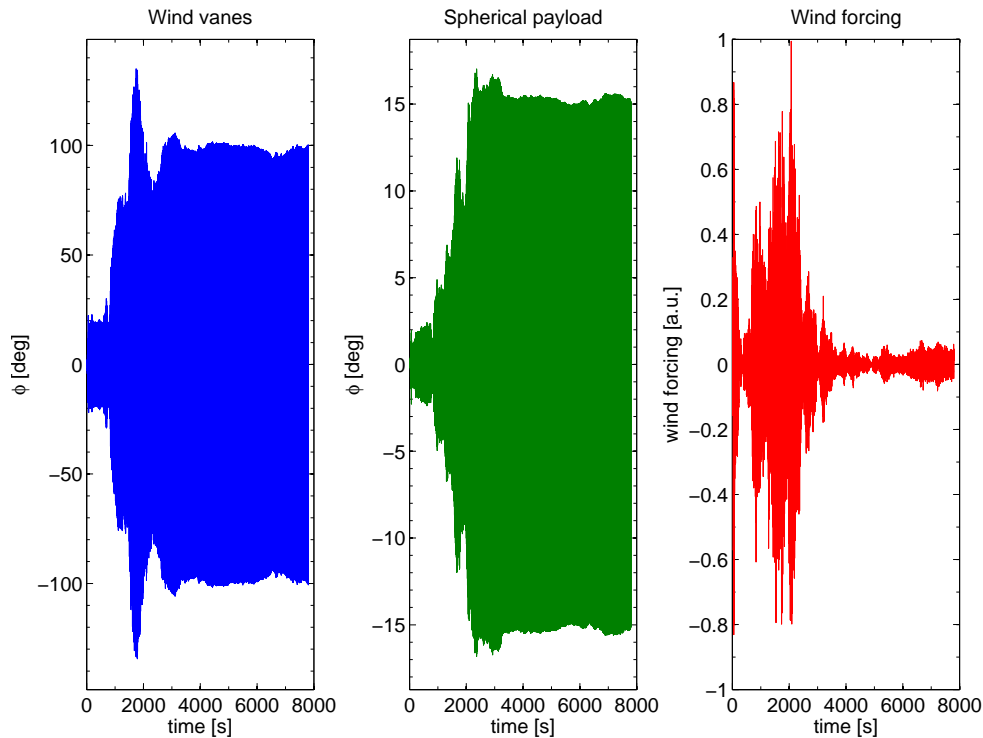


Figure 3.1.: Simulated displacement angles  $\phi$  are given for both payload shapes as well as the wind-forcing. The later is taken from an exemplary radiosonde measurement on 25<sup>th</sup> of February 2011 at Kühlungsborn.

have a displacement angle that is approximately four times lower than the one with the wind vanes. Certainly, this model is a simplified approximation. To get a more detailed picture, one would need to simulate a three dimensional spherical pendulum. Furthermore, in reality the wind forcing is not only determined by the wind speed, but by a superposition of the wind speed and the speed of the gondola. Additionally, the real flight train of LITOS constitutes a double pendulum and bobbing motions of the rubber-made balloon contribute to the driving forces as well. All in all, the real system is highly complex and probably even chaotic. Therefore it does not seem possible to achieve a comprehensive solution in the given period of time. Nevertheless we can conclude even from this simplified model that a spherical payload with a drag as low as possible will significantly reduce pendulum motions. This outcome is confirmed by the new LITOS payload, as shown in Section 3.2.1.

## 3.2. Payload design

### 3.2.1. Payload shape

The latest design of a small payload before I joined the team at IAP was flown in 2011 as shown in Figure 3.2. This LITOS payload featured the electronics inside a quadratic box made of polystyrene. The radiosonde was attached with a dereeler below LITOS, whereas the tracking system was placed above. The distance between the balloon and LITOS was about

### 3. Payload development



Figure 3.2.: LITOS payload in 2011

100 m. Three large wind vanes were used to decelerate pendulum and rotational motions (cf. Theuerkauf [2012]). Later on after some wind channel testing, it was decided to opt for a spherical payload in order to improve the flow around the gondola (A. Schneider, M. Gerding, private communication). This shall avoid rotational motions of the gondola. The diameter of the payload was reduced to 30 cm, compared to an edge length of the previous payload of 35 cm. Also the wind vanes shown in Figure 3.2 were omitted. Their intend was to reduce pendulum motions of the gondola. Nevertheless they make handling more complicated. Furthermore, in the course of this work simulations on pendulum motions have been done (please see previous section). They indicate that it is best to use a payload design with a mass density as high as possible. Figure 3.3 shows the raw data of the polar angle of the payload below the balloon for both configurations. Generally, all data considering position and speed of the gondola where acquired using the tri-axis accelerometer, gyroscope and magnetometer ADIS16407 by Analog Devices Inc. Data retrieval software was kindly provided by A. Schneider. With the new design, the accelerometer was mounted upside down and slightly tilted, which makes the polar angle fluctuate around  $176^\circ$ . Data in altitudes below 1200 m have been removed because they were perturbed by the unwinding dereelers.

As visible from the spline-removed data shown in Figure 3.4, the fluctuation in polar angle is much lower for the new design. A measure for the amplitude of the fluctuations is given by the standard deviation  $\sigma_\theta$  of the polar angle  $\theta$ .

$$\sigma_\theta = \sqrt{\frac{1}{n-1} \sum_{i=1}^n (\theta_i - \bar{\theta})^2} \quad (3.2.1)$$

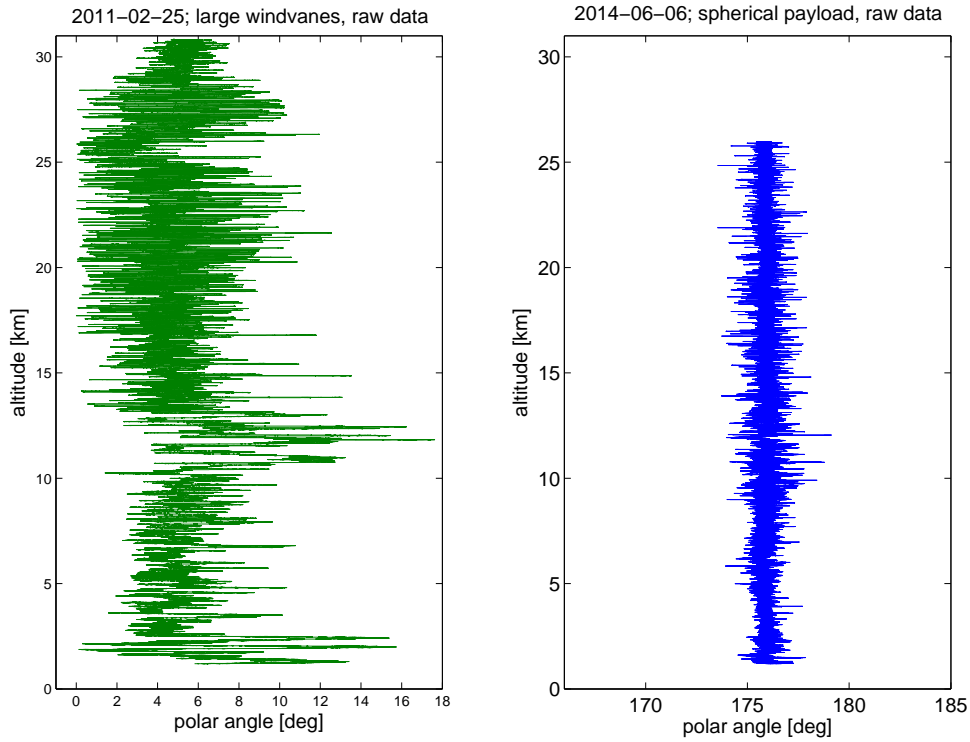


Figure 3.3.: Displacement of the gondola for two different payload shapes. Raw data without spline subtraction are shown here.

where  $\bar{\theta}$  denotes the mean polar angle

$$\bar{\theta} = \frac{1}{n} \sum_{i=1}^n \theta_i \quad (3.2.2)$$

In absolute figures, the standard deviation was reduced from  $\sigma_{\theta} = 2.1^{\circ}$  for the old design to  $\sigma_{\theta} = 0.7^{\circ}$  for the new one. This is a reduction by a factor of three.

Besides, the pendulum motions of the gondola below the balloon rotational motions of the gondola around its vertical axis need to be evaluated. Figure 3.5 reveals that on 25<sup>th</sup> February 2011 there was less rotation of the payload in the troposphere, compared to the stratosphere. This was exactly the other way round on 6<sup>th</sup> June 2014. The difference is caused by different weather conditions. In the third panel of the plot the wind speed measured by the radiosonde is shown. In the troposphere there was less wind speed on 25<sup>th</sup> February 2011, whereas the stratospheric wind was weaker on 6<sup>th</sup> June 2014. The standard deviations calculated according to Equation 3.2.1 are nearly the same for both flights (11.5 deg/s compared to 11.3 deg/s). For further information on the position of the gondola below the balloon, two or more video cameras were mounted on the payload during all flights. From these videos it can be seen that the old payload shows an oscillation around a fixed position, whereas the new payload tends to be rotating more freely. This is confirmed by Figure 3.5: especially in the stratosphere the first flight shows much more maxima and minima in angular velocity than the second one. This corresponds to many changes in direction of rotation. Unfortunately,

### 3. Payload development

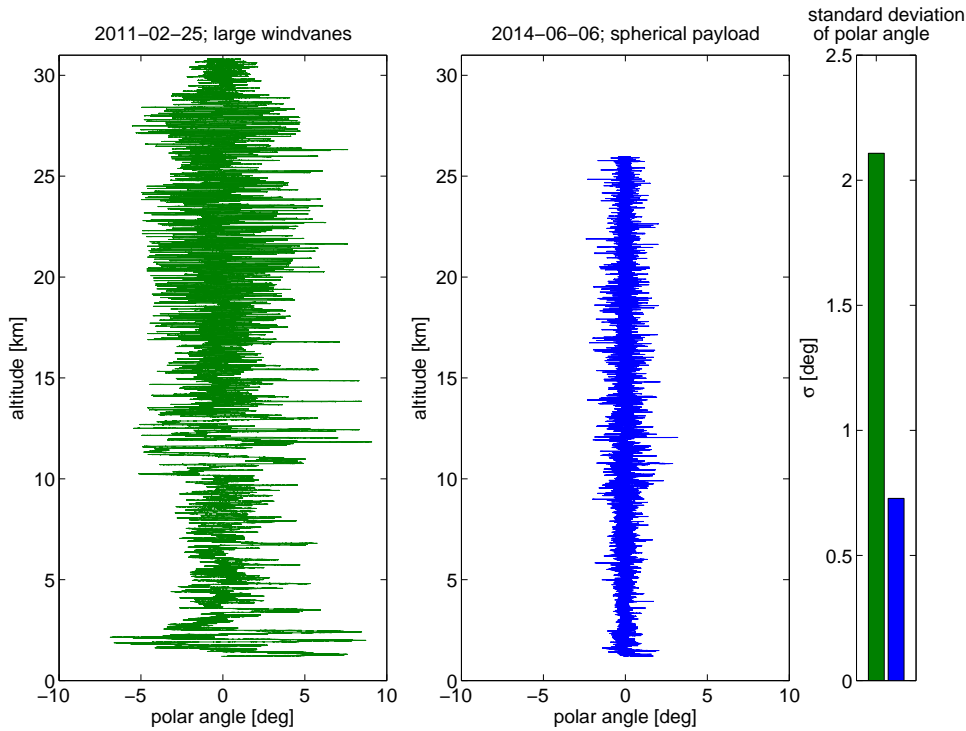


Figure 3.4.: Comparison of polar angle. Spline subtraction with a supporting width of 1000 m is applied.

a comparison of the absolute azimuth angles is not possible, because the magnetometer was shielded by the boxing during the last flight.

All in all it can be said that the new payload shape has largely reduced the displacement of the gondola, whereas it did neither improve nor worsen the velocity of rotational motions, but reduced the number of changes in direction.

#### 3.2.2. Payload mounting

Another cause for high frequency disturbances on turbulence data can be oscillations of the payload due to a twist against gravitational force. If this occurs, the restoring force is the following torsional moment  $M$ :

$$M = m_{\text{payload}} g l_v \quad (3.2.3)$$

$l_{v1}$  denotes the lever arm of the gravitational force. This strongly depends on where the strings are attached to the payload. In Figure 3.6 one can see the difference in lever arm lengths between the old ( $l_{v1}$ ) and the new ( $l_{v2}$ ) configuration. As  $l_{v2}$  is more than three times longer than  $l_{v1}$ , the restoring force with the new design is more than three times higher compared to the old one. The rods at the bottom of the gondola are made of carbon fibre reinforced plastic. In the first version an outside diameter of 8 mm and a wall thickness of 1 mm were used. The ultimate load was tested and found to be 42 kg. This means that the design would withstand an acceleration of 8 g.

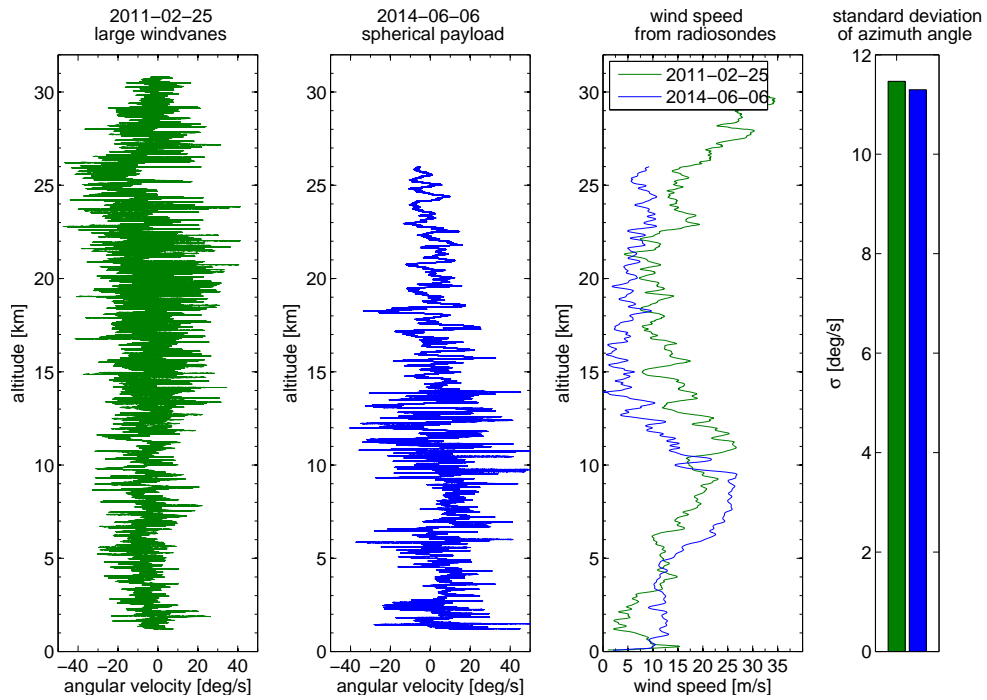


Figure 3.5.: Angular velocity of the gondola in azimuth direction for two different payload shapes. The third panel shows wind speeds for both flights, whereas the fourth one shows standard deviation of angular velocity.

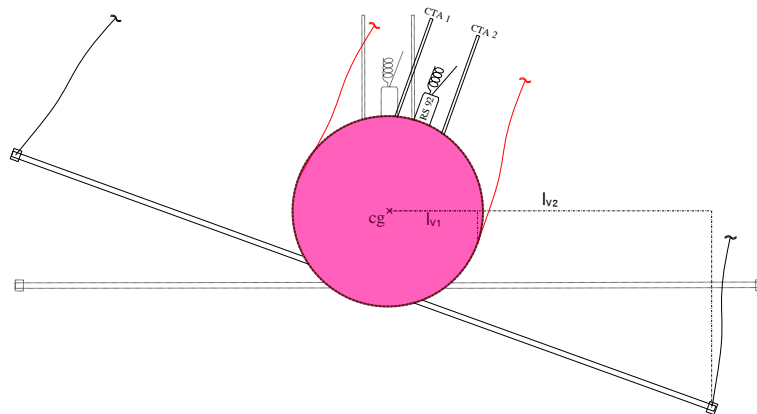


Figure 3.6.: Lever arm of gravitational force on LITOS for a rotation of  $20^\circ$ . The red lines indicate that the box is attached as it was done until 2011, the black ones show the new design.  $l_{v1}$  and  $l_{v2}$  point to the different lever arms and  $cg$  to the centre of gravity.

### 3. Payload development

Nevertheless, the first flight with the new design on 25<sup>th</sup> November 2013 showed that vibrations of the payload on the carbon rods were induced. They are to be seen on the videos, in the raw data of the CTA instrument and on the accelerometer connected to the data acquisition electronics. They have a frequency of about 4.8 Hz and are indicated by the arrow pointing to the green data set in Figure 3.7. This plot was created by running a FFT on z-acceleration data of the whole flight. The frequency of these oscillations has been reproduced in the lab by holding the payload at the ends of the rods and inducing some oscillations at the characteristic frequency of the system by hand. They disturb the turbulence measurements because their frequency is already in the frequency range of the Heisenberg fit and by this they are among the main issues which prevent a successful turbulence evaluation of the data set from 25<sup>th</sup> November 2013. Therefore they need to be avoided by reinforcing the carbon rods holding the payload. According to Wikipedia [2014b] the section modulus ( $\sim$  bending stiffness) of a tube is given by:

$$S = \frac{\pi}{32} \frac{(D^4 - d^4)}{D} \quad (3.2.4)$$

$D$  points to the outside diameter,  $d$  to the inside diameter of the tube. Therefore, increasing the outside diameter from 8 mm to 13 mm with a maintained wall thickness of 1 mm will increase the bending stiffness by a factor of:

$$\frac{S_{13}}{S_8} = 3.06 \quad (3.2.5)$$

For all consecutive flights, carbon fibre tubes with a woven finish were used instead of pultruded ones. They show a better elastic modulus, which results in a higher bending stiffness. As can be see from the blue curve in Figure 3.7 the improvements stopped the oscillations. This impression was confirmed by the videos and the CTA measurements (data not shown here).

Both curves in Figure 3.7 show a pronounced peak at about 0.6 Hz. As videos from the starting procedure suggest, these oscillations are probably caused by bobbing motions of the rubber-made balloon. They can be avoided using zero pressure balloons. The disadvantage of these devices is the more complicated filling procedure and the higher price. Because of this, attempts were made to find another way of damping these motions. Fishing lines were used on the dereelers connecting the balloon and the payload. Their first deployment was successful but they proved unreliable because of necessary modifications as they are not commercially available for this purpose. Please see Appendix A.2 for a more detailed description. The new payload shape originating from the considerations above can be seen in Figure 3.8.

#### 3.2.3. Interior design

Ideally, all the components of LITOS and the tracking system should be placed inside a single box. Otherwise a double or triple pendulum with potentially chaotic motions is created. Unfortunately, the GPS-Iridium module made by NAL Research Inc. interferes with the CTA measurement. In a test run with the antenna placed below the CTA sensor, electromagnetic interferences occurred at regular intervals. They show an amplitude several orders of magnitude above the wanted signal and therefore would make data evaluation impossible. From the

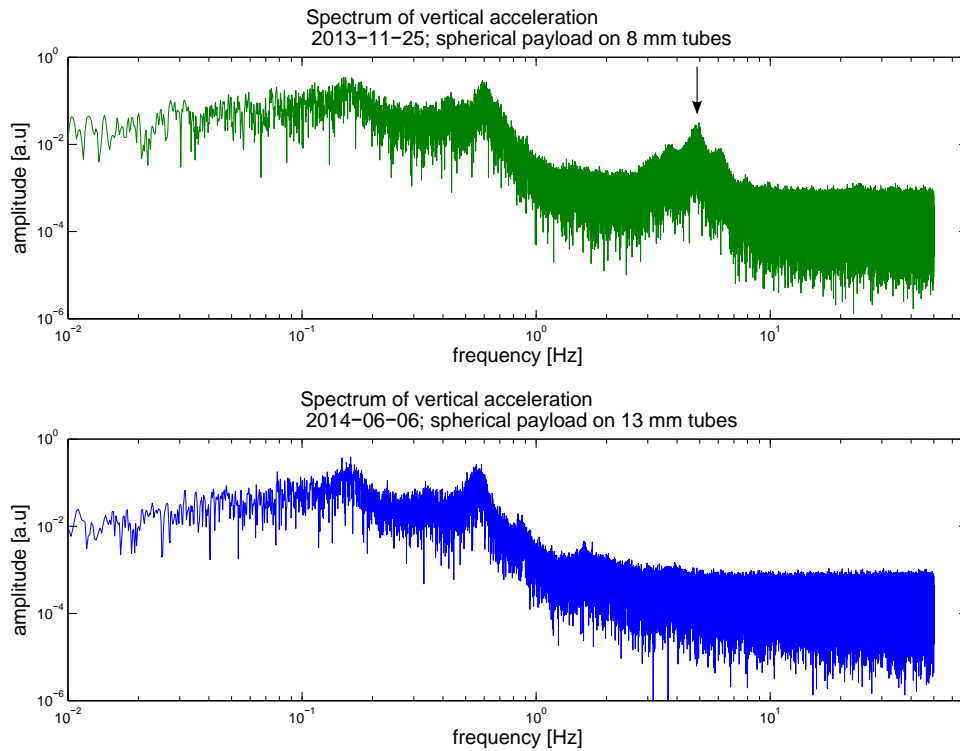


Figure 3.7.: Fourier spectrum of vertical acceleration of the payload for 8 mm and 13 mm tubes. The arrow in the first panel points to the peak caused by oscillating motions of the gondola on the carbon rods.

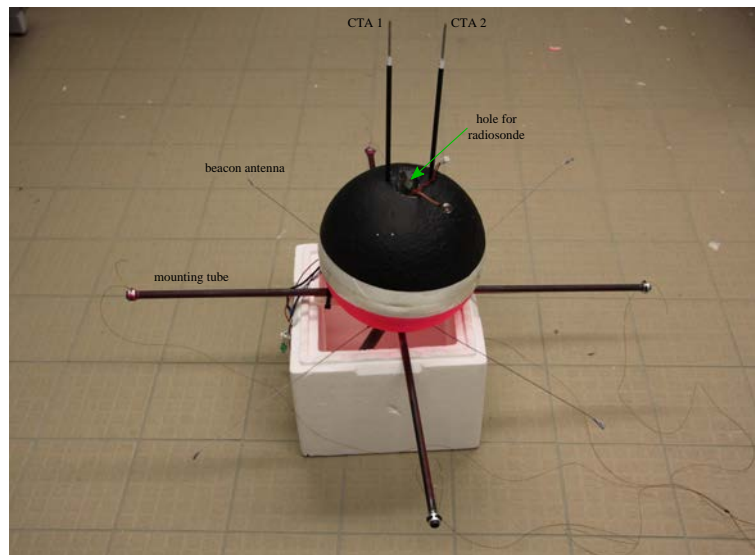


Figure 3.8.: LITOS payload in 2014. The radiosonde placed in the hole on top of the sphere is not mounted.

### 3. Payload development

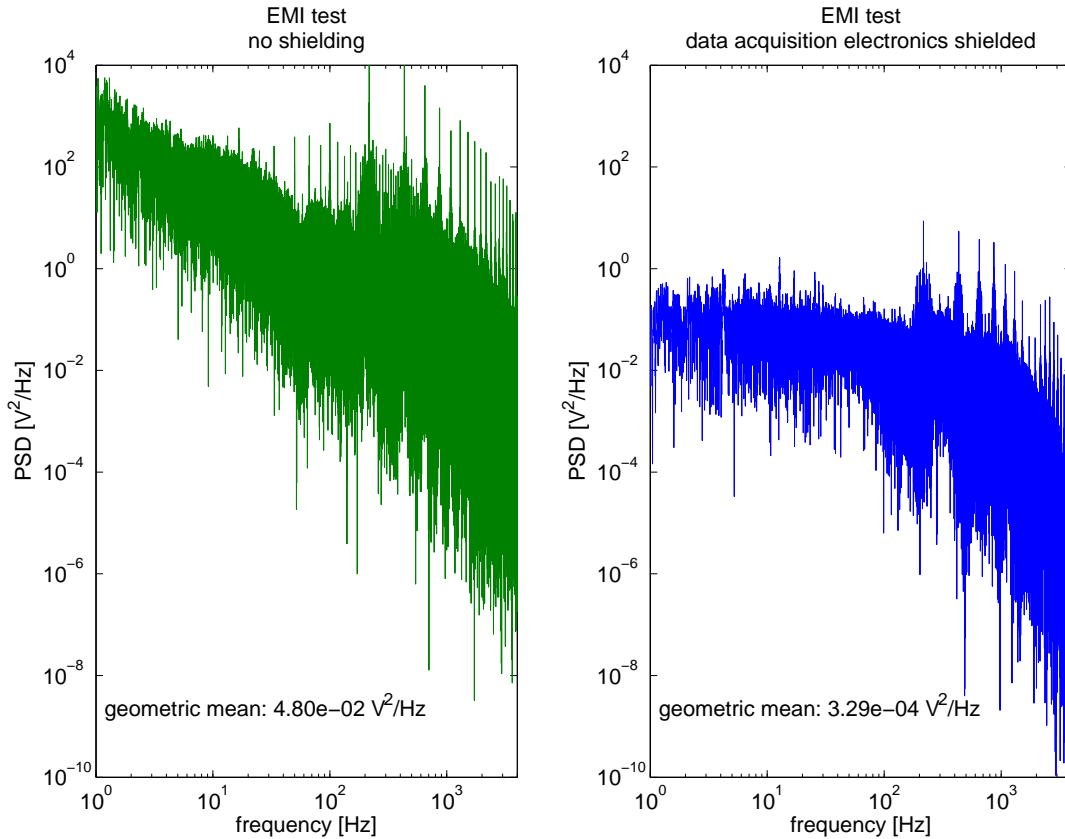


Figure 3.9.: Electromagnetic interferences (EMI) on the CTA signal. The input channel features an anti-aliasing bandpass filter described in Section 3.2.4. A mobile phone is used as a culprit source.

status LED of the tracker it could be seen that these interferences coincide with the Iridium communication of the module. In contrast to the GPS reception the Iridium module needs an active antenna that causes the disturbances. Therefore, the tracking module was placed in a separate box directly beneath the balloon but 150 m above LITOS. During the flight on 16<sup>th</sup> May 2014 the tracker stopped working for no apparent reason during the descent. More than five hours later, it resumed operation which enabled us to recover the payload. From this experience we decided to use a radio beacon as a backup tracking device. It operates at 150 MHz and can be tracked in the range of a few kilometres using a loop antenna.

During the flight on 25<sup>th</sup> November 2013 the data acquisition electronics was placed inside a plastic box. Two radio transmitters (Iridium tracking system at 1620 MHz and radiosonde at 405 MHz) are operated in the flight train of LITOS. They can cause electromagnetic interferences (EMI) on the CTA measurement. This was tested by placing a mobile phone on top of the plastic housing of the data acquisition electronics and starting a call. In a second step this was repeated with the electronics wrapped up in aluminium foil. The results can be seen in Figure 3.9. The mobile phone is sending in the D-band at 900 MHz. It causes elec-

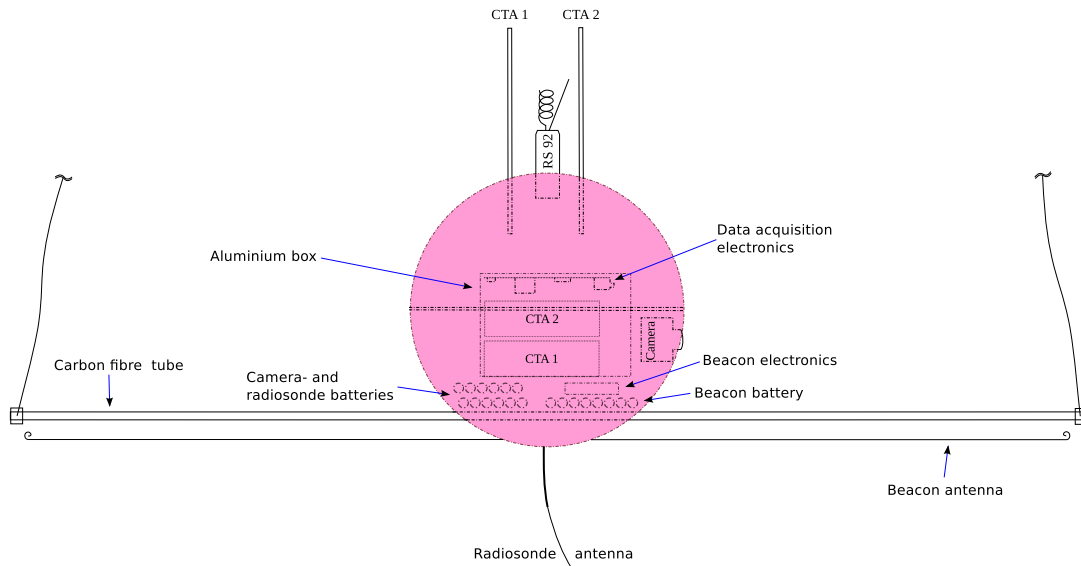


Figure 3.10.: Schematic drawing of the latest LITOS payload design. Batteries within the aluminium box and cables are removed for clarity.

tromagnetic interferences several orders of magnitude above the noise level, that cannot be filtered completely from the wanted signal by the anti-aliasing filter. Shielding of the data acquisition electronics reduces the geometric mean of the power spectral density by more than two orders of magnitude. Further testing was done with the CCA and CTA bridges shielded. This also reduced interferences, but to a smaller extend. From these measurements it was decided to place the data acquisition electronics, the CTA bridges and the power supply batteries inside an aluminium box. A positive side effect is the increased mechanical strength. The main electronics now even survived a hard landing on 27<sup>th</sup> March 2014 which destroyed the polystyrene payload.

Apart from the aluminium box with the electronics, a sideways facing camera, the beacon electronics and 26 AA-sized batteries need to be placed inside the polystyrene sphere. For the setup, please see Figure 3.10.

In the setup from 25<sup>th</sup> November 2013 the radiosonde was placed within the flight train 50 m above LITOS. This causes a time lag between both measurements of ten seconds. To avoid the lag, it was decided to place the radiosonde (RS 92) in LITOS box as it can be seen in Figure 3.10. To make the configuration work, the antenna was extended by a coaxial cable with low damping at the operational frequency of the radiosonde. Though a weakening of the radio signal was expected, the link was still strong enough for proper operation of the device. Nevertheless, evaluating the radiosonde data from both flights with the device mounted on the LITOS gondola revealed some peaks on the temperature measurements, as to be see from Figure 3.11. These spikes have an amplitude increasing with altitude that can reach up to seven Kelvin. When concerned with the quality of the turbulence measurements, it should be kept in mind that  $\epsilon$  depends on the kinematic viscosity  $\nu$  (please see Section 2.1.5 for details).  $\nu$  in turn depends on the radiosonde temperature measurements. These data sets are contam-

### 3. Payload development

inated with radiative effects. Hence it needs be evaluated whether the  $\varepsilon$ -soundings can be trusted at all. In Figure 3.11 temperature predictions taken from the Global Forecast System (GFS) which is run by the US National Weather service (NWS) are shown together with the disturbed measurements. It can be seen that in altitudes up to ten kilometres both measurements coincide apart from small-scale fluctuations, which are not resolved in the GFS data set. In higher altitudes, the spikes in the temperature measurements lie above the predicted values, whereas the main curve of the radiosonde measurement still follows the prediction. For calculations of the energy dissipation rate, the kinematic viscosity is smoothed over 50 data points, which corresponds to a smoothing length of 25 m. In the following, the error in  $\varepsilon$  due to the temperature perturbations will be evaluated. Using the ideal gas law and plugging Equations 2.1.2, 2.1.3 and 2.1.27 into one another yields for the temperature dependence of the energy dissipation rate:

$$\varepsilon(T) = C \frac{T^{3/2}}{(T + 110)^3} \quad (3.2.6)$$

with  $T$  denoting the temperature and the factor  $C$  containing all variables that do not depend on the temperature measurement of the radiosonde. The relative measurement error is given by:

$$\frac{\Delta\varepsilon}{\varepsilon} = \frac{\partial\varepsilon}{\partial T} \frac{\Delta T}{\varepsilon} \quad (3.2.7)$$

with a temperature deviation of 7 K and at a stratospheric temperature of 220 K, differentiation of Equation 3.2.6 results in

$$\frac{\Delta\varepsilon}{\varepsilon} = \frac{3}{2} \frac{-T + 110}{T + 110} \frac{\Delta T}{\sqrt{T}} = 24\% \quad (3.2.8)$$

With energy dissipation rates approximately ranging from  $1e-10$  to 1, a maximum relative error of 24 % is acceptable and expected to be below the errors of the fit routine [private communication, A. Schneider].

Generally, temperature is measured by the radiosonde using a temperature-dependent capacitive sensor wire that is covered with a reflective coating to reduce solar heating [Dirksen et al., 2014]. The authors report a heating of the sensor by radiation of 0.4 K at 100 hPa and a solar irradiance of  $800 (\pm 10) \text{ Wm}^{-2}$  from measurements in a vacuum chamber on the ground. At 100 hPa spikes of about 4 K are seen in the data set. Though our variation is larger by a factor of ten, Holger Vömel from Lindenberg Meteorological Observatory at Deutscher Wetterdienst suggested that our disturbances are caused by solar radiation [private communication]. According to his statement, the solar heating effect will not be averaged out and can reach considerable magnitudes due to the low spin frequency of LITOS compared to an ordinary radiosonde. Accordingly, plans are to use a separate dereeler with the radiosonde to mount it below the LITOS payload in future.

#### 3.2.4. Quality of turbulence measurements

During the first flight with the new payload design on 25<sup>th</sup> November 2013 we utilised a constant temperature anemometer (CTA) manufactured by Dantec Inc. to measure wind fluc-

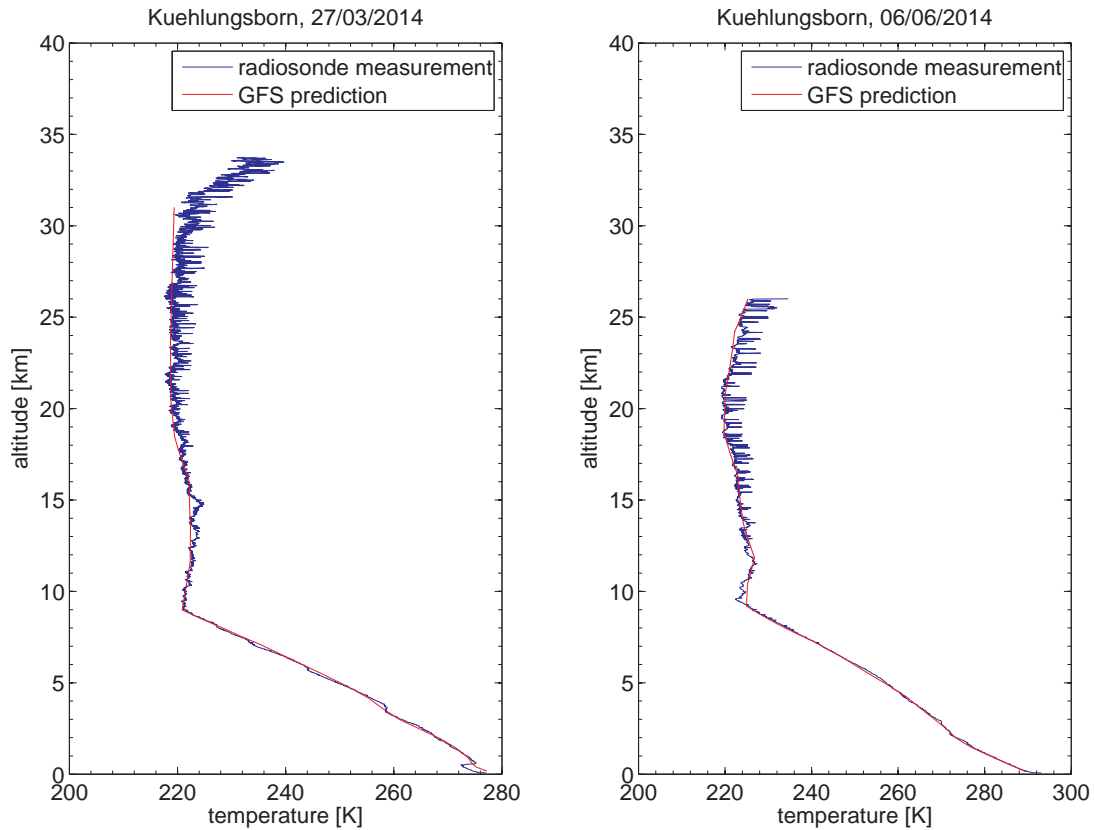


Figure 3.11.: Comparison of measured radiosonde temperatures and GFS predictions for both launches from Kühlungsborn.

tuations and a constant current anemometer (CCA) by TSI Inc. to measure temperature fluctuations. The latter showed a signal to noise ratio that did not allow for any data evaluation (data not shown here).

The analogous signal of the CTA was digitised using a band pass filter with a lower cut-off frequency of 0.3 Hz and an upper cut-off frequency of 2.7 kHz. The intent of the filter was to suppress any parasitic signals from other frequency ranges like the radiosonde or the Iridium system. However, the effects of the anti-aliasing filter need to be removed from the signal during data acquisition. To do so, the filter response was measured over a frequency range six orders of magnitude wide and then convoluted with the measured signal. In conclusion, the filter worked reasonably well. Nevertheless, some problems occurred. In an altitude range between 1 and 15 km oscillations appeared within the signal (Figure 3.12). It can be seen that turbulent areas (light blue) and those contaminated with interferences (red) produce signals in the same order of magnitude. This creates problems if interferences occur in the same altitude regions as turbulence. Both phenomena can only be distinguished from one another by evaluating the related power spectral densities (PSD). They are depicted in Figure 3.13. The first panel shows instrumental noise which is nearly constant from 100 Hz to maximum frequency. Yet there is a slight PSD maximum at about 2 kHz. It is probably caused by the

### 3. Payload development

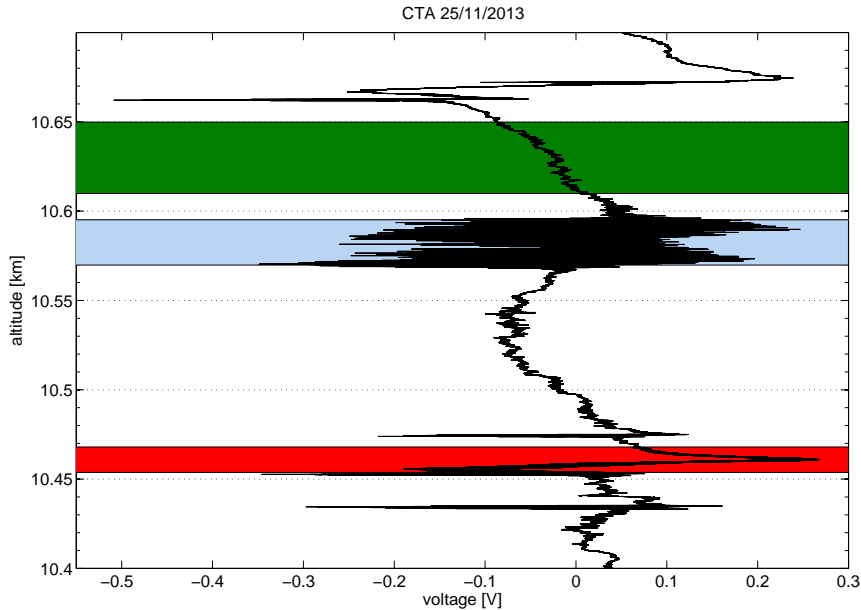


Figure 3.12.: Raw data of the constant temperature anemometer. The green shaded area shows noise only, blue points to real turbulence, whereas red marks an area contaminated with interferences. For the power spectral density of these data, please see Figure 3.13 .

limited precision of the instruments used to measure the filter response and the consequently imperfect removal of the filter effect. The second panel features an undisturbed spectrum of atmospheric turbulence. The third panel however features a typical example of the interferences mentioned above. The first peak shows a centre frequency of about 260 Hz. Up to 3 kHz, higher harmonics of the peak with decreasing amplitude occur. Between 3 and 4 kHz the amplitude increases again and results in a single strong peak. As the frequency of this peak is very close to the cut-off frequency of the digitisation, it may be caused by aliasing effects, although a filter was used. This spectrum does not show any resemblance to the one that is expected from theory. Furthermore, these effects only occur in certain altitude ranges. Therefore it is concluded that these peaks are not of atmospheric but of technical origin. The most likely sources are sound waves produced by howling wind on the cords of the gondola (please see below).

Coming back to the aforementioned oscillations of the signal, one may assume they are caused by oscillations of CTA's feedback control. Due to decreasing air density the heat capacity of the air surrounding the wire is reduced. Accordingly, the closed-loop control circuit may overshoot, so the temperature of the wire and hence the control current may oscillate. To examine this possibility, two CTA systems were placed inside a vacuum chamber and evacuated to the pressure found under flight conditions. The wind was imitated by a processor fan. One of the CTA bridges was the model 54T30, used by us in many flights. The other one was its successor 54T42, kindly made available by Dantec Inc. In the following they are called *CTA old* and *CTA new* respectively. During the test, the vacuum chamber was evacuated using a rotary vane pump. This pump emits considerable acoustic noise. With the pump running, some oscillations have been reproduced. Please see Figure 3.14 for a time

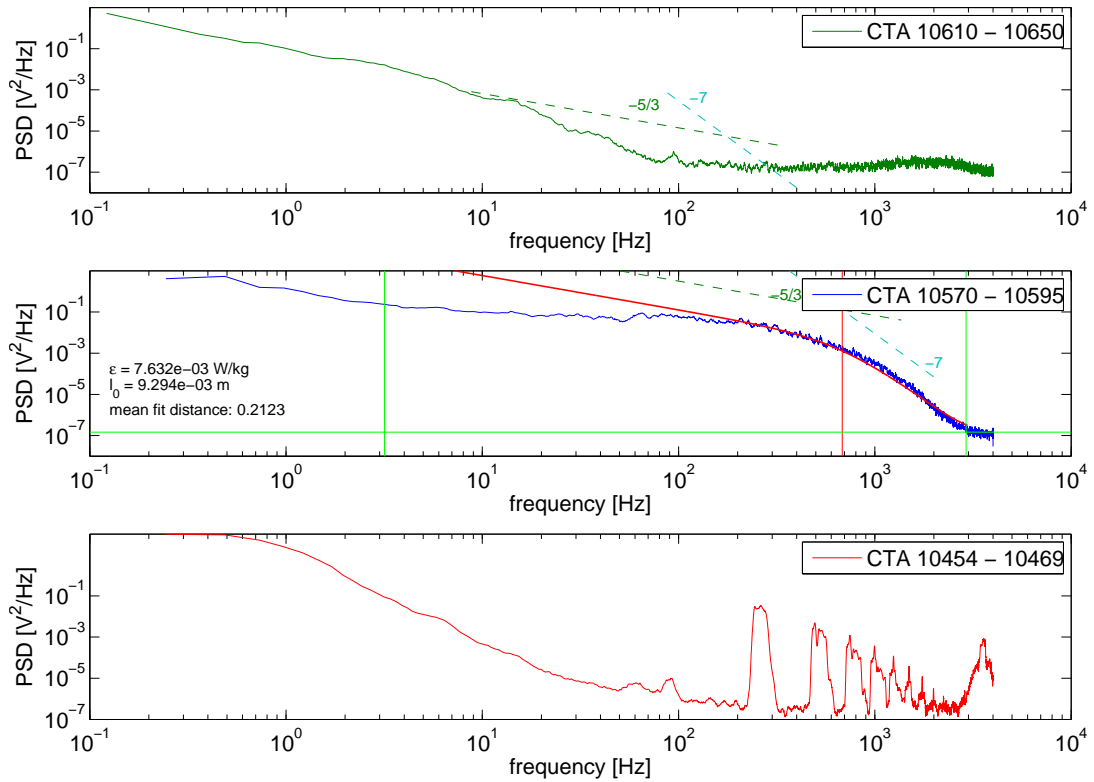


Figure 3.13.: Power spectral densities from raw data shown in Figure 3.12. The allocation of raw data and the corresponding PSD is by colour. The first panel shows a PSD of a non-turbulent patch, containing low frequency atmospheric data and instrumental noise. The second panel shows a successful epsilon fit. The fit area and the noise level are marked in green. In red you see the fitted curve and the calculated inner scale  $l_0$ . The third panel depicts data that contains interferences.

slice of the test. There is a distinct peak at 1500 Hz on both CTAs. Additionally the CTA old shows smaller peaks at 340 and 590 Hz, whereas the new bridge features a strong peak near the cut off frequency at 3500 Hz. Without the pump running, there were no oscillations to be seen. One explanation can be that the running pump induced additional wind motion within the vacuum chamber. On the other side, the oscillations may also have been triggered by acoustic waves emitted by the pump. In the context of evaluation of videos taken on-board LITOS and because the vacuum tests did not reveal a specific pressure range under which the oscillation occur, the latter is the more reasonable explanation. Measurements of the CTA's noise levels (not shown here) disclosed that the new model shows a higher overall noise level and that it is not frequency-independent (i.e., not *white*). Therefore it was decided not to use the newer CTA anymore.

As mentioned above, the oscillations which occur on the atmospheric data are in the audible range and can for example be caused by howling wind noise around the gondola and the ropes. First question is if it is actually possible to measure sound waves with LITOS. To test

### 3. Payload development

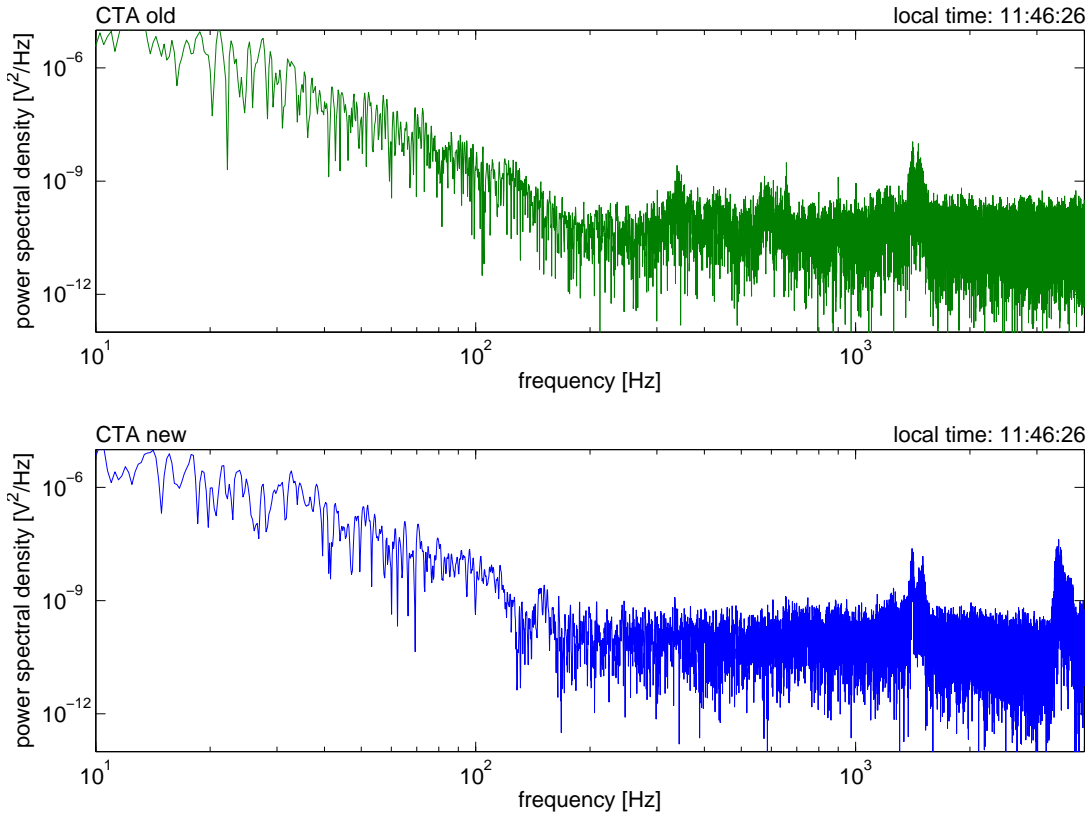


Figure 3.14.: Signals of both CTA placed inside the vacuum chamber at a pressure of 390 hPa, corresponding to the pressure at  $\sim 7.6$  km. The green curve represents the CTA bridge used at IAP as yet (54T30), whereas the blue one depicts data of a new CTA system (54T42). Data acquisition time was three seconds, vacuum pump was on.

this, the CTA wire was placed close to a speaker that emitted a sinusoidal tone. The results can be seen in Figure 3.15. In conclusion it is possible to measure sound waves with the anemometer, but a very high volume is needed to do so. Unfortunately, there was no decibel meter available to quantify this statement. To further evaluate this possibility, the audio track of the sideways facing camera was evaluated and compared to the CTA measurements (Figure 3.16). Comparing both spectra, it is evident that both signals show a first peak at about 200 to 250 Hz. Furthermore, the overtone spectrum looks similar, though the audio signal does show a higher number of peaks compared to the CTA signal. Listening to the videos of the flight one notices a howling sound on the videos which occurs from time to time in the altitude range up to 14 km. This corresponds to the altitude range of the oscillations on the CTA signal. The howling can be noticed during all flights. Its volume is higher than that of people speaking during launch preparation. Probably, the acoustic noise is created by the wind howling in the strings holding the payload. If the sound waves were to be coupled into the CTA measurement via air, the howling of the cords would need to be far louder than people's voices. Hence, it is concluded that the sound is probably coupled in via structure-borne

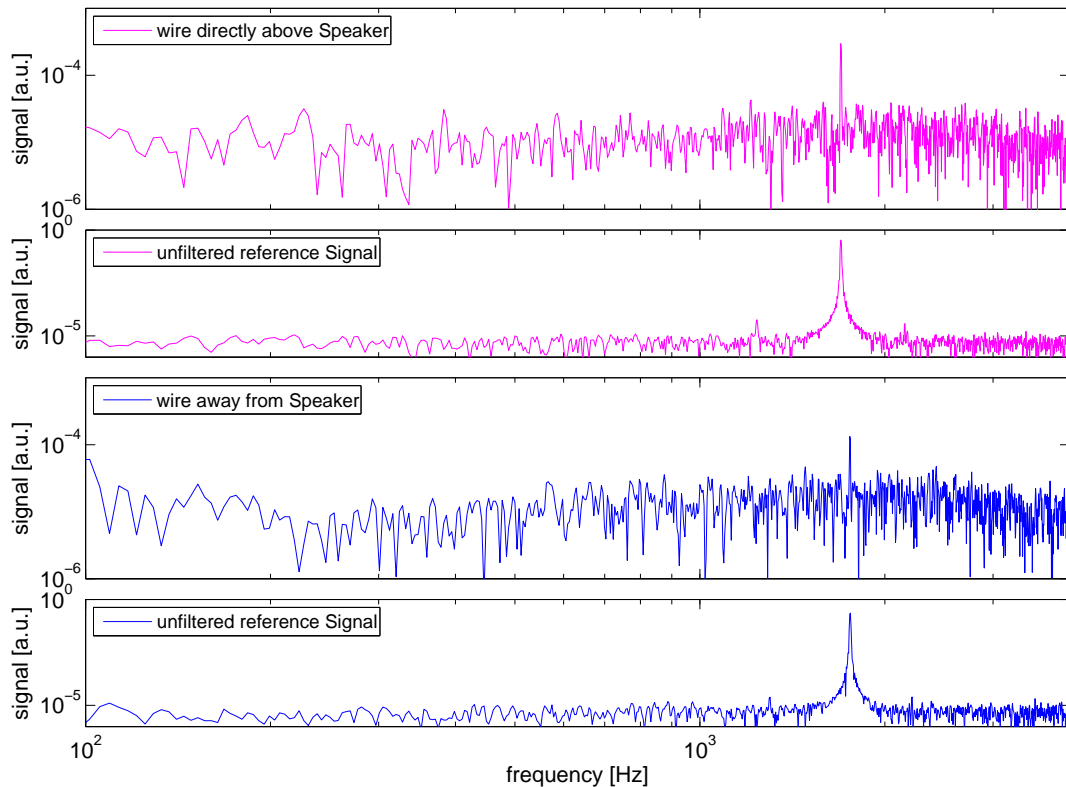


Figure 3.15.: Spectra of sound test with CTA probe placed 10 cm above the speaker that was emitting a sinusoidal tone (uppermost two panels). The first panel shows a FFT of the CTA signal, the second a FFT of the input signal to the amplifier. Lowermost two panels: same as above, save the speaker was placed 50 cm away from the probe and faced perpendicular to the line of sight of the probe.

noise through the carbon tubes. This may also explain the slight difference in the overtone spectra depicted in Figure 3.16.

On both flights in 2014 two CTA systems were used in parallel. There are altitude regions where these oscillations occur on both instruments, some where they occur only on one of them and some where they do not occur at all. A final answer on the different response of the wires on disturbances cannot be given here. But using two CTA systems proved to be a good measure because only a few turbulent patches are affected by oscillations on both CTA systems. When both systems work, the energy dissipation rate of the layer is calculated from the mean value of both Heisenberg fits. The epsilon calculation is rendered impossible only, if both CTAs are affected by the oscillations. Otherwise, the signal of the undisturbed CTA is used. In the future there will be further evaluations on the creation of sound waves by the gondola and their effect on the measurement.

### 3. Payload development

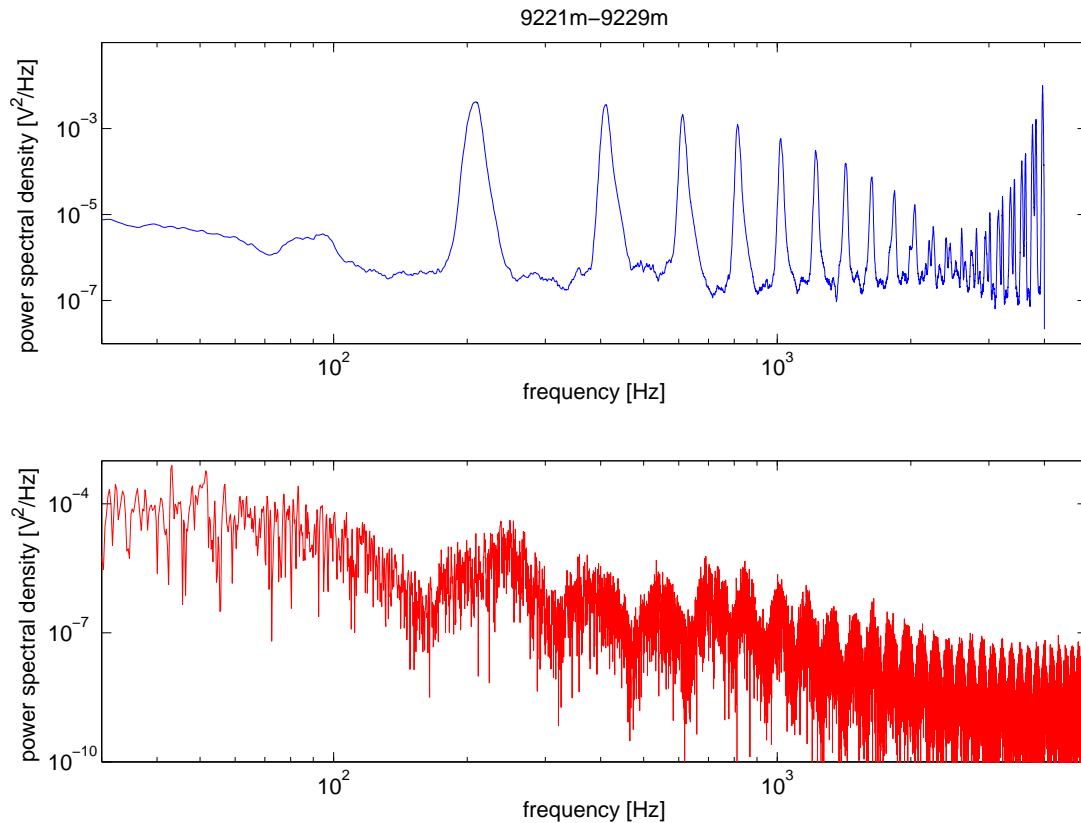


Figure 3.16.: Flight data from 25<sup>th</sup> November 2013. Top panel: PSD of CTA signal showing typical oscillations. Bottom panel: PSD of the audio signal recorded by the sideways facing camera in the same altitude region.

### 3.3. Flight path prediction

A very basic aspect of a successful balloon borne measurement is the recovery of the payload. As landings on sea or in large urban areas are either bad for the payload or potentially dangerous for the inhabitants, a precise prediction of the flight path is highly desirable. The GFS model (Global Forecast System) published by NOAA (National Oceanic and Atmospheric Administration) provides free access to the zonal and the meridional wind each on either 26 or 47 pressure levels depending on the version that is used. Data is released four times a day and provides a prediction up to 192 hours in the future with a temporal resolution of three hours.

Tools exist on the Internet that use these data to calculate the flight path of a balloon. Possibly, the most promising of those is provided by the student run society CUSF (Cambridge University SpaceFlight). This tool gives fairly quick access to a reasonably precise prediction. Nevertheless there are improvements that can be made. The third party software does not provide the source code, therefore, parameters cannot be tuned freely. Also, different programmes for the filling of the balloon, the flight path prediction and the display of geo-

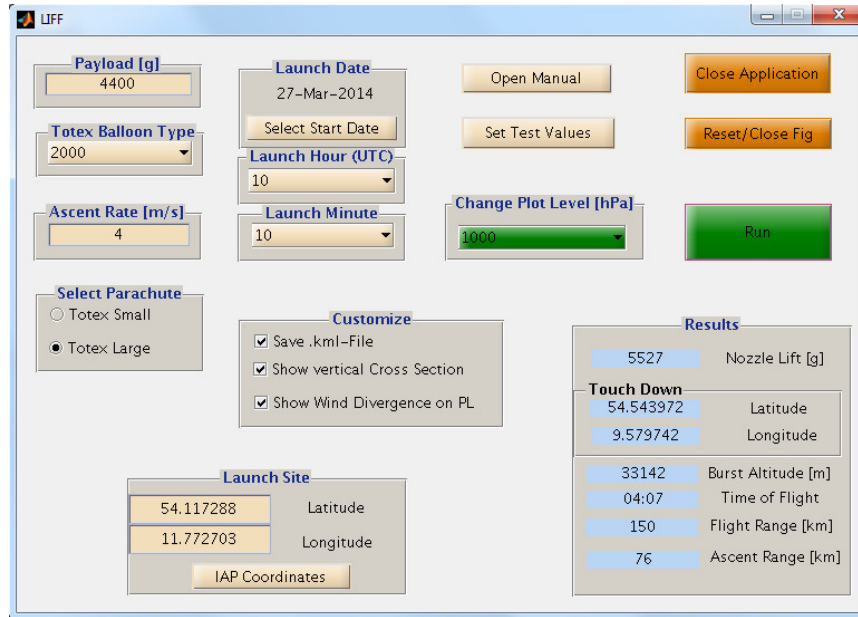


Figure 3.17.: LIFF user interface

physical background parameters are needed that are not adjusted to each other. Thus a tool has been created that combines the aforementioned features and is custom-made to the needs of the balloons and parachutes used at IAP. This tool is named LIFF (Leibniz-Institute Flight path Forecast). It uses the wind field from the high resolution version of the GFS model. To improve precision the wind at a certain point in the atmosphere is calculated by linear interpolation on the latitude-longitude grid as well as between different pressure levels and different forecast times, instead of using the wind on the nearest grid point. Additionally, LIFF provides a graphical user interface (shown in Figure 3.17) that allows for convenient use of the prediction tool. In the lower right corner of the interface predictions of the required nozzle lift, the touch down point and the burst altitude are shown among others. Furthermore, the programme features a graphical output of horizontal divergence in the wind field. Therewith, one can detect instabilities in tropospheric jet streams that provide a source for gravity waves. For the general working scheme of the programme, please see Figure 3.18. The main points of this overview, such as filling of the balloon, calculation of ascent rates, descent rates and the horizontal divergence are explained below in further detail.

### 3.3.1. Balloon filling

In order to improve the accuracy of prediction the ascent rate has to be known as well as possible. All formulae in this section are based on Randall [2014]. LIFF takes the desired ascent rate  $v_{b,d}$  as an input parameter. The real ascend rate  $v_b$  depends on free lift force  $F_{fl}$  or the equivalent mass  $m_{fl}$ . It is calculated by:

$$F_{fl} = m_{fl} g = g \left( \frac{4}{3} \pi r_b^3 (\rho_{gl} - \rho_{gas}) - m_{payload} - m_b \right) \quad (3.3.1)$$

### 3. Payload development

$\rho_{gl}$  denotes air density on ground level. With the following relation for the ascent rate, the balloon radius  $r_b$  on ground level will be acquired using bisection method on  $v_b - v_{b,d} = 0$ .

$$v_b = \sqrt{\frac{F_{fl}}{1/2 c_{d,b} \rho_{gl} \pi r_b}} \quad (3.3.2)$$

This means that  $r_b$  is guessed and this guess is used recalculate the ascent rate  $v_b$ . If it differs from the desired ascent rate  $v_{b,d}$ , the guess for  $r_b$  is changed. Once the correct balloon radius on ground level  $r_b$  is known, the mass equivalent of the nozzle lift in kilogramme  $m_{nl}$  for start preparation can be calculated from

$$m_{nl} = m_{payload} + \frac{F_{fl}}{g} \quad (3.3.3)$$

The drag coefficient of the balloon  $c_{d,b}$  is given for each balloon size by the manufacturer as well as the burst radius  $r_{burst}$ . These data are stored in the programme, so the user just needs to choose the type of balloon. The burst altitude  $z_{burst}$  is computed by:

$$z_{burst} = -H \left( \ln \left( \frac{r_b}{r_{burst}} \right)^3 \right) \quad (3.3.4)$$

$H=7238$  m denotes the pressure scale height.

#### 3.3.2. Balloon ascent

As experience shows, rubber-made meteorological balloons do not reveal a constant ascent rate from ground level to burst altitude. At a certain altitude the ascent rate drops. A possible explanation is a temperature dependence of the elastic modulus of rubber or different regimes of shear stress. In Figure 3.19 it can be seen that on 25<sup>th</sup> February 2011 the drop in ascent rate was slightly above the tropopause. The occurrence of such a drop does not generally depend on temperature. For example on 11<sup>th</sup> November 2008 it happened at 200 m, whereas on 12<sup>th</sup> December 2007 it did not happen at all, though these two launches were performed in the same season.

If two different regimes of shear stress are assumed to exist in the material, the altitude of the knee and the change of ascent rate at the knee should depend on the ratio of balloon weight to payload and the ascent rate on ground level only. This is, because for a certain ratio the ascent rate defines the stress on the balloon envelope. For the same balloon weight (i.e., balloon size) higher ascent rate or higher payload results in an increased start diameter and therefore higher strain on the material. Inspired by these hand waving arguments it was tried to find an empirical formula to describe the altitude of the knee  $z_{knee}$  in the curves as well as the change in ascent rate. For the calculation of burst altitude  $z_{burst}$ , please see Equation 3.3.4. Here it is given directly for clarity. The following formulae made a good match for the flights

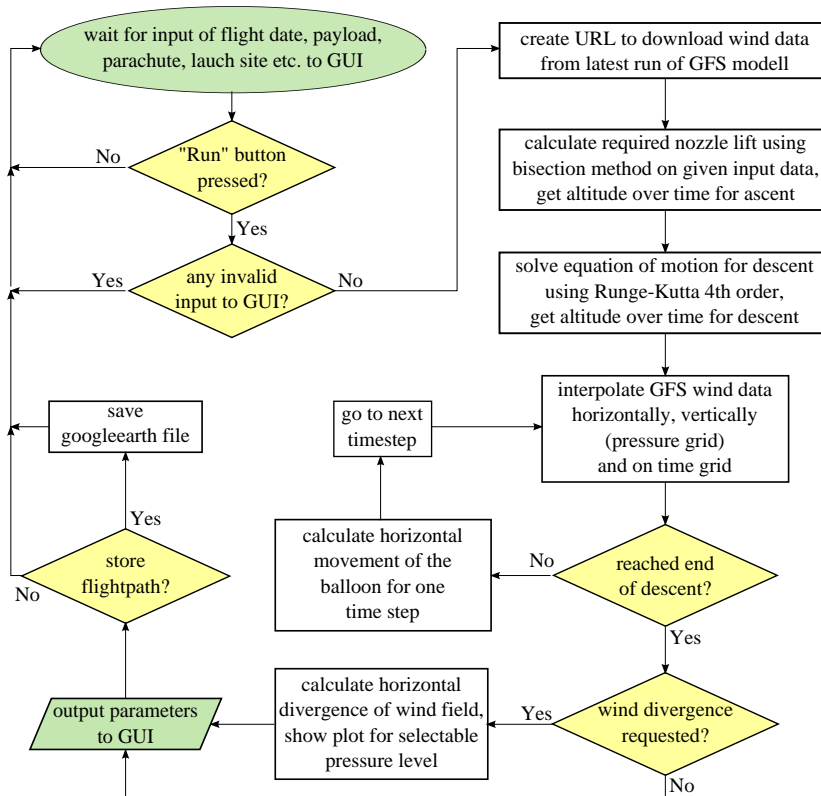


Figure 3.18.: LIFF programme flow

until November 2013 (cf. Figure 3.19).

$$v_{bII} = v_{bI} - 5200 \frac{\left(\frac{m_b}{m_{\text{payload}}}\right)^{1.28}}{v_{bI}} \quad (3.3.5)$$

$$z_{\text{knee}} = z_{\text{burst}} \frac{50}{\exp\left(\frac{m_{\text{payload}}}{m_b}\right)^{1.9}} \quad (3.3.6)$$

Figure 3.19 shows the ascents of all flights performed by IAP with a payload heavier than 2 kg. The first four flights were used to fit Equation 3.3.6 and are indicated by dashed-dotted lines. This equation was used to predict the flightpath of the latest two launches. As shown by the dashed lines, the formula did not provide significantly better results than assuming the ascent rate to be constant. Especially the red curve hardly shows any knee at all. For the evaluation of a constant ascent rate, please see Figure 3.23. Unfortunately, the manufacturer of the balloons (Totex Inc. Japan) has not investigated this effect himself and could not provide any further information on the physical properties of the material used. Another possible explanation for the knees in the curves would be a sudden change in wind speed. As can be seen from the right subplot, the wind was mainly constant on 25<sup>th</sup> February 2011 in the altitude

### *3. Payload development*

range from ten to fifteen kilometres, where the knee occurs. Therefore this explanation can be ruled out. Also the atmospheric temperature does not provide a sufficient explanation. For some flights, the knee occurs around the height of the tropopause at approximately 210 K, whereas others show a knee at much higher temperatures (e.g. 27<sup>th</sup> November) or no knee at all. Other possible explanations are a different age of the latex made balloons, or a different temperature of the filling gas relative to atmospheric temperature. In comprehension, assuming a linear ascent provides better results than the aforementioned fit as comparison of Figure 3.19 and 3.22 reveals. Therefore it was decided to set the ascent rate constant in LIFF. In the future plans are to use zero pressure balloons made of polyethylene with LITOS. As a side effect, they will allow for a more precise prediction of the ascent rates. Campaigns carried out by A. Schneider and A. Haack have shown that these balloons do not reveal any sudden changes in ascent rate. Their vertical velocity only slightly increases with altitude, because their volume increases linearly with decreasing pressure whereas the drag corresponds to the cross sectional area. This effect can be modelled rather easily.

### 3.3. Flight path prediction

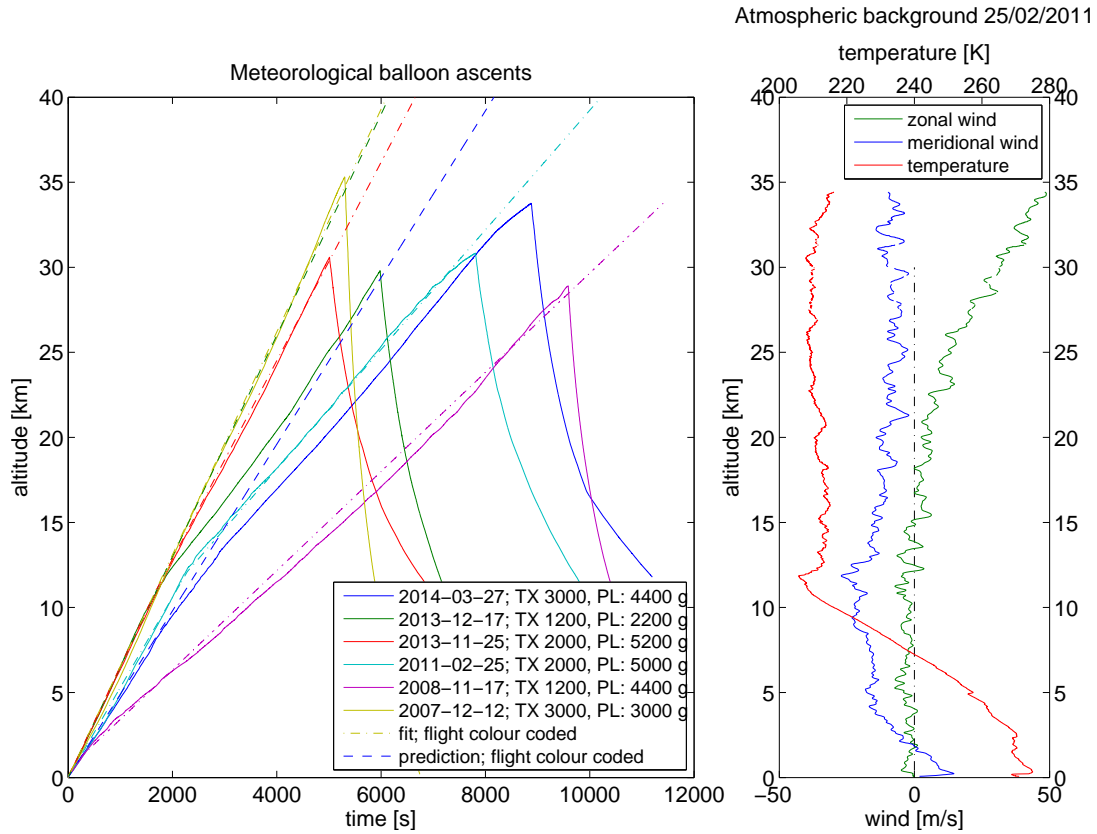


Figure 3.19.: Left: Altitude over time for different flights with payloads heavier than 2000 g.  $TX$  <XXXX> refers to the weight of the Totex balloon in grammes,  $PL$  stands for *payload*. Dashed-dotted lines mark predictions of launches that were used to derive the fit formula. Dashed lines refer to predictions done with that formula. Right: atmospheric background data for the cyan coded flight from the left panel.

#### 3.3.3. Balloon descent

For the descent, the vertical acceleration of the gondola  $\ddot{z}$  is balanced by the gravitational force  $F_g$  and the aggregated drag forces of gondola and parachute  $F_d$ .

$$\ddot{z} = \frac{F_d - F_g}{m_{\text{payload}}} \quad (3.3.7)$$

$m_{\text{payload}}$  denotes the weight of the payload including the parachute. The drag force for any turbulent flow is given by:

$$F_D = \frac{1}{2} \rho v_b^2 C_D A \quad (3.3.8)$$

### 3. Payload development

$v_b$  denotes the vertical speed of the payload. In this case the drag coefficient  $C_D$  is given by the sum of the drag coefficients of the box and the parachute

$$C_D = c_{d,\text{box}} + c_{d,\text{parachute}} \quad (3.3.9)$$

The air-density  $\rho$  can be expressed using column approximation:

$$\rho = \rho_{\text{gl}} \exp\left(-\frac{Mgz}{RT}\right) \quad (3.3.10)$$

$\rho_{\text{gl}}$  denotes the air-density on ground level,  $M$  the molar mass of air,  $R$  the universal gas constant, and  $T$  the atmospheric temperature, which in this case is taken from Fleming et al. [1988]. Combining and rearranging the equations above yields the equation of motion.

$$0 = \ddot{z} + g - \frac{\dot{z}}{2m_{\text{payload}}} \rho_{\text{gl}} \exp\left(-\frac{Mgz}{RT}\right) (c_{d,\text{parachute}} A_{\text{parachute}} + c_{d,\text{box}} A_{\text{box}}) \quad (3.3.11)$$

This equation has been solved using Runge-Kutta 4<sup>th</sup> order method. The drag coefficient for the spherical gondola was set to  $c_{d,\text{box}} = 0.25$  according to Hucho [2011]. In literature drag coefficients for parachutes vary around 1.4 (see Schäfer [2002] for one example). The manufacturer does not provide the drag coefficients of the models used at IAP. Therefore  $c_{d,\text{parachute}}$  was utilised as a free parameter to tune the downcast of the flight path prediction to reality. To do this, the drag coefficient was changed until the predicted landing point for the 25<sup>th</sup> December 2014 came closest to reality. This resulted in  $c_{d,\text{parachute}} = 1.5$ . For evaluation of this method, please see Subsection 3.3.5.

#### 3.3.4. Wind divergence

The horizontal divergence  $D$  of a wind field  $\vec{v} = \begin{pmatrix} u \\ v \end{pmatrix}$  is given by the scalar product of Nabla operator and the wind field:

$$D = \nabla \cdot \vec{v} = \partial_x u + \partial_y v - \frac{\tan \Phi}{r_e} v \quad (3.3.12)$$

$\Phi$  denotes the latitude and  $r_e$  the Earth radius. This divergence is calculated for the wind field along the flight path and plotted on demand. The derivatives are computed using four-point central difference method. The resulting plot can be seen in Figure 3.20. In the left panel the horizontal divergence is shown. In general the range of  $-4 \text{e-}5/\text{s}$  to  $+3 \text{e-}5/\text{s}$  is rather small. Large horizontal divergence would be about one order of magnitude larger. Therefore, no strong gravity wave activity from frontal evolution was expected for the flight on 27<sup>th</sup> March 2014. Please see Section 4.4 for further detail. The right panel shows the zonal wind along the flight path. According to a widely used concept, gravity waves will be filtered, when their phase speed  $c$  matches the zonal background wind  $u$  [e.g. Brasseur and Solomon, 1986]. Therefore the zonal wind can be used to estimate gravity wave breaking.

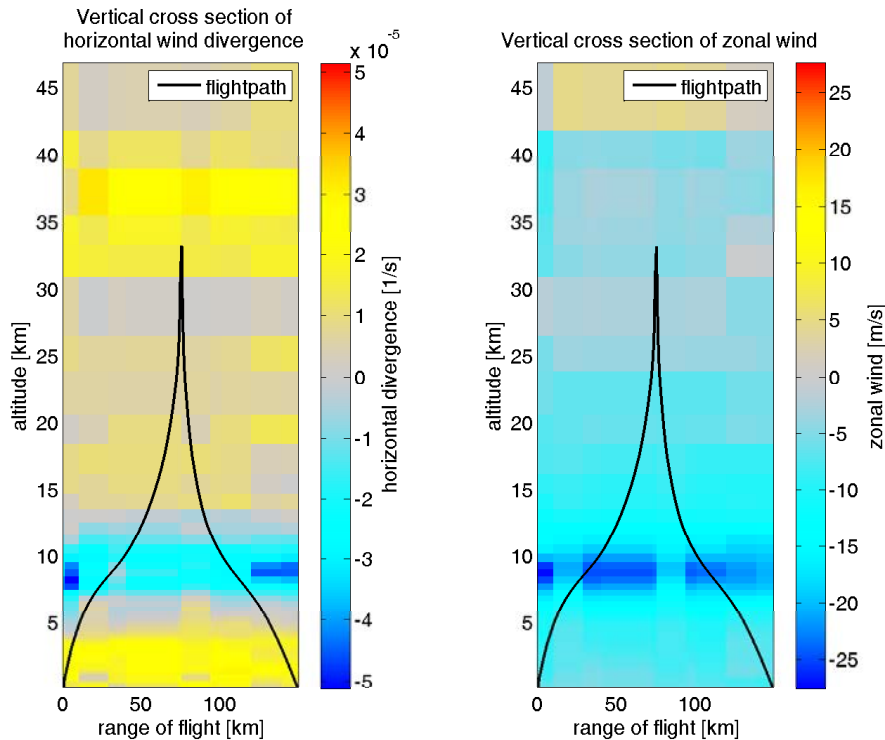


Figure 3.20.: Vertical cross section of the predicted LITOS flight path on 27<sup>th</sup> March 2014. Horizontal wind divergence and zonal wind are colour-coded.

### 3.3.5. Evaluation

So far, three LITOS flights have been predicted using LIFF. Two of them with the large, one with the small parachute. As mentioned above, one flight each is needed to tune the drag coefficients of the parachutes. Hence, the flight on 27<sup>th</sup> March 2014 can be evaluated for the quality of the prediction. The true flight path of LITOS for this day is shown in Figure 3.21 together with two predictions (00:00 and 06:00 run of the GFS model).

The predicted burst altitude was 33 140 m, whereas the balloon reached 33 760 m. This is a deviation of less than 2. The last pre-start run of the prediction anticipated a touch down point that was 22 km away from the real landing point. Using the latest GFS analysis results in a distance from predicted to real landing point of 10 km. Considering the flight range of 158 km, the deviation is 14 % or 7 %, respectively. Clearly, the change from the last pre-start to the latest prediction (not reanalysis) is solely governed by errors in the wind prediction.

Also the latest prediction shows deviations from the real flight track (cf. Figure 3.23). Around a flight time of 1700 s the zonal wind as well as the meridional wind were stronger than in GFS. As visible from Figure 3.22, the 2000 s marker of the prediction is further away from the starting point than that of the true flight path. However this changes later. Between 2100 and 4500 s after launch the prediction overestimates the true wind speed. Accordingly, the balloon covers less distance in the same period of time than predicted. About 4500 s after

### 3. Payload development



Figure 3.21.: Flight track predictions for 27<sup>th</sup> March 2014. The blue line is the last forecast that was available prior to launch, the red one uses the 06:00 run of GFS-model which could be accessed only after take off, whereas the yellow one shows the true flight path of LITOS.

launch, the flight path turned southward. This holds true for the prediction as well as for the real flight. As it is shown in Figure 3.22, the balloon has covered a larger distance when turning southward than anticipated by the prediction. Further along the flight path between 7000 and 8000 s the wind estimation is higher than the wind measured along the flightpath of LITOS, which makes the balloon go further southward than predicted. Around 10 000 s after launch the zonal wind is underestimated, whereas the meridional wind is overestimated by GFS model which gives the prediction too much of a northern component compared to reality.

In the second subplot of Figure 3.22 it can be seen that the constant ascent rate in the prediction leads to better results than the fits that are shown in the blue dashed line of Figure 3.19. Nevertheless, the altitude between 1000 and 4500 s is underestimated by up to 1500 m, which explains at least some of the wind speed deviations in this period mentioned above. Between 5000 and 8000 s after launch the altitude is modelled rather well with deviations in altitude of less than 600 m. At first glance, the descent does not seem to be modelled well. On the one hand, the burst altitude is underestimated by LIFF. As mentioned above, some variations of burst altitudes are down to normal deviations of balloon material properties. Furthermore, the descent rate is underestimated first and overestimated later. This makes the prediction underestimate the distance covered between 8000 and 11 000 s after launch. The true flight path in this period shows a sharp change in descent rate at around 10 000 s after launch. Most

### 3.3. Flight path prediction

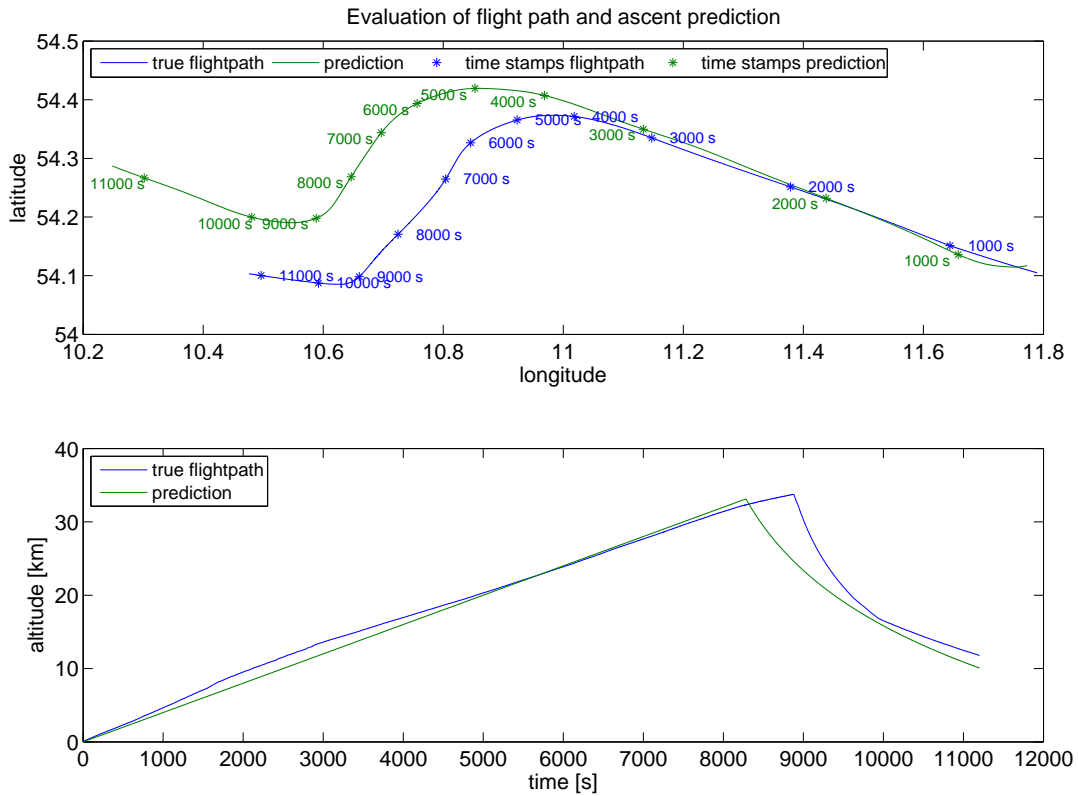


Figure 3.22.: Position and altitude are shown each for the prediction vs. the real flight on 27<sup>th</sup> March 2014. The downcast is only shown until the radiosonde signal was lost.

likely the parachute was not fully deployed until then. Of course, this is something the flight forecast cannot be held accountable for. Practically, the uncertainties in the flight path forecast are mainly down to errors in the wind prediction. In a future version of LIFF this may be improved by using a more precise weather model like the regional Weather Research and Forecasting Model (WARF).

In addition to the improved precision in prediction compared to the on-line tools mentioned above, the user just needs to choose which parachute is used instead of guessing the descent rate on ground level.

### 3. Payload development

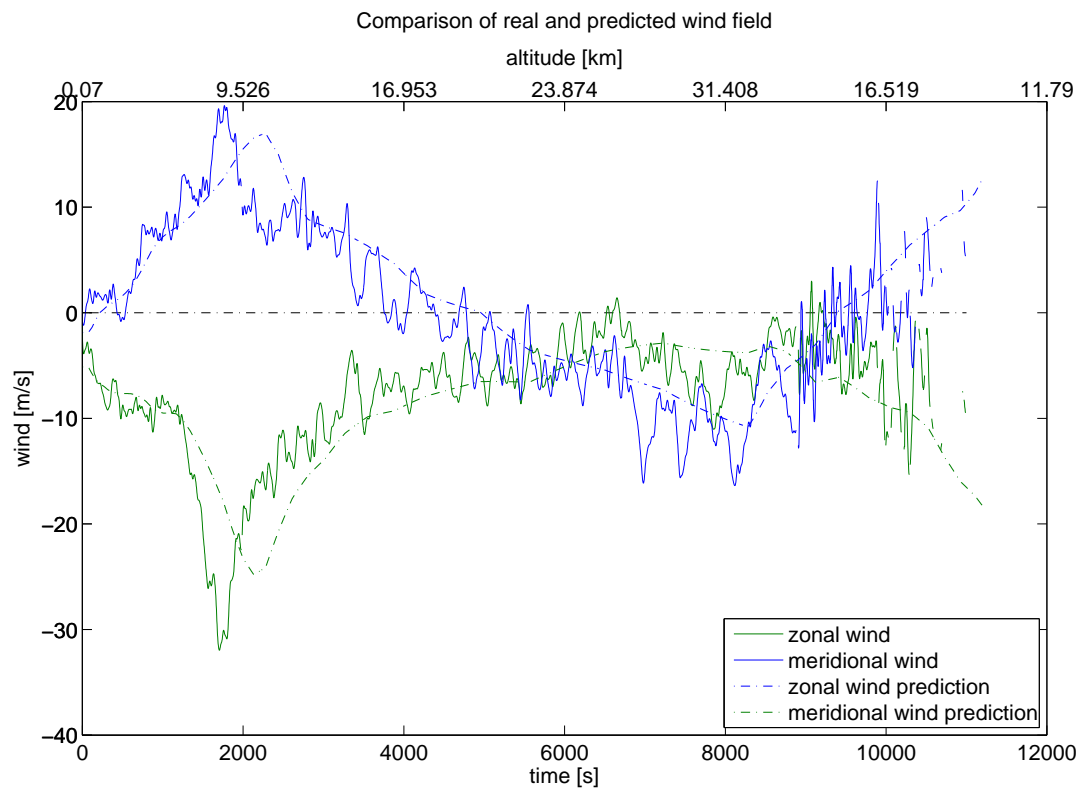


Figure 3.23.: The predicted windfield and the measurements from the radiosonde for the LITOS release on 27<sup>th</sup> March 2014 are shown. The downcast is only shown until the radiosonde signal was lost.

## 4. Geophysical results

In this section, results of two soundings done with the new payload will be discussed and compared to other available measurements of the energy dissipation rate.

Three launches have been carried out with the new LITOS payload so far. The first of them on 25<sup>th</sup> November 2013 had rather poor data quality and will therefore not be reviewed here. The results of the other two from 27<sup>th</sup> March 2014 and 6<sup>th</sup> June 2014 are shown in Figure 4.1 and Figure 4.2, respectively. For comparison, Figure 4.3 shows measurements from the BEXUS 12 campaign on 27<sup>th</sup> September 2011. They were kindly provided by A. Schneider. All figures show energy dissipation rates as measured by LITOS in the left panel. Turbulent altitude bins are marked by a blue dot, whereas non-turbulent ones are left blank. Both launches from Kühlungsborn were equipped with two CTAs as described in Section 2.3.2. Turbulence detection was done on a 5 m altitude grid. The one from Kiruna features a single CTA measurement on a 2 m grid. In the right panels of the three figures temperatures and winds as measured by radiosondes are shown. During both measurements over Kühlungsborn the radiosondes were mounted on the LITOS gondolas which led to peaks on temperature data, please see Section 3.2.3 for further information.

### 4.1. Energy dissipation rates

In Table 4.1, condensed information regarding the turbulence measurements is given. Generally, the statistical allocation of the data sets follows a log-normal distribution [private communication, A. Schneider]. Therefore it was decided to calculate geometric mean values of the energy dissipation rate for the troposphere and for the stratosphere. As especially the launch in June 2014 showed large variations of  $\varepsilon$  in the stratosphere, this area is divided into two regions and mean values are calculated separately. In all cases, the geometric mean is calculated over turbulent altitude layers only, non-turbulent regions are omitted. Practically, the geometric mean is what one visually identifies as the mean from the left panels in Figures 4.1, 4.2 and 4.3. On the other hand, the impact of turbulence on tracer distribution for example largely depends on the strength of turbulence, meaning that even though the energy dissipation rates are allocated log-normally, the effect of turbulence cannot be regarded as proportional to  $\log_{10} \varepsilon$  but rather proportional to  $\varepsilon$ . Accordingly, Table 4.1 shows arithmetic mean values as well. In contrast to the geometric mean it is calculated over all altitude layers, including those where  $\varepsilon = 0$ . This was done to allow for better comparison with other measurements of the energy dissipation rate. The *percentage of single sensor usage* indicates that more than half of the turbulent patches in the data set from March 2014 were found using only one of the two CTAs on board. On 6<sup>th</sup> June 2014 this number increased to almost nine out of ten. By excluding all measurements acquired by single sensor usage from the data,

#### 4. Geophysical results

Table 4.1.: Collective results of both launches from Kühlungsborn and of BEXUS 12. *Percentage of turbulent patches* indicates how many percent of the altitude bins have been recognised as turbulent by the data processing scheme. *Percentage of single sensor calculation* shows how many percent of all turbulent patches were acquired by using only one of the two sensors. *Percentage of compliance* points out how many percent of the measurements with both sensors available were not rejected (cf. Section 2.3.2). The geometric mean was calculated considering turbulent patches only, whereas the arithmetic mean includes all altitude bins.

		Kborn 27/03/14	Kborn 06/06/14	Kiruna 27/09/11
troposphere	percentage of turbulent patches	49	41	80
	geometric mean $\varepsilon$ [W/kg]	2.1e-7	9.0e-5	4.1e-5
	arithmetic mean $\varepsilon$ [W/kg]	2.0e-4	6.2e-3	4.7e-4
stratosphere	percentage of turbulent patches	38	25	50
	geometric mean $\varepsilon$ [W/kg]	4.3e-6	3.0e-6	7.7e-5
	arithmetic mean $\varepsilon$ [W/kg]	6.6e-4	7.0e-3	1.7e-3
lower stratosph. alt < 15 km	percentage of turbulent patches	53	43	65
	geometric mean $\varepsilon$ [W/kg]	2.3e-7	6.0e-6	3.0e-5
	arithmetic mean $\varepsilon$ [W/kg]	1.1e-4	2.1e-2	6.1e-4
middle stratosph. alt > 15 km	percentage of turbulent patches	34	17	44
	geometric mean $\varepsilon$ [W/kg]	1.8e-5	1.2e-6	1.3e-4
	arithmetic mean $\varepsilon$ [W/kg]	8.3e-4	9.8e-5	2.1e-3
percentage of single sensor use		57	88	n.a.
percentage of compliance		60	47	n.a.

it was noticed that especially data with low  $\varepsilon$ -values are affected by the loss of one sensor. Non-turbulent altitude bins are found by the data processing routine through the fit distance criterion. The high occurrence of single sensor measurements at low energy dissipation rates indicates that this criterion needs to be reconsidered in the future. The *Percentage of compliance* points out that in almost half of all turbulent altitude regions where both CTA produced a valid  $\varepsilon$ -measurement their values failed to be less than a decade apart and were rejected. This emphasises the importance of using two independent CTAs because still a considerable number of the measurements is disturbed by non-atmospheric phenomena.

In Figures 4.1 and 4.2, a theoretical lower limit for  $\varepsilon$  is shown. It is calculated according to Lübken [1993]. He states that  $\varepsilon$  cannot be significantly lower than the molecular diffusion coefficient, because otherwise dissipation would consume turbulent eddies immediately. This consideration yields

$$\varepsilon_{\min} \approx \nu N^2 \quad (4.1.1)$$

with  $\nu$  denoting the kinematic viscosity and  $N^2$  the Brunt-Väisälä frequency. As visible from Figures 4.1 and 4.2, in quite a few altitude bins  $\varepsilon$ -values smaller than this estimation were detected. In exact numbers it were 17% on 27<sup>th</sup> March 2014 and 12% on 6<sup>th</sup> June 2014. From manually reviewing turbulent spectra it is known that for low  $\varepsilon$ -values the fit becomes unreliable due to a low number of evaluated data points. These values are marked by a grey

#### 4.1. Energy dissipation rates

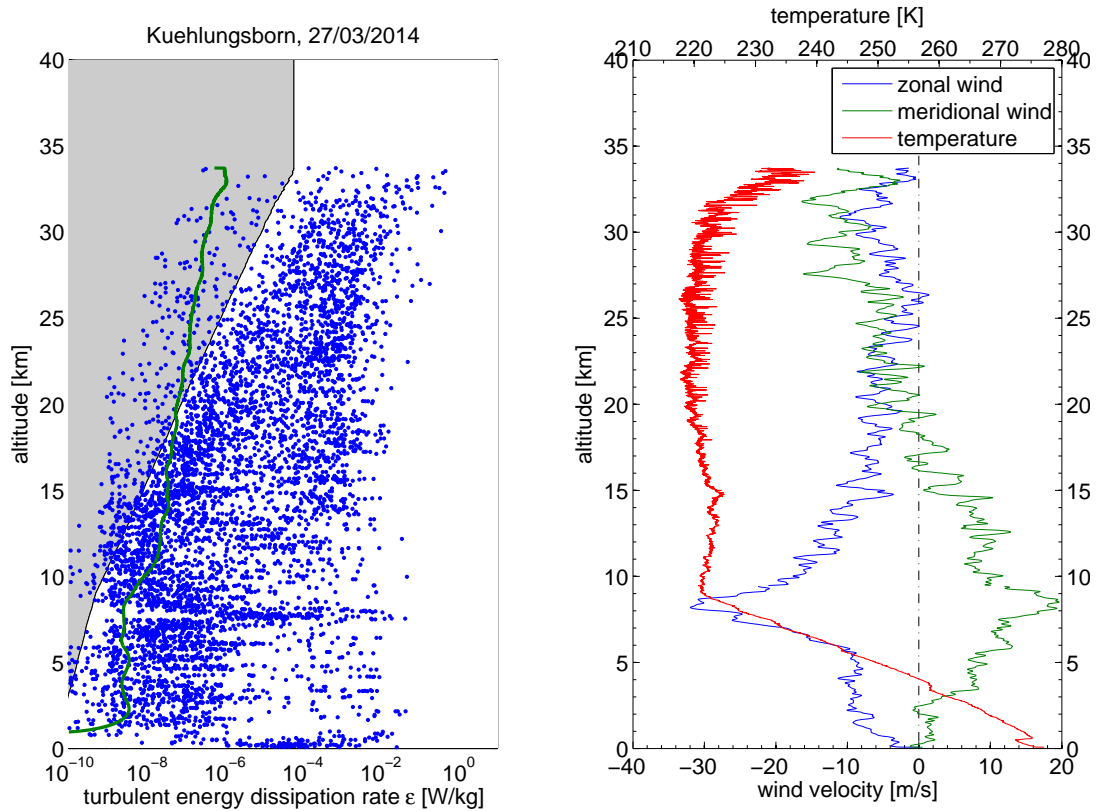


Figure 4.1.: Left panel: turbulent energy dissipation rates as measured with the new LITOS payload on 27<sup>th</sup> March 2014. Data was acquired evaluating two CTAs on a 5 m altitude grid as described in Section 2.3.2. Each point represents a turbulent altitude bin, the green line shows the theoretical minimum for  $\epsilon$ , calculated according to Lübken [1993]. Wind and temperature measurements from the on-board radiosonde are given on the right-hand side. The spikes on the temperature data are due to radiative effects, please see Section 3.2.3 for further details. As discussed in the next section, measurements unreliable for technical reasons are marked by grey background colouring.

background and the procedure is explained further in the following section. Please note that these very small  $\epsilon$ -values have a much larger impact on the geometric mean than on the arithmetic one.

When comparing the values for the energy dissipation rate given in Table 4.1 one finds that the arithmetic mean values of the energy dissipation rates for the first launch from Kuehlungsborn and for that one from Kiruna do not differ by more than a decade for the troposphere as well as for the stratosphere. In contrast, on 6<sup>th</sup> June 2014 the arithmetic mean is a bit more than one order of magnitude higher in the troposphere and almost one decade higher in the stratosphere compared to the other two flights. The geometric mean on the other hand is close for 6<sup>th</sup> June 2014 and 27<sup>th</sup> September 2011 in the troposphere with much lower values on 27<sup>th</sup> March 2014. In the stratosphere the geometric means of both launches from

#### 4. Geophysical results

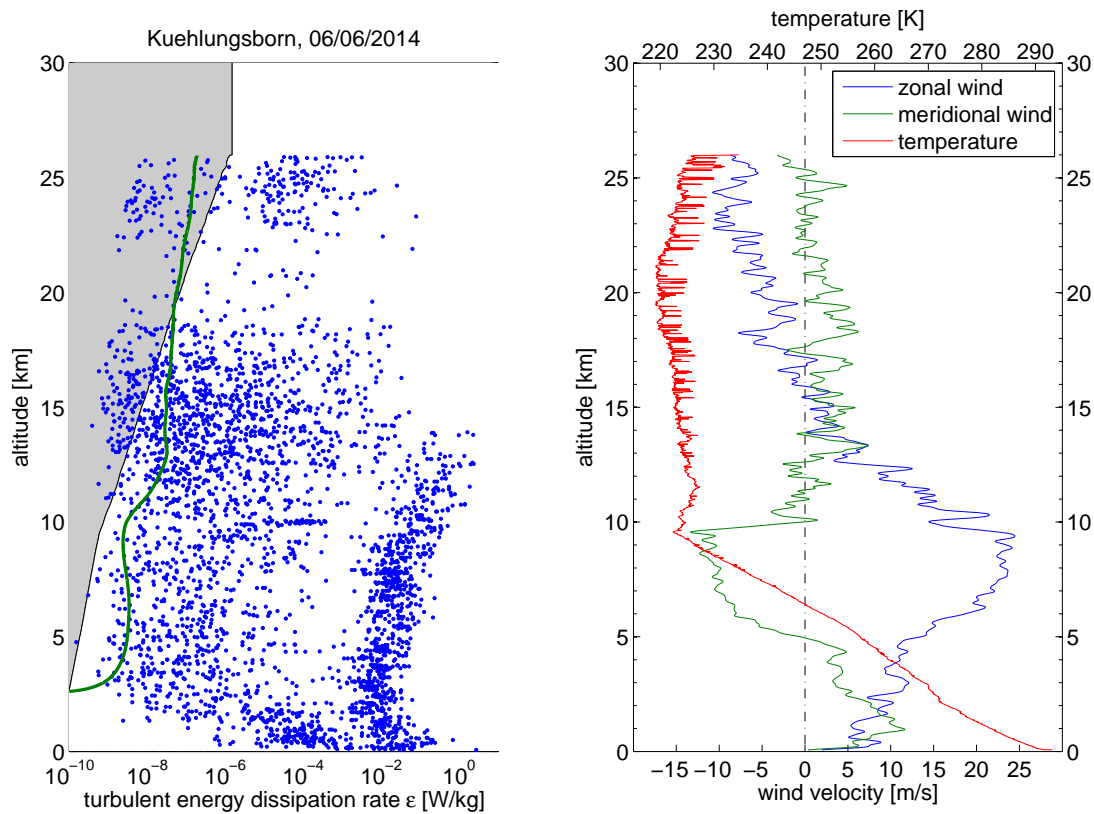


Figure 4.2.: Same as Figure 4.1 but for LITOS launch on 6<sup>th</sup> June 2014.

Kühlungsborn resemble each other, whereas the one from Kiruna shows a higher value. By differentiating the stratosphere into two parts it is found that the first launch from Kühlungsborn as well as the one from Kiruna show an increase of geometric as well as arithmetic mean values with altitude. In contrast on 6<sup>th</sup> June 2014 the arithmetic mean of  $\epsilon$  in the lower stratosphere is two orders of magnitude lower than in the middle stratosphere. When looking at the logarithmically scaled plots, one finds that on 27<sup>th</sup> March 2014 there was a lot of weak turbulence in the troposphere and rather strong turbulence in the stratosphere, whereas the 6<sup>th</sup> June 2014 generally showed less turbulent areas, but rather high  $\epsilon$  in the troposphere and especially in the lower stratosphere. This corresponds to the different mean values discussed above. Furthermore, in the troposphere data can be divided into a branch of high  $\epsilon$ , being centred around 0.1 W/kg, and a lower branch around  $1e-7$  W/kg. The Kiruna launch shows increasing dissipation rates in the troposphere as well as in the stratosphere, with a sharp drop at the tropopause. Summarising, it can be said that turbulence activity was about the same on 27<sup>th</sup> March 2014 over northern Germany and on 27<sup>th</sup> September 2011 over northern Sweden, whereas it was significantly higher on 6<sup>th</sup> June 2014 over northern Germany.

## 4.2. Influence of the data evaluation scheme

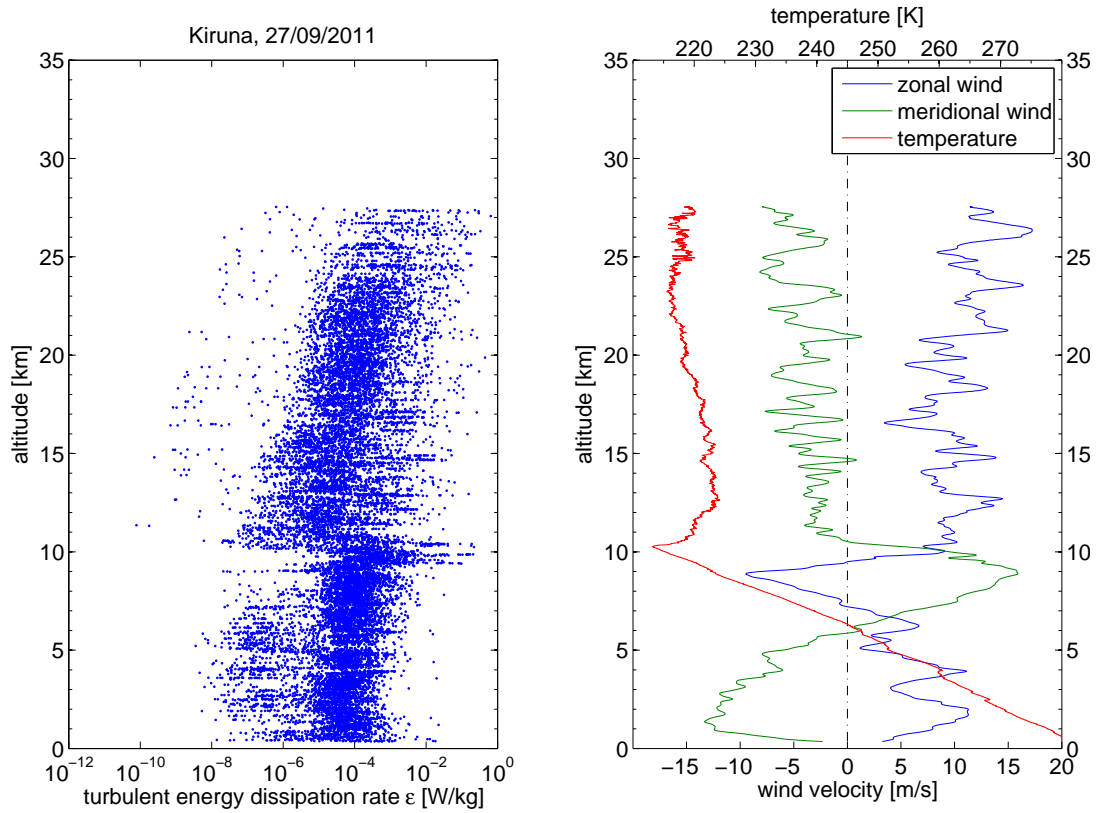


Figure 4.3.: Same as Figure 4.1 but for LITOS launch on 27<sup>th</sup> September 2011. A single CTA was used on a 2 m altitude grid. Data was kindly provided by A. Schneider.

## 4.2. Influence of the data evaluation scheme

As discussed in Section 2.3.2, altitude bins were considered turbulent whenever one of the sensors showed turbulence. From Table 4.1 it is visible that the majority of all calculations are done on the basis of one sensor only. Therefore the effect of the above mentioned decision shall be evaluated here. The corresponding mean values for both types of evaluation are given in the table below. *SiSe* stands for *single sensor measurement*, *DoSe* for *double sensor measurement*.

		Kborn 27/03/2014		Kborn 06/06/2014	
		SiSe	DoSe	SiSe	DoSe
troposphere	geometric mean $\epsilon$ [W/kg]	2.1e-7	3.2e-7	9.0e-5	4.1e-3
	arithmetic mean $\epsilon$ [W/kg]	2.0e-4	3.3e-5	6.2e-3	1.7e-3
stratosphere	geometric mean $\epsilon$ [W/kg]	4.3e-6	6.5e-6	3.0e-6	3.4e-3
	arithmetic mean $\epsilon$ [W/kg]	6.6e-4	1.2e-4	7.0e-3	2.4e-3

#### 4. Geophysical results

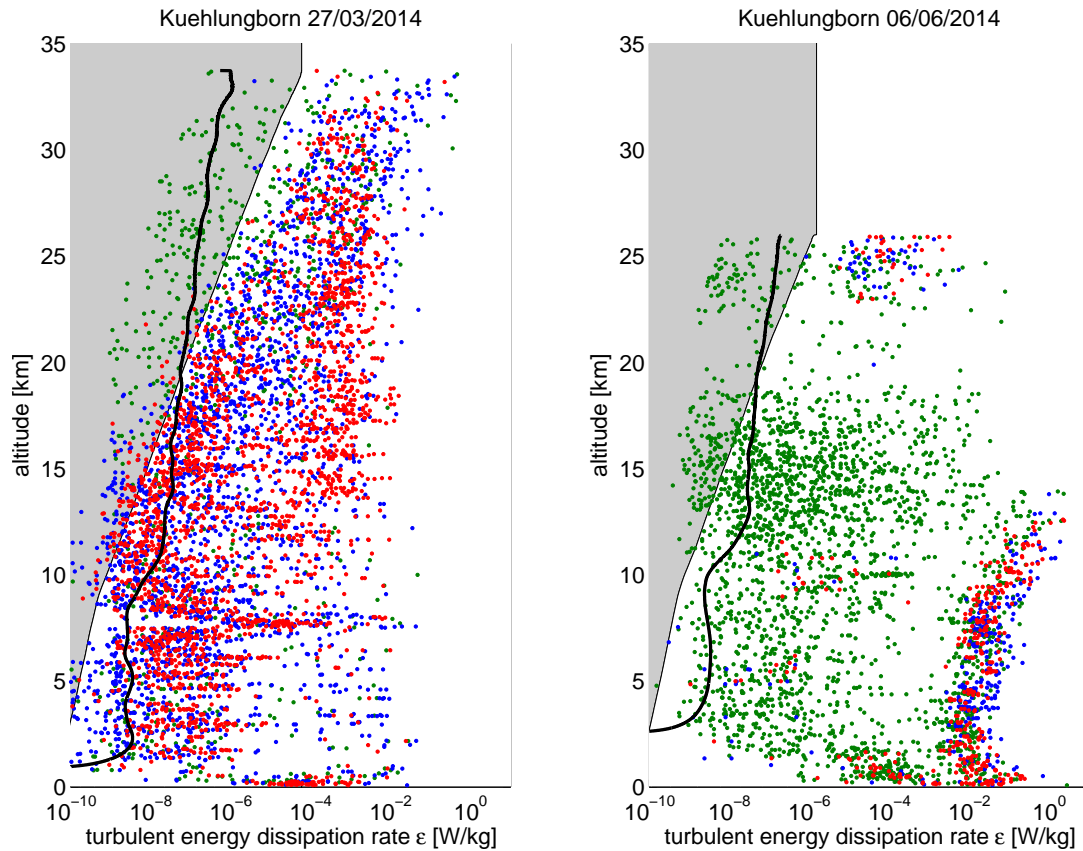


Figure 4.4.: Correlation of  $\epsilon$ -values and sensors. Red: measured by both sensors, green: measured by sensor I only, blue: measured by sensor II only. The theoretical minimum for  $\epsilon$  is given by the black line. Areas marked in grey show questionable results, please see text for further information.

It can be seen that the arithmetic mean values of energy dissipation rates for both evaluation types do not differ by more than a factor of ten, except for the troposphere on 27<sup>th</sup> March 2014. The geometric mean on the other hand does show large differences between both methods. Therefore great care must be taken when interpreting this value. Figure 4.4 depicts which of the  $\epsilon$ -evaluations were done using sensor I, sensor II or both of them. Here it is important to know that on 27<sup>th</sup> March 2014 two equal CTA systems were launched, namely mini CTA 54T30. In contrast, on 6<sup>th</sup> June 2014 its successor 54T42 was used as sensor II. During noise level tests it was noticed that this new system shows a higher overall noise level which is also not completely white (i.e., it depends on frequency, data not shown here). This leads to severe problems in detecting weak turbulence, as seen in the right panel of the figure. It also suggests to include measurements acquired by only one of the two sensors in the data processing because otherwise all data with low  $\epsilon$  values would be discarded due to the malfunction of CTA 54T42. From manual review of several Heisenberg fits it was found that the upper limit for a reliable detection of the inner scale  $l_0$  with the current automatic data evaluation system on a 5 m altitude grid is at about 50 cm. This is because the low number

### 4.3. Comparison with other measurements

of data points at large spatial scales makes the fit less reliable. Furthermore, the spectrum shows non-turbulent atmospheric motion at large scales (cf. Figure 3.13 for example). This will perturb the Heisenberg fit at very low energy dissipation rates. Turbulent patches with either one of the above mentioned effects are sorted out by the fit distance criterion of the data retrieval routine (cf. Figure 2.8). This will be improved in the future and an upper limit for the detection of  $l_0$  may be used in the data acquisition routine. Also the choice of the 5 m altitude grid will be reviewed, as a larger grid size increases the number of data points in the Heisenberg fit. The value of 50 cm for the upper limit of  $l_0$  is a first estimate, which will need to be confirmed by further investigations.  $l_0 > 50$  cm corresponds to all energy dissipation rates marked by a grey background in Figure 4.4. They cannot be trusted without further improvement of the data evaluation scheme and are therefore marked in Figures 4.1 and 4.2 also.

As the compliance of the arithmetic mean values of both evaluation methods indicates, the two data sets allow for a geophysical interpretation on larger altitude scales. Before taking advantage of the high resolution  $\varepsilon$ -profile, the differences between the sensors need to be investigated further though.

### 4.3. Comparison with other measurements

To put the results obtained with LITOS into a broader perspective, the energy dissipation rates of both launches from Kühlungsborn are compared to those obtained with the measurements described in Section 2.2. The results are shown in the table below.

			$\varepsilon_{\text{troposphere}}$ [ $10^{-5}$ W/kg]	$\varepsilon_{\text{stratosphere}}$ [ $10^{-5}$ W/kg]
MUTSI	Gavrilov et al. [2005]	M1	110	3.0
		M8	18	4.7
		M9	360	1.7
GOMOS	Gavrilov [2013]		n.a.	0.25
Barat	Barat [1982]		n.a.	2.7
LITOS	own work	03/2014	20	66
		06/2014	620	700

Comparisons with other data sets are given by Theuerkauf [2012]. The MUTSI campaign was carried out over Japan at  $35^\circ$  N. In the table arithmetic mean values of the energy dissipation rates are given. The GOMOS data set was acquired at 30 km altitude between  $34^\circ$  N and  $36^\circ$  N. Barat's values were taken over France in altitudes between 25 and 28 km. The arithmetic mean given here is not a mean value over all altitude layers, but the mean value over the turbulent patches.

In the troposphere, the values obtained by MUTSI are in the same order of magnitude as the ones from LITOS. Stratospheric energy dissipation rates taken from the latter on the other hand are two to three orders of magnitude higher compared to all other values shown.

#### 4. Geophysical results

This is likely to be caused by the higher altitude resolution of LITOS. As visible in Figures 4.1 and 4.2, high energy dissipation rates occur also in very small patches. With other measurement techniques, these structures cannot be fully resolved. Instead, turbulent areas are considered together with non-turbulent ones. The impact of this on the measurements of  $\varepsilon$  is not clear. In other words: further investigations on the influence of sampling small turbulent patches on a coarse altitude grid need to be carried out in order to make LITOS measurements better comparable to others.

#### 4.4. Meteorological background conditions

The occurrence of turbulence is closely linked to gravity wave activity in the troposphere and the stratosphere (cf. Section 4.6). Therefore, parameters for gravity wave activity shall be evaluated in the following. All plots shown in this section rely on the Global Forecast System (GFS) as published by NOAA (National Oceanic and Atmospheric Administration) and on the radiosonde measurements.

The most prominent sources of gravity waves according to Fritts and Alexander [2003] are topography, convection, geostrophic adjustment and wind shear. Hereafter, they will be reviewed one after another. In the end the different potential sources are summarised and related to LITOS observations.

At first, orographic gravity waves shall be discussed, which are caused by topographic impact on the flow. The wind field at 850 hPa (about 1400 m) for the times of all three launches is given in Figure 4.5. Concerned with the data for BEXUS 12, it is important that the main mountains in northern Norway and Sweden are the Scandinavian Mountains close to the Norwegian Sea. When looking at the first panel, it should be noted that the wind on 27<sup>th</sup> September 2011 blew parallel to this mountain chain in northern Norway, but almost perpendicular to it in the middle. Therefore significant mountain wave generation is expected in central Norway on 27<sup>th</sup> September 2011 but hardly any contribution from the northern parts of the country. The second panel of Figure 4.5 shows a wind flow over northern Germany coming from southern Sweden and the Baltic Sea. In this area no considerable mountains are located. Therefore mountain wave generation was not expected in the important area on 27<sup>th</sup> March 2014. On 6<sup>th</sup> June 2014, the main flow in the launch area was northbound. So possible sources for mountain waves are the German Central Uplands. Even though these mountains are only a few hundred meters high there may have been mountain wave generation due to the flow being almost perfectly perpendicular to the mountain chain.

Yet another gravity wave source is convection. According to Fritts and Alexander [2003], deep convective clouds can be linked to high-frequency gravity wave activity in the stratosphere. Nevertheless, according to them these waves are characterised by their diversity in phase speeds and frequencies, which makes it difficult to establish the right correlation between them and their convective sources. Still, these waves can cause turbulence when breaking. In weather forecast models, the likelihood for the generation of convective cells is given by the Convective Available Potential Energy (CAPE). It is a measure for the instability in the atmosphere and given by the integral over the local buoyancy from the level of free convection to the equilibrium level. The level of free convection in turn is the level where the temperature of an ascending air-parcel falls below the ambient temperature. When its

#### 4.4. Meteorological background conditions

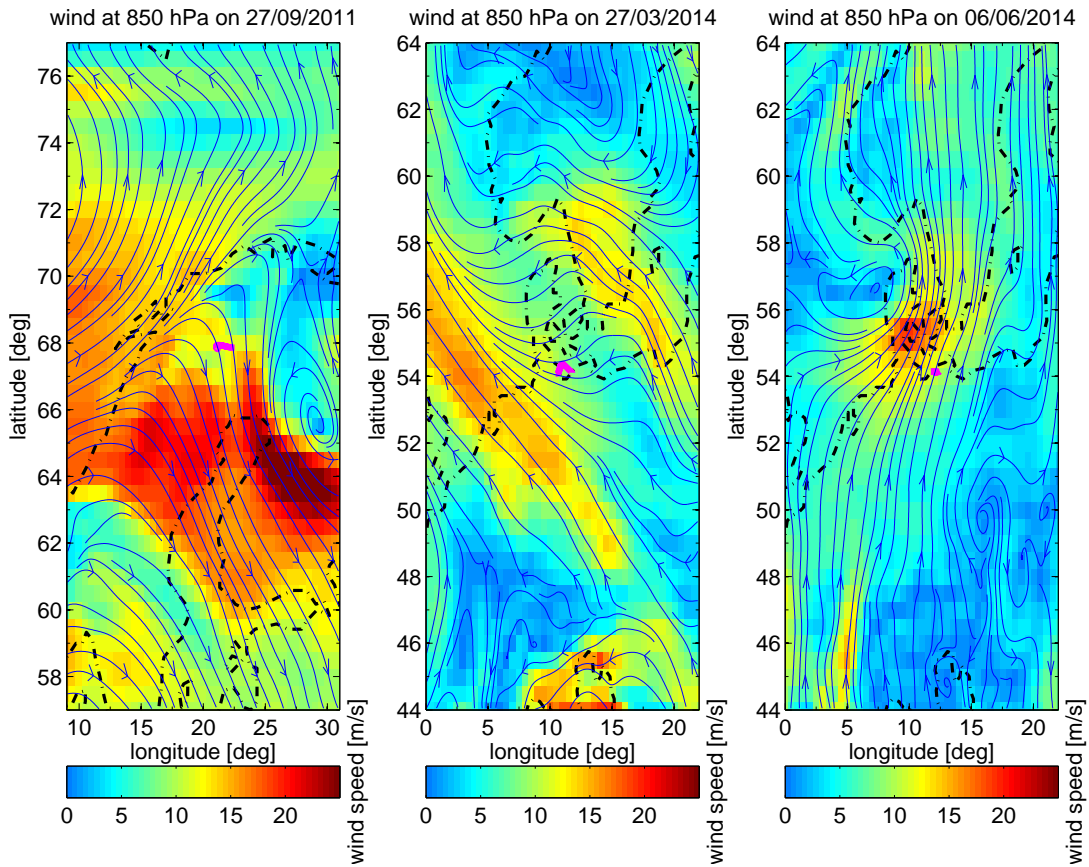


Figure 4.5.: Wind field at 850 hPa (approx. 1400 m) for the launch times of the different LITOS balloons. The flightpath is indicated by a magenta solid line. The streamlines of the wind field are given in blue.

temperature exceeds the ambient temperature, it has reached equilibrium level. The CAPE for all launches discussed in this section is shown in Figure 4.6. Please note the different colour scaling. Generally, in Europe 1500 J/kg to 2500 J/kg are considered as high values. On 27<sup>th</sup> September 2011, the only considerable amount of CAPE was found over northern Finland in a distance of 350 km to the launch point with 50 J/kg. This value is so low that no gravity wave generation by convection can be assumed on this day in the certain area. On 27<sup>th</sup> March 2014, CAPE activity was also very small in the flight area, whereas it reached 150 J/kg over England and France. Still, these values are so low that no considerable wave activity due to convection can be expected. In contrast, on 6<sup>th</sup> June 2014 the situation was different. Over northern Denmark (300 km from Kühlungsborn) CAPE up to 600 J/kg was found. Values of up to 1000 J/kg can be seen in a different patch above the Baltic countries. Even in northern Germany 200 J/kg are reached. Hence, in this case convection is a likely source of gravity waves over the launch area.

Moving on to the third type of gravity wave generation, the effects of geostrophical adjustment shall be assessed in the following. According to Fritts and Alexander [2003], gravity

#### 4. Geophysical results

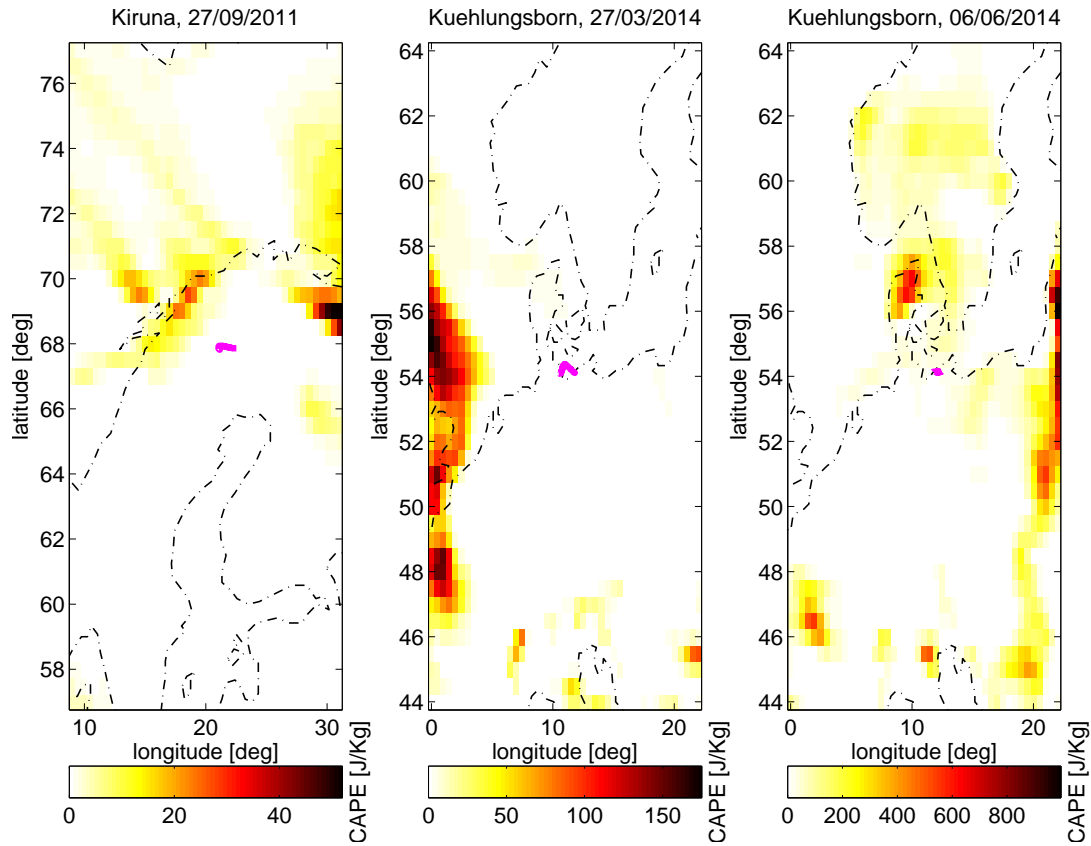


Figure 4.6.: Convective available potential energy (CAPE) on ground level as retrieved from GFS data for three different launches. The flightpath is given by a magenta solid line. Please note the different colour scaling.

waves are triggered especially in regions of strong flow deceleration and along certain synoptical patterns. In Europe this means that the jet-stream does a sharp right turn. From this turning point, gravity waves are emitted along the direction of the flow before the turn. See also O'Sullivan and Dunkerton [1995] for a more detailed picture of these flow patterns. They are usually evaluated in the wind field at a pressure of 500 hPa (around 5500 m). Such a plot can be seen in Figure 4.7. The flow shown in the first panel depicts a splitting of the jet stream and a strong deceleration at 68°N in front of the Norwegian coast. This is likely to have contributed to gravity wave activity. On 27<sup>th</sup> March 2014, the wind field over northern Germany was a stable parallel flow from south-southeast. There is a strong jet near the German-Polish border which creates considerable wind shear, but neither a major deceleration nor the typical patterns described above can be found. Hence medium gravity wave activity due to the shear is expected here. During the last launch, a splitting and a deflection of the jet stream as described above took place close to the German-Czech frontier. Furthermore, a flow deceleration is observed over the south-western Baltic Sea. The latter may have produced considerable gravity waves over northern Germany, whereas the frontal evolution in southeastern Germany may have emitted gravity waves in southeasterly direction which do

#### 4.4. Meteorological background conditions

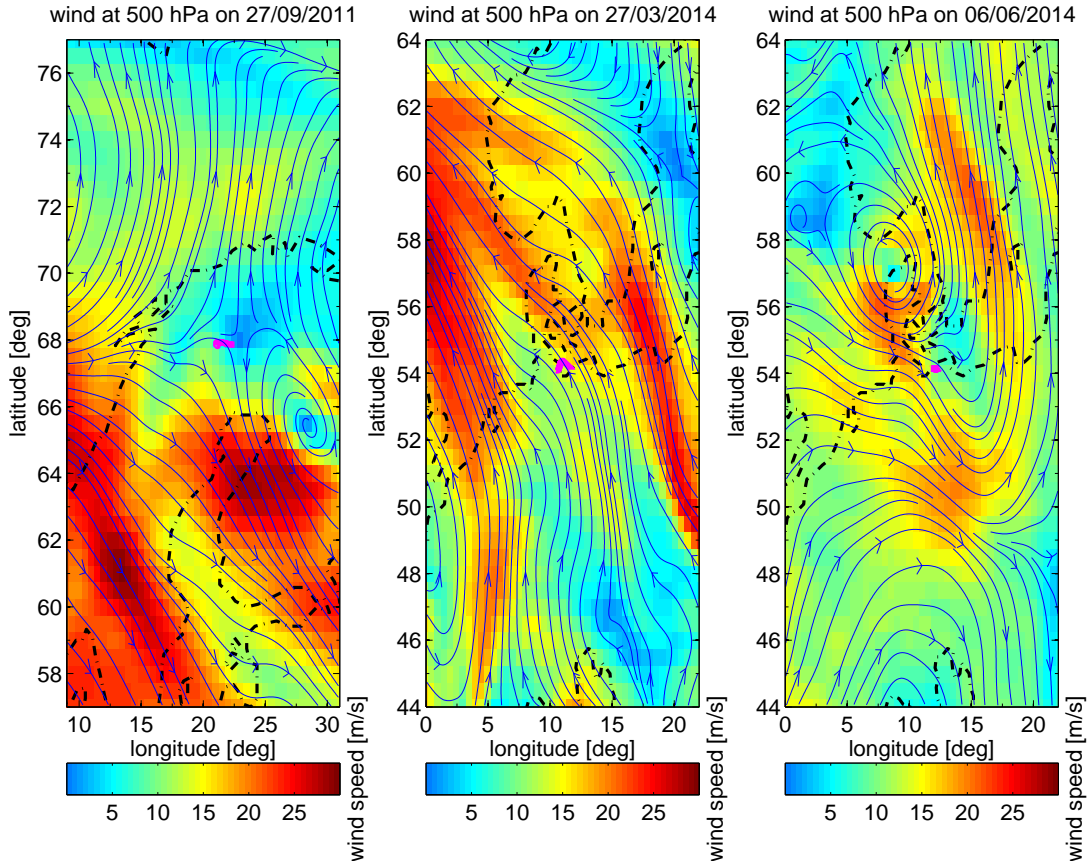


Figure 4.7.: Same as Figure 4.5, but for 500 hPa level.

not contribute in the launch area.

Concluding the evaluation of possible gravity wave sources, it is apparent that for 27<sup>th</sup> September 2011 rather high activity is expected due to mountain waves, whereas convection is not contributing. On 27<sup>th</sup> March 2014 tropospheric gravity wave motion is expected to be low due to small CAPE and negligible mountain wave activity. The strong wind shear at 500 hPa nevertheless may have caused some stratospheric activities. The launch in June 2014 shows rather high CAPE and strong deceleration of the flow, which predicts fairly strong gravity waves emitted in the troposphere. When comparing these statements with the results shown in Table 4.1 it is found that the launch on 6<sup>th</sup> June 2014 showed strongest turbulence activity in low to medium altitudes. Except for the uppermost regions, the one carried out from Kiruna reveals less activity and the first launch from Kühlungsborn features an even lower level of turbulence. Again, this does not hold for the region above 15 km. This is generally consistent with the expected wave activity. Still, one has to be careful when applying such considerations, because only possible sources of gravity waves were evaluated. Turbulence is not caused by the existence of gravity waves but by their breaking. This can be due to wind shears as evaluated in Section 4.6 or because of wave-wave interactions in the whole altitude range of LITOS. In the troposphere always local over-adiabatic temperature gradients

#### 4. Geophysical results

are found, which lead to wave breaking as well. For stronger statements, also direct measurements of gravity waves by LIDAR or RADAR would need to be taken into consideration.

### 4.5. Occurrence of turbulence compared to the Richardson number

As stated in Section 2.1.2, Richardson numbers below  $1/4$  are widely considered as a criterion for turbulence. Hence, in this section the correlation between turbulent atmospheric patches and low Richardson numbers will be evaluated.

In Figures 4.8 and 4.9 energy dissipation rates together with Richardson numbers inferred from radiosonde measurements for both launches from K uhlungsborn are given. Furthermore, the Brunt-V ais al a frequency  $N^2$  and the wind shear  $S^2$  are shown. As discussed in

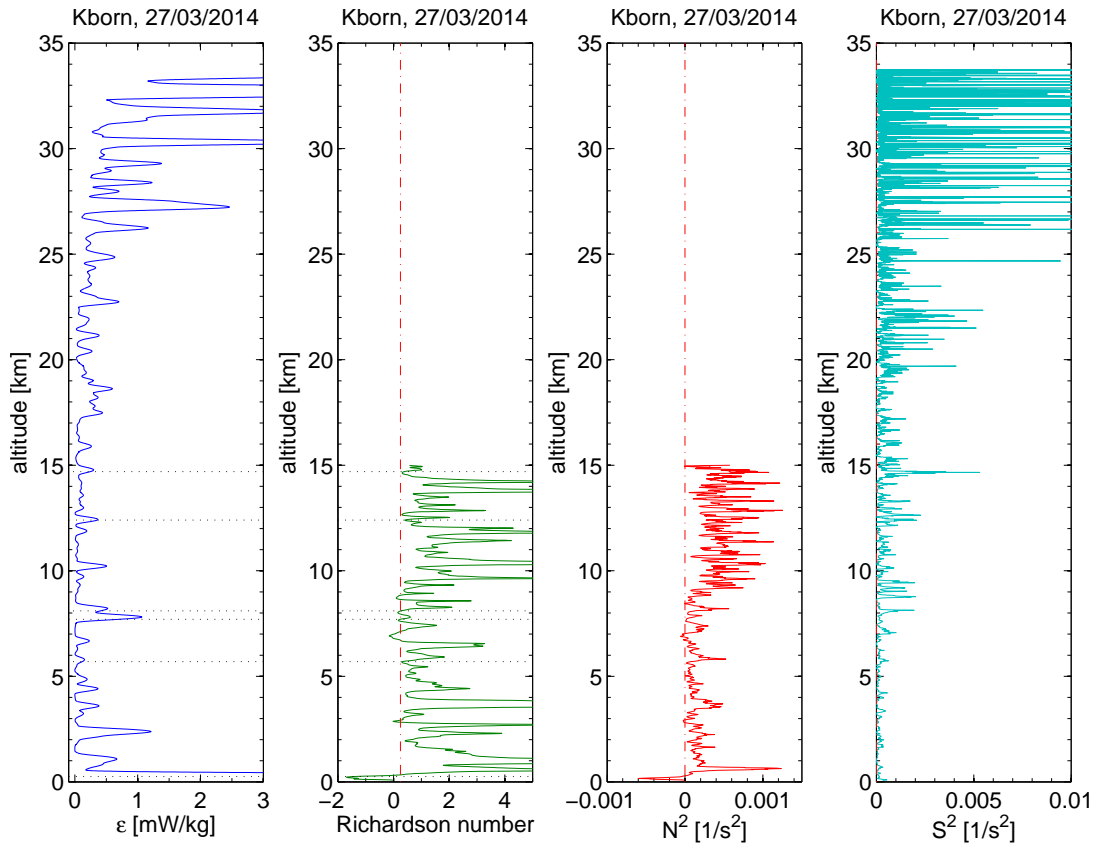


Figure 4.8.: Linear representation of energy dissipation rates (far left) and Richardson numbers (left) for 27<sup>th</sup> March 2014. The horizontal dotted lines point to peaks in the  $\varepsilon$ -profile that correspond to  $Ri < 1/4$ . The vertical red line highlights  $Ri = 1/4$ . The second and the third panel show the quadratic Brunt-V ais al a frequency  $N^2$  and the quadratic wind shear  $S^2$  respectively. Richardson numbers and Brunt-V ais al a frequencies above 15 km cannot be calculated due to disturbed temperature data.

#### 4.5. Occurrence of turbulence compared to the Richardson number

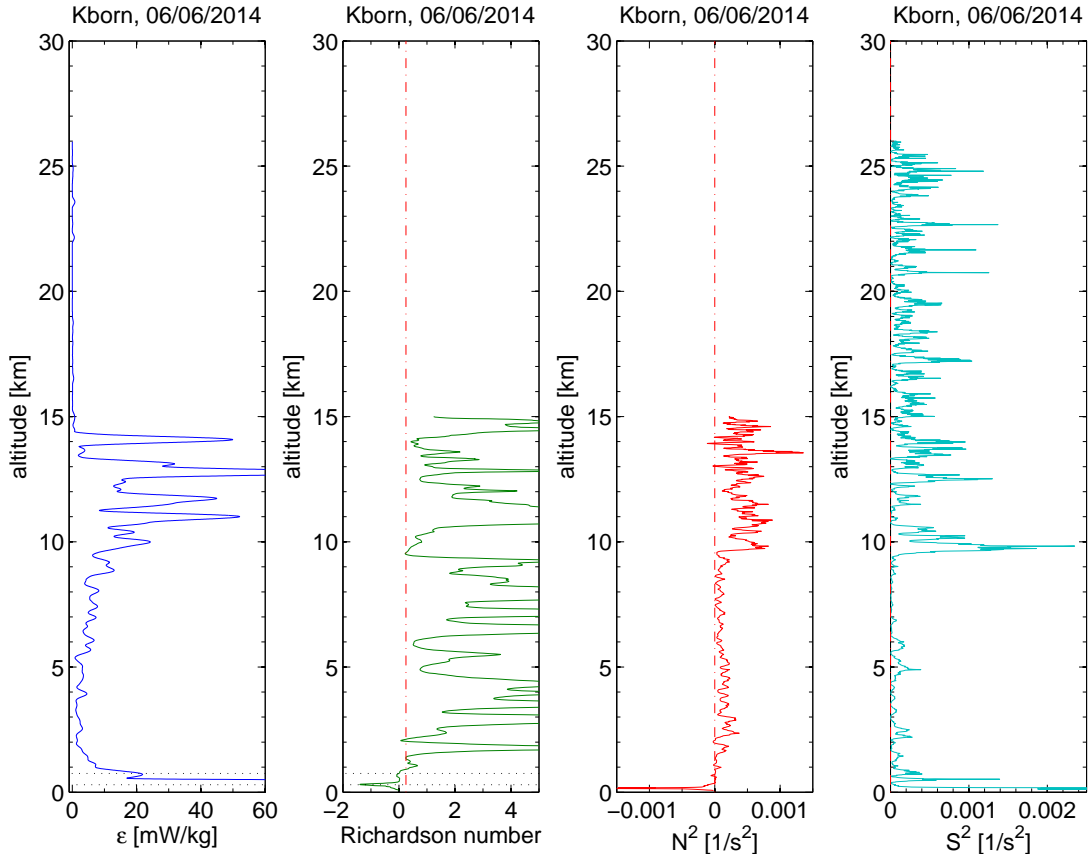


Figure 4.9.: Same as Figure 4.8 but for 6<sup>th</sup> June 2014.

Section 3.2.3, temperature measurements were disturbed by radiative effects, which means the Richardson numbers and Brunt-Väisälä frequencies are not plotted above 15 km and are increasingly noisy below.  $Ri$ ,  $N^2$  and  $S^2$  are calculated on a length scale of 20 m. It is assumed that the balloon moves with the horizontal wind, which means that the radiosonde in altitude  $z$  measures the wind at  $z + 150\text{ m}$ . However, this assumption is questionable because the cord between balloon and gondola also considerably influences the drag of the system. All in all, a height deviation of up to 75 m cannot be excluded. This affects potential temperatures and Richardson numbers. The linear representation of  $\varepsilon$  was chosen because it eases separation of areas with strong turbulence from those with weak turbulence.  $\varepsilon$  values were smoothed using an Hann filter with a supporting width of 200 m. When comparing  $Ri$  with  $\varepsilon$  for the first launch, six patches where the occurrence of stronger turbulence coincides with  $Ri < 1/4$  are found up to 15 km. There are areas where  $Ri < 1/4$ , but turbulence is weak. Yet the other case with strong turbulence and  $Ri > 1/4$  is far more common. In the second example, only two accordances of strong turbulence with  $Ri < 1/4$  are found. They are both located in the atmospheric boundary layer. Especially in this data set, strong turbulence with  $Ri > 1/4$  occurs far more often than the adversary case. When discussing turbulence in stratified flows, Thorpe [2005] cites the Miles-Howard theorem, according to which a shear flow is stable, as long  $Ri$

#### 4. Geophysical results

is larger than  $1/4$  everywhere in the fluid. Thorpe remarks that  $Ri < 1/4$  is a necessary but not sufficient condition for instability. On the contrary, Haack et al. [2014] found from evaluation of two balloon campaigns (BEXUS) using LITOS that there is no direct link between the Richardson number and the occurrence of turbulence. Looking at the data set given here it can be concluded that if there is a link between  $Ri$  and the occurrence of turbulence at all,  $Ri < 1/4$  is a sufficient condition for turbulence and not a necessary one.

#### 4.6. The influence of Kelvin-Helmholtz instabilities and gravity wave breaking on turbulence

In this section, data from Kühlungsborn will be evaluated with a focus on shear-generated turbulence. According to Fritts et al. [2003] Kelvin-Helmholtz (KH) instabilities in the atmosphere arise at strong shears of the mean wind which can be triggered by gravity waves. In a widely used picture (as presented in the previous section) this is associated with  $Ri < 1/4$  (dynamical instability) or  $Ri < 0$  (convective instability). This coherence has been questioned more recently though. Achatz [2005] for example does not see any connection between  $Ri < 1/4$  and the breaking of gravity waves. A wider overview is given in Haack et al. [2014]. Still, this introduction to the basic principles of turbulence creation will rely on the concepts of dynamic and convective instability, as done by Fritts et al. [2003].

The evolution of a KH instability can be divided into four stages which are shown in Figure 4.10. This picture was created using Direct Numerical Simulation (DNS) by Fritts and

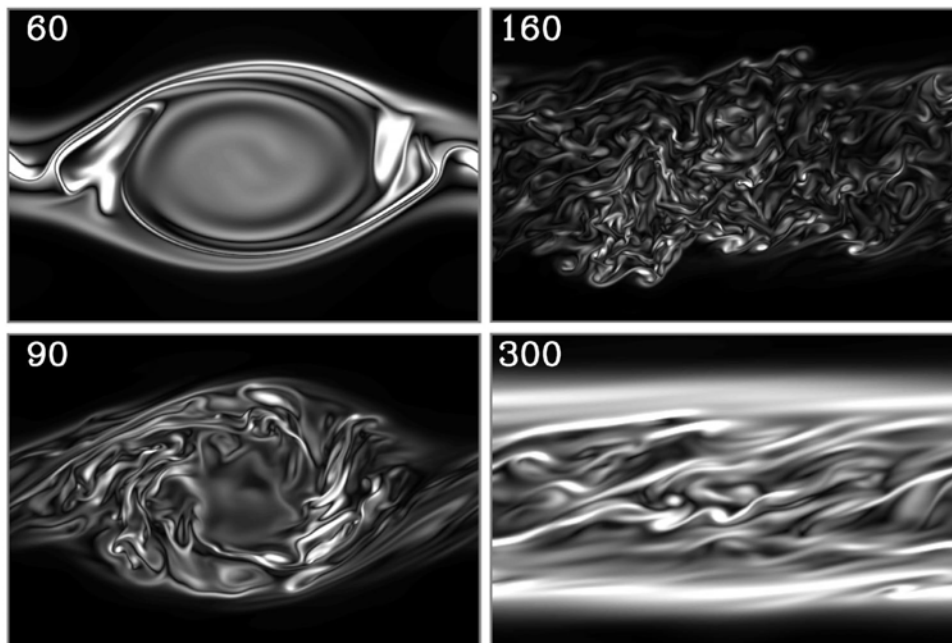


Figure 4.10.: Cross section of the vorticity magnitude in a Kelvin-Helmholtz instability. The cross sectional plane is located vertically in the direction of the flow. Graphics are taken from Fritts and Alexander [2003].

#### 4.6. The influence of Kelvin-Helmholtz instabilities and gravity wave breaking on turbulence

Alexander [2003]. The numbers in the upper left corners show time in arbitrary units, where one buoyancy period corresponds to 28 time elements. A KH instability is located inside the so called KH billow. The initial trigger for such a KH billow is a dynamical instability in the flow due to a shear in the background wind or temperature. This results in further vortices being created around the instability. Now vortices become smaller and smaller, as energy is transferred to smaller scales. Breaking of gravity waves on the other hand is characterised by an instability that emerges from the strong velocity and temperature gradients caused by the gravity wave itself. Fritts et al. [2003] state that gravity waves with low intrinsic frequencies and low group velocities often form KH billows, whereas those with high intrinsic frequencies quickly become not only dynamically but also convectively unstable, which results in gravity wave breaking. The authors also describe that KH instability is the more important of these two processes in the troposphere and lower stratosphere, whereas in the mesosphere gravity wave breaking becomes dominant.

When comparing energy dissipation rates shown in Figures 4.8 and 4.9, one will notice that the smoothed  $\varepsilon$  in the troposphere is approximately one order of magnitude higher in the latter. Close to the tropopause the data set from June 2014 shows maximal activities that are even two orders of magnitude higher compared to the March launch. Studying the stratosphere it can be noticed that maximum activity drops by two orders of magnitude compared to the tropopause region, whereas it increased on 27<sup>th</sup> March 2014 by almost one order of magnitude (see also Figures 4.1 and 4.2). In the previous section it was stated that there is no clear connection between the occurrence of highly turbulent altitude bins and  $Ri < 1/4$ . Unfortunately, there is no calculation of the Brunt-Väisälä frequency available above 15 km. Still, the wind shear  $S^2$  can be used for analysis. Assuming a constant  $N^2$ , an increasing  $S^2$  will result in a lower  $Ri$ . On 6<sup>th</sup> June 2014 there was a strong wind shear at about 10 km, which is likely to have resulted in KH instabilities or gravity wave breaking, even though  $Ri > 1/4$ . As opposed to the widely used picture, Achatz [2005] explicitly states that the Richardson criterion is not directly applicable to high frequency gravity waves. As mentioned in Section 4.4, gravity waves were mainly caused by shear and convection on this day, which leads to the generation of high frequency gravity waves. The turbulence generation at the wind shear mentioned above leads to the high  $\varepsilon$  values above 10 km. This wave breaking furthermore is expected to have filtered gravity waves, which in turn makes the stratosphere more quiet. On the other hand this does not explain the height offset between the maximum wind shear (10 km) and the sharp drop in energy dissipation rate (15 km). When comparing stratospheric winds for both flights the strong stratospheric increase in wind shear on 27<sup>th</sup> March 2014 attracts attention. This renders KH instabilities and gravity wave breaking very likely which in turn causes the high values of maximal energy dissipation rates in this altitude region compared to the data set from June 2014.



## 5. Conclusion and prospects

The scope of this work was to develop a small-scale payload for turbulence observations in the stratosphere. Previously, LITOS required the use of large balloons with heavy payloads like BEXUS for successful data analysis. Many technical details were improved including the payload mounting, its shape and material and the housing of the electronics. Data acquisition electronics was adapted by IAP as well. Furthermore, investigations were carried out to identify the source of certain non-atmospheric oscillations on the measurements. They resulted in using two independent CTA systems. As a result, LITOS can now be successfully operated on gondolas weighing below five kilogramme. Additionally, an all-new flightpath prediction system was created, which improves the accuracy of landing point forecasts. This enables launching under a larger variety of geophysical conditions, because the likelihood for payload loss is reduced.

On the new payload, LITOS measures turbulent energy dissipation rates from wind fluctuations. Energy dissipation rates vary by up to eight orders of magnitude during the flight. Arithmetic mean values of  $\varepsilon$  do not differ significantly between the troposphere and the stratosphere as a whole for both launches. When separating the stratosphere into two parts, an increase in  $\varepsilon$  is found all the way up from the troposphere to the stratosphere on 27<sup>th</sup> of March 2014, whereas values build up in the lowermost stratosphere on 06<sup>th</sup> of June 2014 but significantly decrease above. In the troposphere, arithmetic mean values of the energy dissipation rate are in good compliance with measurements carried out on other systems. In the stratosphere however, LITOS was found to measure energy dissipation rates two orders of magnitude higher than others. This is possibly caused by the higher altitude resolution of LITOS. The variation in energy dissipation rates measured with LITOS was compared to possible sources of turbulence by evaluation of meteorological parameters.

Future development of the payload will concentrate on the following points: The origin of the disturbances on the CTA signal is to be determined. The focus will be on sound waves as a possible source. Also, the radiosonde will be placed below the main LITOS payload, whereas the GPS-Iridium tracking unit may be allocated in the same box as LITOS in the future. Furthermore, improvements on temperature fluctuation measurements are highly desirable to allow for turbulence observation in these data. Additionally, a telemetry system is currently under development that will make LITOS usable in areas where payload recovery is impossible. The data retrieval software will especially undergo revisions of the noise level detection strategy.

From the geophysical point of view, the new payload allows for regular soundings with LITOS. Also, the restrictions on the launch point are much less compared to BEXUS. The greater flexibility facilitates investigating the time evolution of turbulence by releasing several LITOS payloads one after another from the same point. Furthermore, LITOS is planned to be launched during the METROSI (MEsoscale processes in TROposphere-Stratosphere In-

## *5. Conclusion and prospects*

teraction) project, which is part of the ROMIC (Role Of the Middle atmosphere In Climate) priority programme in Germany.

# A. Appendix

## A.1. Noise level detection

To improve the median-fit procedure described in Section 2.3.2, a new approach was developed. Instead of looking at the mean value in a certain frequency range, a spline function is fitted to the data set. An exemplary result can be seen in Figure A.1. In this procedure, all minima of the spline are retrieved in the first place. Then the programme is looking for the first minimum after the steep drop, caused by the viscous subrange. I.e., it searches for the right-most minimum which has a PSD at least one order of magnitude lower than the next minimum to the left. In the right panel of Figure A.1 this minimum is indicated by the red star at about  $10^{1.9}$  Hz. Experience shows that the beginning of the noise level is detected best by the sharp bend in the curve where it rises from noise level. Therefore, one is looking for the first maximum in the second derivative left of the minimum described above. In the right panel of Figure A.1 it is marked by the green vertical line. The noise level in turn is determined by the intersection of this vertical line with the measured curve.

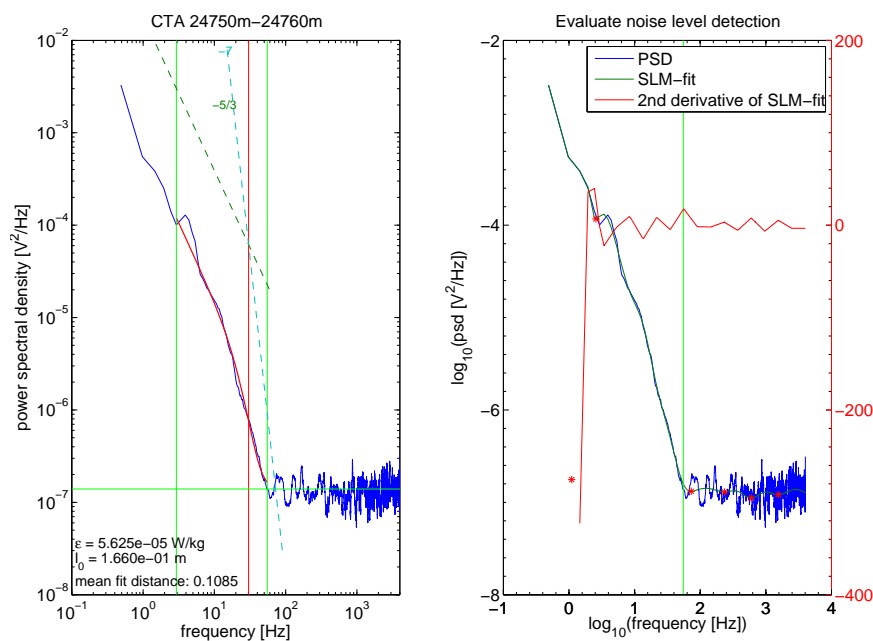


Figure A.1.: Left: Heisenberg fit with noise level detected by the derivative method. Right: Evaluation of noise level detection. The horizontal position of the high frequency border of the fit range (right-most green vertical line in both panels) is determined by evaluating the minima (red stars in the right panel) and the 2<sup>nd</sup> derivative of the fit. Further detail is given in the main text.

## A. Appendix

This method is more precise in the detection of the noise level in the stratosphere. Unfortunately, in the troposphere oscillations of non-atmospheric origin occur on the data (cf. Section 3.2.4). In that case the noise level can still be estimated with the median method fairly well, whereas the derivative method fails. Once the origin of these oscillations is found, the derivative method described here is expected to give better results than the median method.

### A.2. Dereeler cords

Until 2013, IAP used dereelers made by Graw Inc. for the launches of smaller LITOS payloads. They feature a braided rope, which is rather stiff and does not allow for much damping in the flight train. It was decided to reuse empty dereelers and wind them with monofilament fishing line made from nylon, which is more flexible. For the flight on 27<sup>th</sup> March it worked perfectly well, whereas for the two adjacent starts the line broke at launch. For all flights and for the ultimate load testing a knot called "Centaur knot" was in use, specifically designed for monofilament fishing line and supposed to retain more than 90% of the original line strength. In Table A.1 the stated and measured maximum loads are shown.

Table A.1.: Maximum load comparison of different fishing lines. All the testing was done after the second launch on 16<sup>th</sup> May 2014.

date	stated max. load [kg]	real max. load [kg]	failure
27-March-2014	19.6	12.4	NO
16-May-2014	17.3	7.6	YES
30-May-2014	29	25	YES

From the experience of the first flight, the line of the third one would have been expected to be strong enough. Examining the dereeler after the line had broken showed that under the strong pull at launch the top layer had become entangled with subjacent layers. This can possibly be avoided by winding the dereeler with a higher preload. However, it does not seem possible to do this by hand in a repeatable manner. Therefore this type of line was not used anymore.

## Bibliography

- U. Achatz. On the role of optimal perturbations in the instability of monochromatic gravity waves. *Physics of Fluids (1994-present)*, 17(9):094107, 2005.
- J.-R. Alisse, P. Haynes, J. Vanneste, and C. Sidi. Quantification of stratospheric mixing from turbulence microstructure measurements. *Geophysical Research Letters*, 27(17):2621–2624, 2000. ISSN 1944-8007. doi: 10.1029/2000GL011386. URL <http://dx.doi.org/10.1029/2000GL011386>.
- G. Allodi. FMINUIT A binding to minuit for matlab, octave & scilab, 2010. URL [http://www.fis.unipr.it/~giuseppe.allodi/Fminuit/Fminuit\\_intro.html](http://www.fis.unipr.it/~giuseppe.allodi/Fminuit/Fminuit_intro.html).
- R. Abmann. Über die Existenz eines wärmeren Luftstromes in der Höhe von 10 bis 15 km. *Sitzungsbericht der Königlich-Preußischen Akademie der Wissenschaften zu Berlin*, 24: 495–504, May 1902.
- J. Barat. Some characteristics of clear-air turbulence in the middle stratosphere. *Journal of the Atmospheric Science*, 39:2553–2564, 1982.
- J. Barat, C. Cot, and C. Sidi. On the measurement of the turbulence dissipation rate from rising balloons. *Journal of Atmospheric and Oceanic Technology*, 1(3):270–275, 1984.
- H. Bönisch, A. Engel, T. Birner, P. Hoor, D. Tarasick, and E. Ray. On the structural changes in the Brewer-Dobson circulation after 2000. *Atmospheric Chemistry and Physics*, 11(8):3937–3948, 2011. doi: 10.5194/acp-11-3937-2011. URL <http://www.atmos-chem-phys.net/11/3937/2011/>.
- G. Brasseur and S. Solomon. *Aeronomy of the middle atmosphere: chemistry and physics of the stratosphere and mesosphere*, volume 2. Springer, 1986.
- A. Brewer. Evidence for a world circulation provided by the measurements of helium and water vapour distribution in the stratosphere. *Quarterly Journal of the Royal Meteorological Society*, 75:351–363, 1949.
- A. Davis and A. Marshak. *3D radiative transfer in cloudy atmospheres*. Springer, 2005.
- R. Dirksen, M. Sommer, F. Immler, D. Hurst, R. Kivi, and H. Vömel. Reference quality upper-air measurements: GRUAN data processing for the vaisala RS92 radiosonde. *Atmospheric Measurement Techniques Discussions*, 7(4):3727–3800, 2014. doi: 10.5194/amtd-7-3727-2014. URL <http://www.atmos-meas-tech-discuss.net/7/3727/2014/>.

## Bibliography

- G. Dobson. Origin and distribution of the polyatomic molecules in the atmosphere. *Proceedings of the Royal Society of London. Series A, Mathematical and Physical Sciences*, 236: 187–193, 1956.
- F. Durst. *Fluid Mechanics: An Introduction to the Theory of Fluid Flows*. Springer, Berlin, Heidelberg, 2008.
- E. Fleming, S. Chandra, M. Schoeberl, and J. Barnett. *Monthly mean global climatology of temperature, wind, geopotential height, and pressure for 0-120 km*. National Aeronautics and Space Administration, 1988.
- D. Fritts and J. Alexander. Gravity wave dynamics and effects in the middle atmosphere. *Reviews of Geophysics*, 41(1), 2003.
- D. Fritts, C. Bizon, J. Werne, and C. Meyer. Layering accompanying turbulence generation due to shear instability and gravity-wave breaking. *Journal of Geophysical Research: Atmospheres (1984–2012)*, 108(D8), 2003.
- N. Gavrilov. Estimates of turbulent diffusivities and energy dissipation rates from satellite measurements of spectra of stratospheric refractivity perturbations. *Atmospheric Chemistry and Physics*, 13:12107–12116, 2013.
- N. Gavrilov, H. Luce, M. Crochet, F. Dalaudier, S. Fukao, et al. Turbulence parameter estimations from high-resolution balloon temperature measurements of the MUTSI-2000 campaign. In *Annales Geophysicae*, volume 23, pages 2401–2413, 2005.
- A. Haack, M. Gerding, and F.-J. Lübken. Characteristics of stratospheric turbulent layers measured by LITOS and their relation to the Richardson number. *Journal of Geophysical Research*, 2014. doi: 10.1002/2013JD021008. *accepted*.
- W. Heisenberg. Zur statistischen theorie der turbulenz. *Zeitschrift für Physik*, 124(7-12): 628–657, 1948.
- G. Hermite. Exploration des hautes régions de l’atmosphère à l’aide de ballons non montés, pourvus d’enregistreurs automatiques. *Comptes rendus hebdomadaires des séances de l’Académie des sciences*, 77:862–864, 1892. URL <http://gallica.bnf.fr/ark:/12148/bpt6k3073f>.
- K. Hoinka, S. Theis, and C. Gebhardt. The tropopause: discovery, definition and demarcation. *Meteorologische Zeitschrift*, 6:281–303, 12 1997.
- W.-H. Hucho. *Aerodynamik der stumpfen Körper*, volume 2. Wiesbaden, 2011.
- L. King. On the convection of heat from small cylinders in a stream of fluid: Determination of the convection constants of small platinum wires, with applications to hot-wire anemometry. *Proceedings of the Royal Society of London. Series A*, 90(622):563–570, 1914. doi: 10.1098/rspa.1914.0089. URL <http://rspa.royalsocietypublishing.org/content/90/622/563.short>.

- A. Kolmogorov. The local structure of turbulence in incompressible viscous fluid for very large Reynolds numbers. In *Dokl. Akad. Nauk SSSR*, volume 30, pages 299–303, 1941.
- F.-J. Lübken. On the extraction of turbulent parameters from atmospheric density fluctuations. *Journal of Geophysical Research: Atmospheres (1984–2012)*, 97(D18):20385–20395, 1992.
- F.-J. Lübken. *Experimental Results on the Role of Turbulence for the Heat Budget of the Upper Atmosphere*. Habilitation, Rheinische Friedrich-Wilhelms-Universität, Bonn, 1993.
- F.-J. Lübken. Seasonal variation of turbulent energy dissipation rates at high latitudes as determined by in situ measurements of neutral density fluctuations. *Journal of Geophysical Research: Atmospheres (1984–2012)*, 102(D12):13441–13456, 1997.
- F.-J. Lübken. Turbulent scattering for radars: A summary. *Journal of Atmospheric and Solar-Terrestrial Physics*, 107:1–7, 2014.
- J. Mathieu and J. Scott. *An introduction to turbulent flow*. Cambridge University Press, 2000.
- G. Nastrom and F. Eaton. Persistent layers of enhanced C<sub>2</sub>N in the lower stratosphere from VHF radar observations. *Radio Science*, 36(1):137–149, 2001. ISSN 1944-799X. doi: 10.1029/2000RS002318. URL <http://dx.doi.org/10.1029/2000RS002318>.
- NOAA. US standard atmosphere, 1976. Technical report, NOAA-S/T, 1976.
- D. O’Sullivan and T. Dunkerton. Generation of inertia-gravity waves in a simulated life cycle of baroclinic instability. *Journal of the Atmospheric Sciences*, 52(21):3695–3716, 1995.
- R. Ozmidov. On the turbulent exchange in a stably stratified ocean. *Izv. Acad. Sci. USSR, Atmos. Oceanic Phys.*, 1:861–871, 1965.
- S. Pope. *Turbulent flows*. Cambridge university press, 2000.
- S. Randall. Balloon data, burst calculator, 2014. URL [http://wiki.ukhas.org.uk/guides:balloon\\_data](http://wiki.ukhas.org.uk/guides:balloon_data). [Online; accessed 31-August-2014].
- M. Schäfer. Realitätsbezogener Mechanikunterricht durch Beiträge der Strömungsphysik, 2002. URL [http://www.dlr.de/schoollab/Portaldata/24/Resources/dokumente/go/14.8.02\\_Ankuendigung.pdf](http://www.dlr.de/schoollab/Portaldata/24/Resources/dokumente/go/14.8.02_Ankuendigung.pdf). [Online; accessed 10-July-2014].
- A. Schneider, M. Gerding, and F.-J. Lübken. Comparing turbulent parameters obtained from LITOS and radiosonde measurements. *Atmospheric Chemistry and Physics Discussions*, 14(13):19033–19053, 2014. doi: 10.5194/acpd-14-19033-2014. URL <http://www.atmos-chem-phys-discuss.net/14/19033/2014/>.
- R. Sharman, S. Trier, T. Lane, and J. Doyle. Sources and dynamics of turbulence in the upper troposphere and lower stratosphere: A review. *Geophysical Research Letters*, 39(12), 2012.
- T. Shepherd. Transport in the middle atmosphere. *Journal of the Meteorological Society of Japan*, 85B:165–191, 2007. URL <http://centaur.reading.ac.uk/31785/>.

## Bibliography

- I. Smalikho, F. Köpp, and S. Rahm. Measurement of atmospheric turbulence by 2- $\mu$ m doppler lidar. *Journal of Atmospheric and Oceanic Technology*, 22(11):1733–1747, 2005.
- V. Sofieva, A. Gurvich, F. Dalaudier, and V. Kan. Reconstruction of internal gravity wave and turbulence parameters in the stratosphere using GOMOS scintillation measurements. *Journal of Geophysical Research*, 112:D12113, 2007. doi: 10.1029/2006JD007483.
- V. Sofieva, A. Gurvich, and F. Dalaudier. Mapping gravity waves and turbulence in the stratosphere using satellite measurements of stellar scintillation. *Physica Scripta*, 2010 (T142):014043, 2010.
- O. Sumińska. Application of a constant temperature anemometer for balloon-borne stratospheric turbulence soundings. Master’s thesis, Leibniz-Institute of Atmospheric Physics e.V. at University of Rostock, 2008.
- V. I. Tatarski. *Wave propagation in a turbulent medium*. Mc Graw-Hill Book Company, 1961.
- V. I. Tatarskii. *The effects of the turbulent atmosphere on wave propagation*. 1971.
- G. Taylor. The spectrum of turbulence. *Proceedings of the Royal Society of London. Series A-Mathematical and Physical Sciences*, 164(919):476–490, 1938.
- H. Tennekes and J. Lumley. *A first course in turbulence*. The MIT Press, Cambridge (Massachusetts), 1972.
- A. Theuerkauf. *Stratospheric turbulence observation with the new balloon-borne instrument LITOS*. PhD thesis, IAP Kühlungsborn, 2012.
- A. Theuerkauf, M. Gerding, and F.-J. Lübken. LITOS – a new balloon-borne instrument for fine-scale turbulence soundings in the stratosphere. *Atmospheric Measurement Techniques*, 4(1):55–66, 2011.
- S. Thorpe. *The Turbulent Ocean*. Cambridge University Press, Cambridge, 2005.
- D. Waco. A statistical analysis of wind and temperature variables associated with high altitude clear air turbulence (HICAT). *Journal of Applied Meteorology*, 9(2):300–309, 1970.
- Wikipedia. Drag (physics) — Wikipedia, the free encyclopedia, 2014a. URL [http://en.wikipedia.org/w/index.php?title=Drag\\_\(physics\)&oldid=620848038](http://en.wikipedia.org/w/index.php?title=Drag_(physics)&oldid=620848038). [Online; accessed 13-August-2014].
- Wikipedia. Section modulus — wikipedia, the free encyclopedia, 2014b. URL [http://en.wikipedia.org/w/index.php?title=Section\\_modulus&oldid=611284649](http://en.wikipedia.org/w/index.php?title=Section_modulus&oldid=611284649). [Online; accessed 11-July-2014].

## Acknowledgements

I am grateful for all those who made this work possible. Thanks to the team at IAP for the fruitful cooperation and the pleasant working atmosphere.

In particular, I would like to make a reference to Prof. Franz-Josef Lübken for the great opportunity to work with sounding balloons in his group at IAP. Special thanks go to Michael Gerding for his close supervision, his encouragements and his particular patience shown in countless discussions. Without him this work could not be close to what it is. Furthermore I like to thank Andreas Schneider for introducing me to all the details of LITOS and to Reik Ostermann for his support with the electronics.

I am greatly indebted to Erik Jeglorz for lively and enriching conversations on matters of physics and beyond. Also I like to express my gratitude to Anna-Lena Bulgrin for proofreading this thesis. Thank you very much indeed.

Last but not least I am obliged to my family and friends, for sharing the happy moments with me and for supporting me in times of despair.



## **Statement of authorship**

Hereby I certify that the work presented in this master thesis has been performed solely by myself except where explicitly identified to the contrary. Any sources from which I used data, ideas or words either in quotation or in paraphrase are cited. I confirm that this work is submitted in partial fulfilment for the degree of M. Sc. in physics and has not been submitted elsewhere in any other form for the fulfilment of any other degree or qualification.

Rostock, 05<sup>th</sup> September 2014

(Jens Söder)